



Department of Materials Science and Engineering  
Faculty of Mechanical Maritime and Materials Engineering

# Optical Emission Spectroscopy during Wire and Arc Additive Manufacturing

Gautham Mahadevan  
4794443

Thesis Committee:  
Prof. Dr. ir. Marcel Hermans  
Dr. ir. Wei Ya  
Prof. Dr. ir. Vera Popovich  
Prof. Dr. ir. Erik Offerman  
Prof. Dr. ir. Constantinos Goulas

Delft, September 23, 2020



# Abstract

Additive Manufacturing (AM) has been identified to be a key technology in the ‘third industrial revolution’ - a new wave of manufacturing technologies characterised by functional software, flexible robots, and a range of digitized services that addressed the limitations of traditional casting and milling based subtractive manufacturing processes. Wire and Arc Additive Manufacturing (WAAM) is one such AM technique that is used to produce metal components that are near net shape. Mechanical testing, failure analysis and microstructure investigation of the finished component is done only after it is fully built. Building defective parts increases the material usage, power consumption, build time, and overall cost of production. Thus, real time detection of process and product anomalies not only saves money and material but can also improve the mechanical properties of the printed component.

One such monitoring technique is Optical Emission Spectroscopy (OES), where the electromagnetic radiation emitted by the plasma arc in the printing process is used to characterize the processing conditions of the WAAM environment. Although OES has been used for quality control in arc welding as well as powder-based AM processes, there has not been any previous study directly focused on the use of OES to study the WAAM process. Monitoring systems require a robust setup that can collect reliable and repeatable data, if it is to be used for quality control. Although OES is a feasible method to study arc radiation, there is currently no application of this technique in a reliable monitoring system for commercial application.

The goal of this study was to develop an OES based monitoring system for the WAAM process. The monitoring system consisted of an experimental setup designed to collect reliable optical emission data from the plasma arc using an optic fibre attachment to the WAAM robot and a software system was designed to perform data analysis and post-processing of the collected optical spectrum. The developed monitoring system was validated by performing a series of experiments with different processing conditions (welding current, voltage, speed and surface conditions) to investigate the potential correlations among them with the detected optical spectrum. A peak characterization test was designed with different material combinations to test the reliability of the emission peak matching algorithm that was developed. It was followed by a ramping test where the heat input was incrementally increased to study the correlation with the processed OES signals. The final experiment was an anomaly detection test where the OES data was used to characterize the presence of an artificially deposited ceramic anomaly on the base plate that simulated the presence of an impurity. Secondary investigation techniques like optical microscopy, a high-frequency V-I sensor and a high-speed camera footage was used to validate the OES observations. The results of these experiments showed the feasibility of OES based monitoring systems for WAAM. However, the obtained results were not always consistent and the system requires further research before it can be used for reliable quality control of the WAAM process.





# Acknowledgements

The last 10 months have been one of the most challenging but rewarding experiences I have had. Working on this thesis has not only improved my understanding of materials science but also taught me valuable lessons in organization, time management and communication which I will carry with me forever. This thesis would not be possible without the help and guidance of many people whose contribution I would like to acknowledge.

This thesis was done at the Rotterdam Additive Manufacturing Lab (RAMLAB) in collaboration with the MSE department at TU Delft.

I'd like to thank Vincent Wegener and RAMLAB for giving me an opportunity to work on such an interesting project. I'd like to thank my supervisor Wei Ya for his training, teaching and patience to answer all of my questions. I would also like to thank Ben and Vignesh for assisting me with experiments and everyone at RAMLAB for their help and support.

I'd like to thank my thesis supervisor Marcel Hermans for his support and guidance throughout the project. I'd like to thank Jurriaan for his time and assistance with the high-speed camera experiments. I'd also like to thank Sander and Remko for their invaluable help with the microscopy tests.

I'd like to acknowledge the inspiring teachers I have had the privilege of learning from. I'd like to thank KS Balaji and Balaji Sampath for shaping my understanding of science and teaching me how to ask questions. I'd like to thank Ms Malini for her kindness and wisdom. I'd also like to thank Prof Raman and Prof Abhinandan for their advice and guidance.

I'd like to thank my friends for being my constant source of support and inspiration and for always being there for me whenever I needed.

I'd like to thank my parents for everything they have done for me and their support towards making me achieve my goals and dreams. I would finally like to thank my brother for all his help and wisdom, and for lighting the early spark of curiosity that still motivates me today.

*Gautham Mahadevan  
Delft, September 2020*



# Contents

<b>Contents</b>	<b>vii</b>
<b>List of Figures</b>	<b>xi</b>
<b>List of Tables</b>	<b>xv</b>
<b>1 Thesis Outline</b>	<b>1</b>
1.1 Background . . . . .	1
1.2 Thesis outline . . . . .	2
<b>2 Literature Survey</b>	<b>3</b>
2.1 Evolution of Manufacturing Systems . . . . .	3
2.2 Additive Manufacturing . . . . .	4
2.2.1 Rapid Prototyping and Rapid Manufacturing . . . . .	4
2.2.2 Metallic AM . . . . .	6
2.3 Wire and Arc Additive Manufacturing . . . . .	7
2.3.1 History of WAAM . . . . .	8
2.3.2 WAAM process conditions and workflow . . . . .	8
2.3.3 Optimizing WAAM system . . . . .	9
2.4 Limitations of WAAM . . . . .	10
2.4.1 Cracking . . . . .	10
2.4.2 Porosity . . . . .	10
2.4.3 Lack of Fusion . . . . .	11
2.4.4 Inclusions and Phase Instability . . . . .	12
2.5 Monitoring and Control . . . . .	13
2.5.1 Thermal based monitoring . . . . .	13
2.5.2 Electromagnetic signal monitoring . . . . .	13
2.6 Optical Emission Spectroscopy . . . . .	14
2.6.1 OES for monitoring and control . . . . .	15
2.6.2 Limitations and Knowledge Gaps . . . . .	15
2.7 Objectives of this study . . . . .	15
<b>3 Theory</b>	<b>17</b>
3.1 Introduction . . . . .	17
3.2 Metal Transfer Mechanisms . . . . .	17
3.2.1 Short-circuit Metal Transfer . . . . .	18
3.3 Thermodynamic Equilibrium . . . . .	20

3.3.1	Maxwell's Equation . . . . .	20
3.3.2	Boltzmann's Law . . . . .	20
3.3.3	Saha's Equation . . . . .	21
3.3.4	Local Thermodynamic Equilibrium . . . . .	21
3.4	Plasma Diagnostics . . . . .	22
3.4.1	Line Intensity Ratio . . . . .	22
3.4.2	Boltzmann Plot Method . . . . .	23
3.5	Conclusion . . . . .	25
<b>4</b>	<b>Materials and Methods</b>	<b>27</b>
4.1	Introduction . . . . .	27
4.2	Experiment Setup . . . . .	27
4.3	Materials Used . . . . .	30
4.4	Self-programmed Software for OES data analysis . . . . .	30
4.4.1	Spectral Data Collection . . . . .	31
4.4.2	NIST database . . . . .	32
4.4.3	Baseline Estimation . . . . .	32
4.4.4	Peak Characterization . . . . .	33
4.4.4.1	Finding Peaks . . . . .	34
4.4.4.2	Matching Peaks . . . . .	34
4.4.5	Intensity Ratio and Temperature calculations . . . . .	35
4.4.5.1	Intensity Ratio . . . . .	35
4.4.5.2	Implementation of Boltzmann Plot . . . . .	36
4.4.6	Process Parameters Visualization . . . . .	38
4.5	Experiment Design . . . . .	38
4.5.1	Spectrometer Optimization . . . . .	39
4.5.1.1	Positioning . . . . .	39
4.5.1.2	Signal Saturation . . . . .	42
4.5.1.3	Integration Time . . . . .	42
4.5.1.4	Optic Filter . . . . .	42
4.5.1.5	Angle Optimization . . . . .	43
4.5.1.6	Signal Repeatability . . . . .	44
4.5.2	Setup and Software Validation . . . . .	45
4.5.2.1	Peak Characterization Test . . . . .	45
4.5.2.2	Ramping Test . . . . .	45
4.5.2.3	Anomaly Detection Test . . . . .	46
4.5.2.4	Validation of Anomaly Detection Test . . . . .	47
<b>5</b>	<b>Results and Discussion</b>	<b>49</b>
5.1	Spectrometer Optimization: Angle Test . . . . .	49
5.1.1	Results . . . . .	49
5.1.2	Discussion . . . . .	51
5.2	Selection of Emission Peaks . . . . .	52
5.3	Spectrometer Optimization: Signal Repeatability . . . . .	53
5.4	Software Validation: Peak Characterization . . . . .	57
5.4.1	Results . . . . .	57
5.4.2	Discussion . . . . .	59

5.5	Software Validation: Ramping Test . . . . .	59
5.5.1	Intensity Profiles . . . . .	61
5.5.2	Temperature and Intensity Ratio Profiles . . . . .	62
5.6	Software Validation: Anomaly Detection . . . . .	64
5.6.1	Results . . . . .	64
5.6.1.1	Intensity Profiles . . . . .	65
5.6.1.2	Plasma Temperature . . . . .	66
5.6.1.3	Intensity Ratio . . . . .	69
5.6.2	Discussion . . . . .	71
5.6.2.1	High Frequency Voltage Analysis . . . . .	72
5.6.2.2	High-speed camera investigation . . . . .	75
5.6.2.3	Weld Appearance and Geometry . . . . .	78
5.6.3	Conclusions of Anomaly Test . . . . .	82
<b>6</b>	<b>Conclusions and Future Directions</b>	<b>85</b>
6.1	Conclusions . . . . .	85
6.2	Future Directions . . . . .	86
	<b>Bibliography</b>	<b>87</b>



# List of Figures

2.1	Global AM market and Compound Annual Growth Rate [6] . . . . .	4
2.2	Schematic of Selective Laser Melting RP process [12] . . . . .	5
2.3	Classification of AM systems [17] . . . . .	6
2.4	Schematic of WAAM process [30] . . . . .	9
2.5	Mechanism of crack formation [48] . . . . .	10
2.6	Porosity in WAAM [42] . . . . .	11
2.7	Lack of Fusion defect in AM [42] . . . . .	12
2.8	Oxide inclusions in AM part [55] . . . . .	12
2.9	The differential dilution sensor response to continuous variation of laser clad- ding dilution in real time [39] . . . . .	14
3.1	Oscillogram of short-circuit transfer [76] . . . . .	18
3.2	High speed camera images of metal transfer process in short-circuit transfer [78]	19
3.3	Example of plasma temperature calculation for 4 Chromium emission lines of wavelengths between 474-481 nm . . . . .	24
4.1	Schematic diagram of WAAM Setup . . . . .	28
4.2	WAAM Experimental Setup . . . . .	29
4.3	Sample data file generated by the spectrometer . . . . .	31
4.4	NIST Atomic Spectra database [86] . . . . .	32
4.5	Flowchart for baseline estimation algorithm . . . . .	33
4.6	Flowchart for Peak Matching algorithm . . . . .	34
4.7	Software Application GUI of peak characterization . . . . .	35
4.8	App GUI to visualize Intensity Ratio profiles . . . . .	36
4.9	App GUI to visualize Plasma Temperature profiles . . . . .	37
4.10	App GUI to visualize high frequency V-I data . . . . .	38
4.11	Spectrometer Positioning Setup . . . . .	40
4.12	Angle calculation using pilot laser . . . . .	41
4.13	Two dimensional schematic representation of angle calculation using pilot laser	41
4.14	a) OES spectrum without filter b) OES spectrum with filter . . . . .	43
4.15	Experimental setup for angle test . . . . .	44
4.16	Schematic drawing of Ramping Test processing conditions along a deposition line of 5x36 mm . . . . .	46
4.17	Ceramic pattern on S355 base plate for the Anomaly Detection Test . . . . .	46
5.1	Angle Test baseline profiles . . . . .	50
5.2	Sample baseline calculation for an observation angle of 20° . . . . .	50

## LIST OF FIGURES

---

5.3	Planck's black body radiation curve . . . . .	51
5.4	Cr I peaks chosen for temperature calculations . . . . .	52
5.5	Fe I peaks chosen for intensity ratio calculations . . . . .	53
5.6	Repeatable signal comparison at TS = 0.7 m/min a) Intensity profile b) Plasma Temperature profile c) Intensity Ratio profile . . . . .	54
5.7	Repeatable signal comparison at TS = 0.3 m/min a) Intensity profile b) Plasma Temperature profile c) Intensity Ratio profile . . . . .	55
5.8	Example of non repeatable signal for same processing conditions at TS = 0.3 m/min a) Intensity profile b) Plasma Temperature profile c) Intensity Ratio profile . . . . .	56
5.9	Peak characterization of signal from with 316L wire and Inomaxx shielding gas	57
5.10	Peak characterization of signal from with NiCrMo wire and Ferromaxx shielding gas . . . . .	58
5.11	Peak characterization of signal from with X89 steel wire and Argon shielding gas	58
5.12	Weld beads for different travel speeds in ramping conditions . . . . .	60
5.13	Intensity profile of a Chromium emission peak 527.2 nm . . . . .	61
5.14	Plasma Temperature profiles from Ramping Test for different travel speeds .	62
5.15	Intensity Ratio from Ramping Test for different travel speeds . . . . .	63
5.16	Intensity of Cr I emission line at wavelength of 528.76 nm at a) TS = 1.2 m/min b) TS = 0.7 m/min c) TS = 0.3 m/min . . . . .	65
5.17	Comparison of plasma temperature profiles in anomaly detection test at TS = 1.2 m/min . . . . .	66
5.18	Comparison of plasma temperature profiles in anomaly detection test at TS = 0.7 m/min . . . . .	67
5.19	Comparison of plasma temperature profiles in anomaly detection test at TS = 0.3 m/min . . . . .	68
5.20	Comparison of intensity ratio profiles in anomaly detection test at TS = 1.2 m/min . . . . .	69
5.21	Comparison of intensity ratio profiles in anomaly detection test at TS = 0.7 m/min . . . . .	70
5.22	Comparison of intensity ratio profiles in anomaly detection test at TS = 0.3 m/min . . . . .	70
5.23	Detected voltage waveform of SAWP metal transfer mode on a ceramic-free base plate at a TS of 0.7 m/min . . . . .	72
5.24	Selected regions for comparative study of voltage waveforms . . . . .	73
5.25	Voltage waveform from region 1 and 2 at TS = 1.2 m/min . . . . .	73
5.26	Voltage waveform from region 1 and 2 at TS = 0.7 m/min . . . . .	74
5.27	Voltage waveform from region 1 and 2 at TS = 0.3 m/min . . . . .	74
5.28	High speed camera footage of metal transfer in ceramic region a) Before arc ignition b) Arc ignition c) Wire pulled back up by servo motor d and e) Drop detachment f) Arc off . . . . .	76
5.29	High speed camera footage of metal transfer in ceramic region a) Arc off b,c) Arc ignition d) Asymmetric arc e) Servo motor drawn up without droplet detachment f,g) Arc ignition h) Droplet detachment i) Arc off . . . . .	77
5.30	Voltage waveform in ceramic region . . . . .	77
5.31	a) Symmetric arc in ceramic free region b) Asymmetric arc in ceramic region	78

---



5.32 180 mm welds of different travel speeds printed on the ceramic pattern for anomaly detection with welding current of 160 A and welding voltage of 18 V	79
5.33 Sample cross-sections for optical microscopy analysis . . . . .	79
5.34 Schematic of a WAAM weld track [64] . . . . .	80
5.35 Weld geometry parameters for all samples at a) TS = 1.2 m/min b) TS = 0.7m/min c) TS = 0.3 m/min . . . . .	81
5.36 Optical micrographs of weld samples at a) TS = 0.3 m/min in ceramic b) TS = 0.7 m/min in ceramic c) TS = 1.2 m/min in ceramic d) TS = 0.3 m/min without ceramic e) TS = 0.7 m/min without ceramic f) TS = 1.2 m/min without ceramic . . . . .	82



# List of Tables

3.1	Chromium emission line data from NIST database for temperature calculation in Fig 3.3 . . . . .	24
4.1	Composition of LN316 LSi welding wire . . . . .	30
4.2	Composition of S355 steel plate . . . . .	30
4.3	Composition of Inomaxx Plus shielding gas . . . . .	30
4.4	Composition of NiCrMoFe wire . . . . .	30
4.5	Composition of Ferromax Plus shielding gas . . . . .	30
4.6	Composition of X90 steel wire . . . . .	30
4.7	Composition of Abicor Binzel ceramic spray . . . . .	30
5.1	Weld geometry parameters for TS = 1.2 m/min . . . . .	80
5.2	Weld geometry parameters for TS = 0.7 m/min . . . . .	80
5.3	Weld geometry parameters for TS = 0.3 m/min . . . . .	81



# Chapter 1

## Thesis Outline

### 1.1 Background

The evolution of industrial manufacturing relies on innovation in processes, materials and product design. The manufacturing industry traditionally used subtractive manufacturing (SM) techniques to build parts. SM is a top-down approach that successively removes material from a solid block of metal. In most cases the larger block of material is made by casting and then further cut and milled to remove the excess. Additive Manufacturing (AM) was identified to be a key technology in the ‘third industrial revolution’ - a new wave of manufacturing technologies characterised by functional software, flexible robots, new processes, and a range of web-based services that addressed the limitations of subtractive manufacturing.

AM is a term to describe a class of processes that uses a layer-additive approach to design and construct parts, and utilize different heat sources like a laser, plasma arc or an electron beam. They are an extension of rapid prototyping processes that use a bottom-up technique, comparable to stereolithography and welding repair techniques. The metallic AM integrates these rapid prototyping techniques with principles from Computer Aided Design (CAD). The automation of the process enables manufacturers to build structural parts directly from CAD data.

Wire and Arc Additive Manufacturing (WAAM) is a subcategory of AM. It uses a metal wire as the feedstock, and an electric arc as the heat source, thereby combining both welding and additive manufacturing techniques. Similar to Gas Metal Arc Welding (GMAW) and Metal Inert Gas welding (MIG), the process utilises a welding torch, a power source, metal wire, and a shielding gas. It also has either a robotic system or a gantry system that controls the movement of the torch to build functional products that are near net-shape.

Mechanical testing, failure analysis and microstructure investigation of the components built with WAAM is done only after it is fully built. Building defective parts increases the material usage, power consumption, build time, and overall cost of production. Thus, real time monitoring and detection of process and product anomalies not only saves money and material but can also improve the quality of the part. Necessary interventions and repairs can be in place to prevent the defective build.

Optical Emission Spectroscopy (OES) is one such monitoring technique that can be used to characterize the temperature and composition of a system by detecting the optical emission radiating from it. In this study, it was used to characterize the plasma arc that was created in the welding process.

This study focuses on developing a reliable OES based monitoring system to study the WAAM process. This study focuses on understanding the physics of the plasma arc and correlating the detected optical emission from the arc to processing conditions like current, voltage and travel speed. This correlation is studied with the help of a self-programmed software that processes the collected optical spectrum and visualizes the processed signal. The research objectives of the study are:

- To study the potential of developing a reliable OES based quality control and monitoring tool for WAAM,
- To design a reliable experiment setup and software tools to process optical spectrum data from the plasma arc,
- To validate the reliability of the setup and software by analysing data from different processing conditions,
- To investigate the correlation between the collected spectrum and the processing conditions and weld characteristics.

## **1.2 Thesis outline**

This thesis presents, in Chapter 2, a general background of some essential concepts, as well as an overview of relevant literature. It details the evolution of manufacturing systems and introduces Wire and Arc Additive Manufacturing (WAAM). The mechanism of the process and its limitations are detailed. The limitations of existing monitoring systems are presented and Optical Emission Spectroscopy is introduced as a potential monitoring system for the quality control of the WAAM process.

Chapter 3 provides a theoretical background of the metal transfer mechanisms used in the WAAM process. It presents a brief overview of plasma physics and introduces the concepts of local thermodynamic equilibrium. The equations and laws governing the plasma state are presented to explain the basis of the spectroscopic characterization techniques used in this study.

Chapter 4 presents the scientific approach and the materials used in the study. It details the WAAM experiment setup and explains the self-programmed software that is used to implement the post-processing algorithms on the spectroscopy data. Spectrometer optimization tests are detailed for optimum positions and observation angle. The experiment setup and developed software are validated by testing them on different experimental processing conditions. The setup for the peak characterization test, heat input ramping test and anomaly detection test are presented.

Chapter 5 presents the results of all the experiments detailed in chapter 4. The processed optical spectrum data is visualized using the developed software and correlations between the OES data and experimental processing conditions are elaborated. For the anomaly detection test, secondary investigation techniques like optical microscopy, high-frequency V-I data and high-speed camera footage is used to validate the OES results.

Chapter 6 presents a summary of the thesis and the conclusions of the study. It also details the possible future directions that can be further researched.

## Chapter 2

# Literature Survey

### 2.1 Evolution of Manufacturing Systems

The evolution of industrial manufacturing relies on innovation in processes, materials and product design. The manufacturing industry traditionally used subtractive manufacturing (SM) techniques to build parts. SM is a top-down approach that successively removes material from a solid block of metal. In most cases the larger block of material is made by casting and then further cut and milled to remove the excess. [1].

Maritime, structural and aerospace manufacturing sectors have regulated standards for product and process quality. They require functional, high integrity engineering products in low volumes, small product development cycles, and shorter production times [2]. With an increasing demand and investment, there was a need to create alternatives to SM with easily upgradable production systems where new technologies and functions could be readily integrated. These alternatives needed to have the following features [3]:

- Reduce the time needed to design, build or reconfigure a manufacturing system to ramp-up to full capacity, high quality production (Rapid prototyping and production),
- Increase the variety in the products that can be manufactured (Design freedom),
- Increase flexibility to manufacturing fluctuating production volumes (Production freedom),
- Reduce the cost of production (lead time, material efficiency).

In addition to material and process considerations, metal manufacturing processes have a significant environmental burden associated with it. Manufacturing processes consume non-renewable resources in the form of metal ores and fossil-oil derived fuels. They are also energy intensive and release solid, liquid and gaseous waste that pollutes the environment when it is not disposed properly [4].

It can be inferred that traditional manufacturing systems are limited by their lack of flexibility and inefficiency with respect to material, energy and time. Although the literature identifies the limitations of SM, it only provides a framework for designing new manufacturing systems and does not always offer a replaceable solution.

## 2.2 Additive Manufacturing

Additive Manufacturing (AM) was identified to be a key technology in the ‘third industrial revolution’ - a new wave of manufacturing technologies characterised by functional software, flexible robots, new processes, and a range of web-based services that addressed the limitations of subtractive manufacturing [5]. The global investment in additive manufacturing technology has seen a near exponential rise, as shown in Fig 2.1.

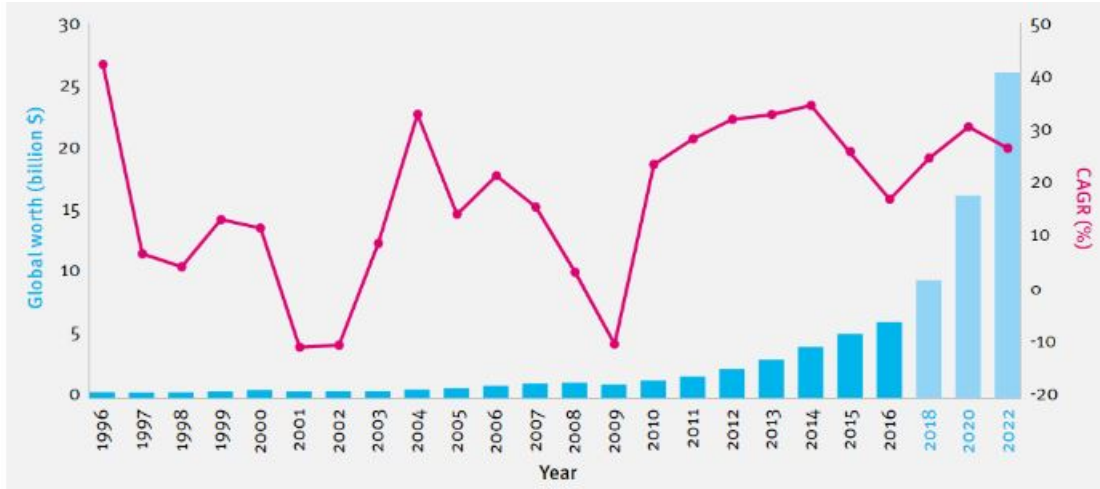


Figure 2.1: Global AM market and Compound Annual Growth Rate [6]

Metallic AM is a term to describe a class of processes that uses a layer-additive approach to design and construct parts, and utilize different heat sources like a laser, plasma arc or an electron beam. They are an extension of rapid prototyping processes that use a bottom-up technique, comparable to stereolithography and welding repair techniques. The metallic AM integrates these rapid prototyping techniques with principles from Computer Aided Design (CAD). The automation of the process enables manufacturers to build structural parts directly from CAD data [7].

In the manufacturing industry, the ‘buy-to-fly ratio’ (BTF) is defined as the weight of raw material divided by the weight of the final component. This index is a measure of how efficient and material intensive a manufacturing process is. For subtractive metal manufacturing processes, the BTF ratio can go as high as 20 [8]. High BTFs are seen in processes where a lot of variables influence the quality of the final part. The metallic AM processes are observed to have a much lower BTF ratio of around 1.2 [9].

### 2.2.1 Rapid Prototyping and Rapid Manufacturing

Rapid prototyping (RP) is a technique used to quickly fabricate a scale model of a physical part or assembly using three-dimensional CAD data. Commercial RP systems have been used by manufacturers as a tool for design verification in various industries like medical, automotive and aerospace. Traditionally, design prototyping was done using methods like casting, machining and injection moulding. With the development of sophisticated software, RP systems are now widely used for its shorter development cycles, higher geometric complexity and customizability of production volume and design [10, 11]



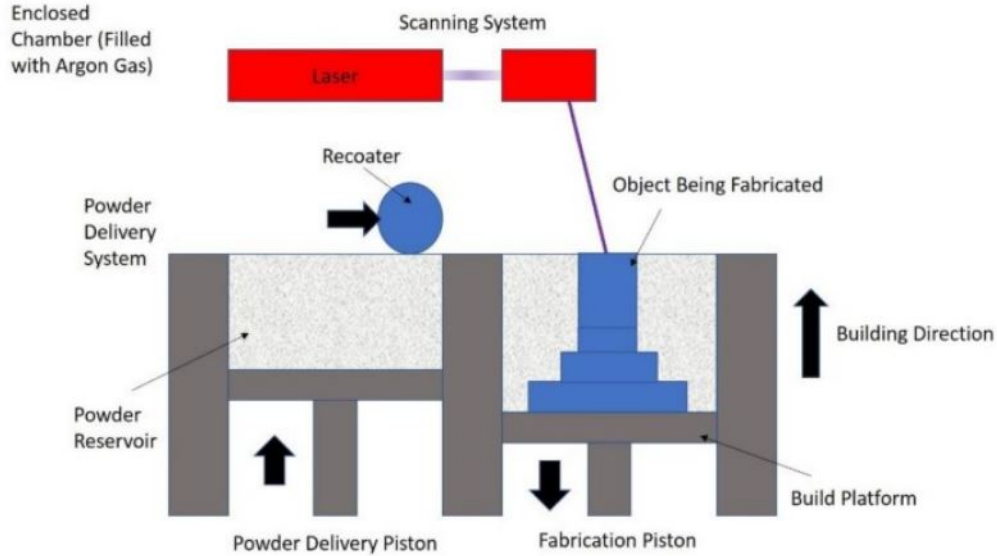


Figure 2.2: Schematic of Selective Laser Melting RP process [12]

RP systems use a layer additive approach to produce solid models by processing sheet, powder or liquid material feedstock. RP systems take the 3D shape data of the component and slice it into layers to generate a tool path. A heat source like a laser is used to melt, agglomerate or sinter the raw material to make a solid representation of the designed component. One such RP process is illustrated in Fig 2.2. RP systems are used as an assessment of the 3 Fs of a design - Form, Fit and Functionality. These systems are also used to manufacture moulds that are used in vacuum and investment casting. Apart from the manufacturing industry, RP is also used in biomedical prototyping, where it sees application in surgery rehearsal and prosthesis design. [13].

Although RP is a quick and inexpensive method for near net shape manufacturing and design visualization, it does not show structural and mechanical functionality. Manufacturing industries wanted to transition from simple prototypes to the direct production of finished products. Increasing demand for cheaper products and new opportunities for engineering design led to the concept of Rapid Manufacturing (RM). RM research was focused on manufacturing metal components which addressed the functional limitations of RP as well as injection moulding and subtractive manufacturing techniques [10].

RM allows geometric freedoms such as variable wall thickness and zero draft (no taper angle), which is not possible in injection moulding. The additive processes used by this technique will also allow for the manufacturing of functionally graded compositions or with embedded electronics that can assist in the monitoring and control of the process. It is to be noted that RM does not offer a good surface finish and thus the component has to undergo post processing to remove surface roughness [14].

The benefits of RM outweigh its limitations and was thus seen as a promising technique for the fabrication and production of functional metallic models that can be used directly as finished products or components [15].

### 2.2.2 Metallic AM

Metallic AM processes are categorized based on the form of raw material used - powder-based (blown or laser bed) and wire-based techniques. In the powder laser bed technique, a laser is focused on a powder bed which selectively fuses layers of the CAD model until the whole part is built. Another technique involved blown powder or a metal wire as the feedstock that forms a melt pool due to a laser or electron beam heat source. In this process, metal layers are formed upon solidification of the molten metal. These AM processes can also be categorized based on their heat source - into arc, laser and electron beam AM. The choice of heat source depends on the desired deposition accuracy, efficiency and build rate of the process [16]. Fig 2.3 illustrates the classification of metallic AM processes.

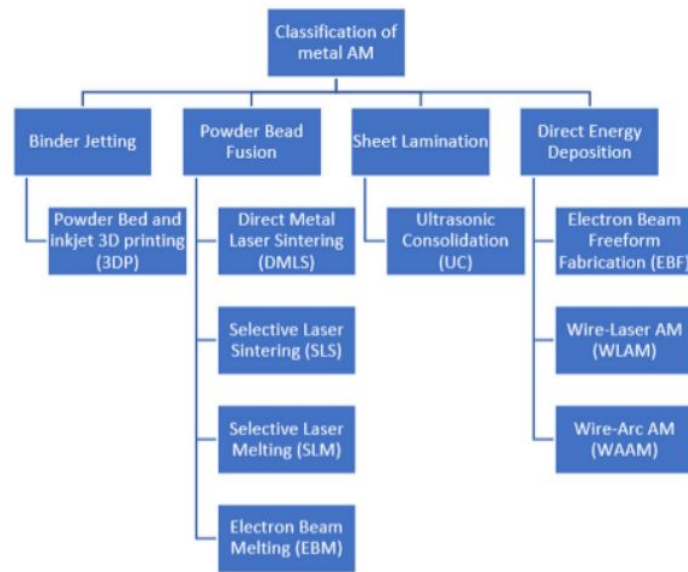


Figure 2.3: Classification of AM systems [17]

Although powder based techniques can produce near net shape products with desired mechanical properties, it has a number of limitations that make it unsuitable for widespread commercial use. These limitations can be summarised below:

- Low build rate, high cost and is limited by the size of the operating chamber [18]
- Metal powders have low capture efficiency between 20-30 percent that results in energy wastage [19]
- They have lower densities and require post processing like isostatic pressing to get higher densities and better mechanical properties [20].
- Metal powders are susceptible to contamination from carbon, hydrogen, nitrogen and oxygen resulting in low quality, defective parts [21]
- Metal powders are harder to recycle compared to metal wires [22]
- Laser sources have a poor energy conversion of 10 percent, which is exacerbated by the high reflectivity of metals which making Copper and Aluminum parts [23, 24]

Numerous studies have been done comparing the quality of products made from the different forms of raw material. It is seen that a coaxial powder feeding combined with a lateral wire with the same laser heat source results in an increase in deposition efficiency and also contributes to a better surface finish [25]. Another study investigated powder and wire feedstock separately by building two walls with a height of four layers. It is seen that a wire source has a greater deposition efficiency. The wire source also had a less perturbed melt pool, which led to a better surface finish and lesser microstructural imperfections [26]. These studies concluded that a wire feed source was better than metal powder in RM processes. Similar studies were done to investigate the effect of the heat source in the process. While a laser heat source was effective on metal powders, they showed limited application on a wire source. These limitations can be summarized below:

- The energy absorption coefficient of the wire is inhomogeneous and results in an inefficient energy coupling between the laser and the material [27],
- The tension of the wire is not uniform and thus causes vibrations and bending that perturb the melt pool and result in a poor surface finish [28],
- Automation of the process is hindered by the high sensitivity of the wire orientation with respect to the laser [28],
- Excessively high dilutions are observed, with a nearly 15 percent difference between wire and powder sources [29].

These limitations indicated that although a wire feed source was superior to the available alternatives, an alternate, cheaper and more automatable heat source was needed. Researchers investigated the possibility of modifying arc welding processes like Gas Metal Arc Welding (GMAW) and Gas Tungsten Arc Welding (GTAW) to produce near net shape products that had superior mechanical properties and had the potential of manufacturing engineering parts with high structural integrity and low costs. Wire and Arc Additive Manufacturing was such a process that addressed the limitations of laser-based solid freeform fabrication techniques and had the potential for widespread adoption.

## 2.3 Wire and Arc Additive Manufacturing

Wire and Arc Additive Manufacturing (WAAM) is a subcategory of AM. It uses a metal wire as the feedstock, and an electric arc as the heat source, thereby combining both welding and additive manufacturing techniques. Similar to Gas Metal Arc Welding (GMAW) and Metal Inert Gas welding (MIG), the process utilises a welding torch, a power source, metal wire, and a shielding gas. It also has either a robotic system or a gantry system that controls the movement of the torch to build functional products that are near net-shape [30].

The end of the 20th century saw an increase in the research and development of new manufacturing technologies that could be used as alternatives to SM. Though the term Additive Manufacturing has been in use only in the last 20 years, it was known by different names like solid freeform manufacturing, shape welding, shape melting, rapid prototyping and 3D welding.

### 2.3.1 History of WAAM

The first advancement in WAAM was a patent was filed for the superposed deposition of metal using a fusible electrode. Successive adjacent beads were deposited in a layered manner by means of a consumable electrode in a shielded arc welding process. It was made for ornamental purposes and did not have any industrial application [31]. This patent spurred further investigation to improve the functionality of the final product and still be economically viable. An early version of WAAM was used in the cladding of retorts, which needed to be operated in a high temperature environment susceptible to oxidation and corrosion [32]. This patent was the first to identify the importance of process monitoring and the effect it had on the mechanical properties and microstructure of the final part in WAAM.

The process saw further development when a method to fabricate thick-walled circular pressure vessels was patented [33]. This process had a higher deposition rate for a fraction of the cost of traditional SM processes that needed pressers, rollers and furnaces to be built. The improvement of the mechanical properties of the product could be attributed to controlled solidification and forced cooling and tempering due to progressive deposition. Numerous experimental studies followed this in order to integrate this new technology into manufacturing units capable of low cost mass production. In 1976 a method to fabricate large high quality rotors for turbines and generators was published [34]. The author noted that homogeneous, isotropic properties could be obtained with suitable process monitoring of heat input and temperatures to ensure optimum operating conditions. Another study showed that high volume parts could be fabricated in a tandem system with multiple welding heads and could achieve a deposition rate of 20 kg/hr [35]. Mechanical and fracture testing of these WAAM (then called shape welding) products showed superior ductility, tensile strength, toughness and fracture resistant properties in comparison to products manufacturing by SM [36].

The end of the 20th century saw the development of the process facilitated by advancement in computer technology. An online point-to-point program was used in tandem with GMAW to deposit an unsupported wall in a layer additive technique. It also led to the creation of the Initial Graphics Exchange Specification (IGES) format to optimize slicing algorithms of the final part [37]. Advancements in speed, slicing algorithms and improved monitoring and control paved the way for industrial adoption of WAAM for manufacturing metallic products [38].

The literature indicates that WAAM initially did not seem like a promising manufacturing technique that could replace casting and milling. However, the potential for automation was recognized and research was carried out to improve the process. Process monitoring was identified to be an important step towards improving the quality of the parts produced. More sophisticated sensors, hardware and software to process large amounts of data has significantly advanced our understanding of WAAM sub-processes and how materials behave. However, only some metals were studied extensively and process controls that worked for one material did not necessarily work for all due to different physical and chemical properties [39, 40, 41].

### 2.3.2 WAAM process conditions and workflow

Modern WAAM systems offer flexibility in path design, material choice, variation in process parameters and customizable monitoring and control systems. This process begins with the design of the required part to be built. A 3D CAD model of the desired part is input into the AM software, which generates a series of 2D contours stacked on top of each other in

layers. This constitutes the ‘tool path’, a set of directions followed by the welding torch to deposit the metal. The wire feed speed (WFS)/ welding current, welding voltage, welding speed, interlayer temperature and interpass time are known as the process parameters and control the process. They are decided based on the wire material, the desired microstructure and mechanical properties of the final part [30].

The first bead of metal is deposited on a substrate, followed by successive layers that are deposited on top of each other. Post processing involves machining out the substrate followed by the heat treatment of the final product to give a good surface finish and desirable mechanical properties. Each of these steps can be broken down into sub-processes which contribute to the quality of the final product [42]. A schematic representation of the WAAM process is shown below in Fig 2.4.

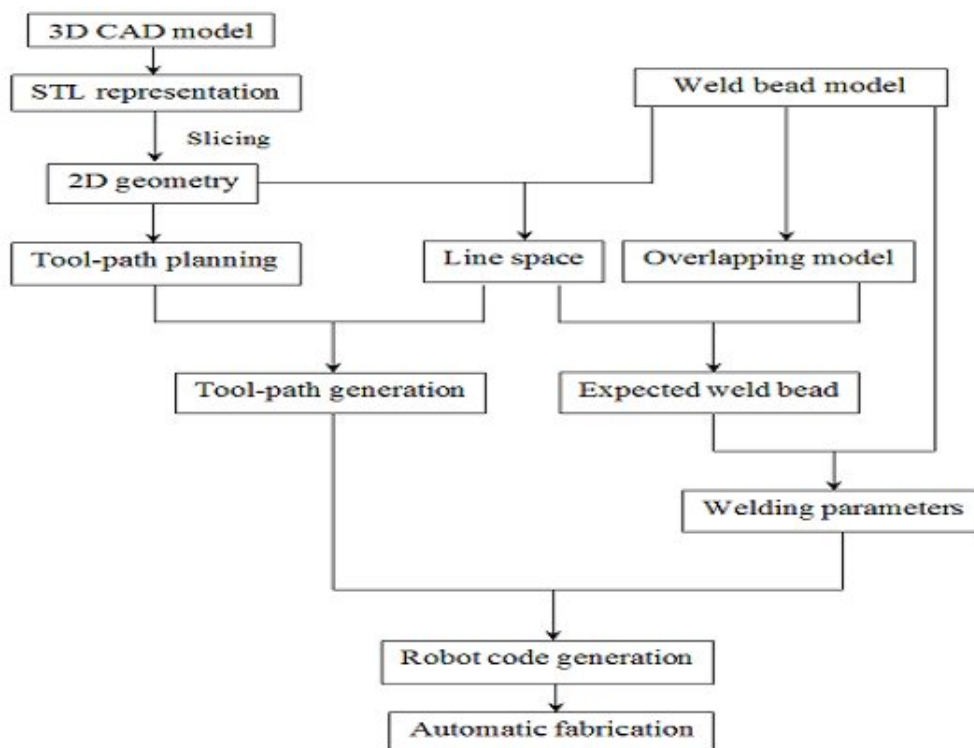


Figure 2.4: Schematic of WAAM process [30]

### 2.3.3 Optimizing WAAM system

Though the operating principles of WAAM hasn't changed, development of better hardware, algorithms and sensing equipment resulted in improved monitoring and control systems for process optimization.

Optimized slicing algorithms ensure that individual layers constitute parts of higher quality [43]. Modelling techniques have been investigated to optimize tool paths by considering the thermo-mechanical cycles a material undergoes [44]. Process parameters have the most significant effect on the surface appearance and material properties of the build. It is found that increasing the inter-layer temperature increases the surface roughness and reduces the build height in some cases [45]. Increasing the WFS decreases the stability of the arc and melt pool thereby reducing the surface quality [45]. The microstructure of the build can be

manipulated when rolling is done in conjugation with deposition [46].

It can be concluded, from reviewing these studies, that WAAM is a complex process with many variables, all of which contribute to surface finish, material properties, microstructure, and overall quality of the part.

## 2.4 Limitations of WAAM

Although WAAM addresses some limitations of subtractive manufacturing, its sub-processes require further optimisation before it sees widespread adoption. Inhomogeneous heat input in a dynamic solidification environment, where remelting, fluid flow, and material evaporation occur concurrently can cause the formation of microstructural anomalies that affect the quality of the final part [42]. Some of these anomalies are discussed below.

### 2.4.1 Cracking

Different physical factors and process parameters cause crack formation in the build. Gradients in surface tension caused by the movement of the melt pool can cause the formation of surface cracks. Differences in thermal properties between the substrate and wire material can create thermal gradients which leads to crack formation. These cracks are also formed when there is a thermal gradient in the melt pool during solidification, and is also called ‘hot tearing’. These thermally induced stresses can exceed the strength of the material at elevated temperatures [47]. The presence of these defects depends on the materials used as well as the melting trajectory of the melt pool and the thermal expansion coefficients. The mechanism of crack formation is illustrated below in Fig 2.5.

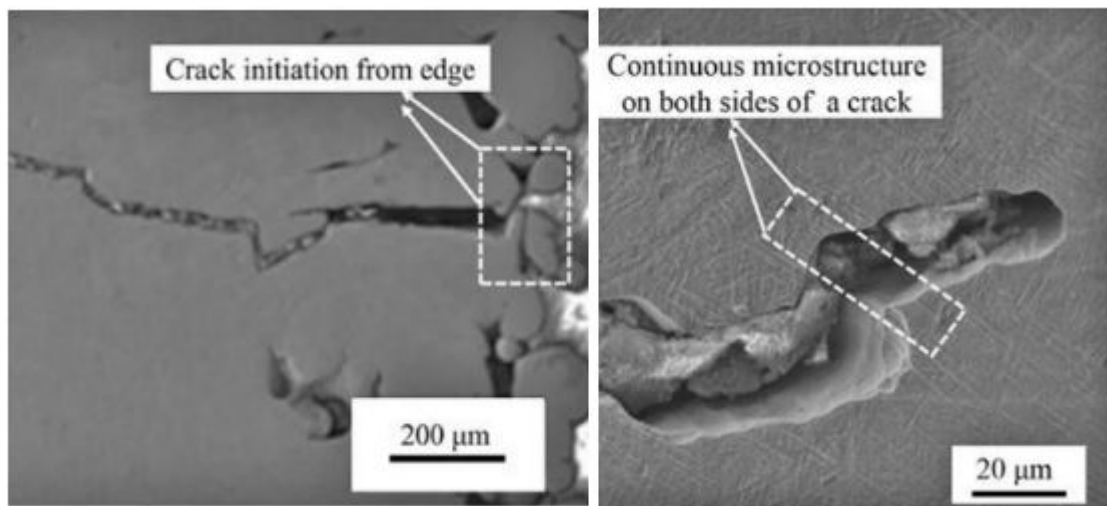


Figure 2.5: Mechanism of crack formation [48]

### 2.4.2 Porosity

Porosity is a common defect found in AM parts and can occur across varying length scales. It can be caused by trapped shielding gas surrounded by a solidifying melt pool. Another mechanism called the Marangoni flow can occur, where a surface tension gradient along a liquid interface causes gas retention bubbles within the melt pool leading to the formation

of pores, as shown in Fig 2.6 [49]. The effect of scanning speed on porosity has also been investigated by Meier et al. The study showed that a higher scanning speed creates a surface with more roughness and fragmentation. Since a new layer is built on the rough surface of a previously deposited layer, the build is more susceptible to the formation of entrapped defects and melt pool instability. [50].

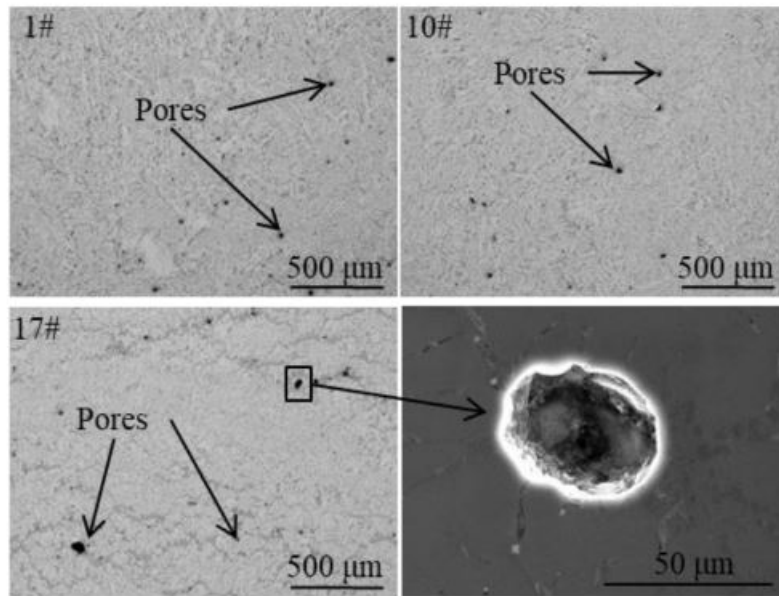


Figure 2.6: Porosity in WAAM [42]

### 2.4.3 Lack of Fusion

When the melt pool does not have sufficient energy, the inability to melt the metal particles can cause a lack of fusion in AM parts. They are usually found along layer boundaries, are irregularly shaped and often contain insufficiently melted metal particles. The dynamic cooling environment of the melt pool can also cause the selective evaporation of some elements which leads to a reduction in the density of the part. They form irregular pores when the overlap between adjacent layers is not enough to create stable metallic bonding, as shown in Fig 2.7. It is found that an increase in scanning speed results in a higher probability to find these defects due to a decrease in the specific energy. Selecting appropriate process parameters that are optimized for the materials used in the process can prevent the formation of these defects [51].

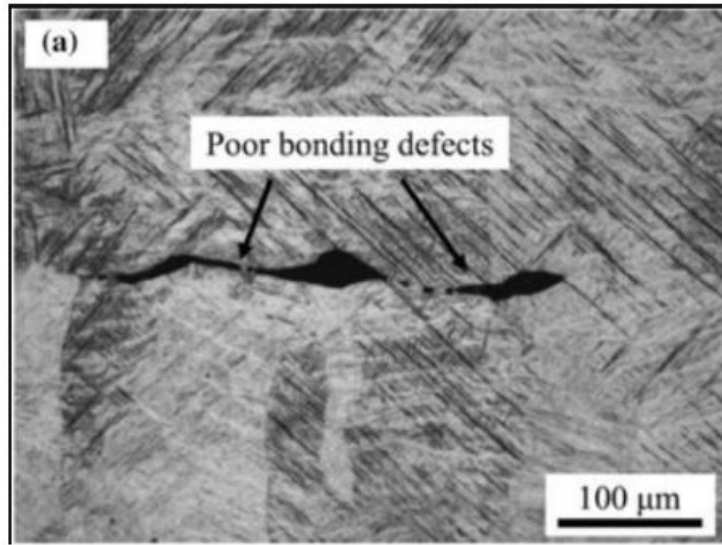


Figure 2.7: Lack of Fusion defect in AM [42]

#### 2.4.4 Inclusions and Phase Instability

A chemical reaction between the deposited metal layer and shielding gas can result in the formation of intermetallic particles like oxides and sulfides, as illustrated in Fig 2.8. These inclusions can be up to 1 mm in size and have an effect on mechanical properties like fatigue, fracture toughness and ductility [52]

Temperature gradients found in the melt pool causes spatial variations in the solidification rate, which has an effect on the microstructure and phase stability. Variation in travel speed also causes change in grain structure and the formation of metastable phases distributed in the microstructure [53, 54]

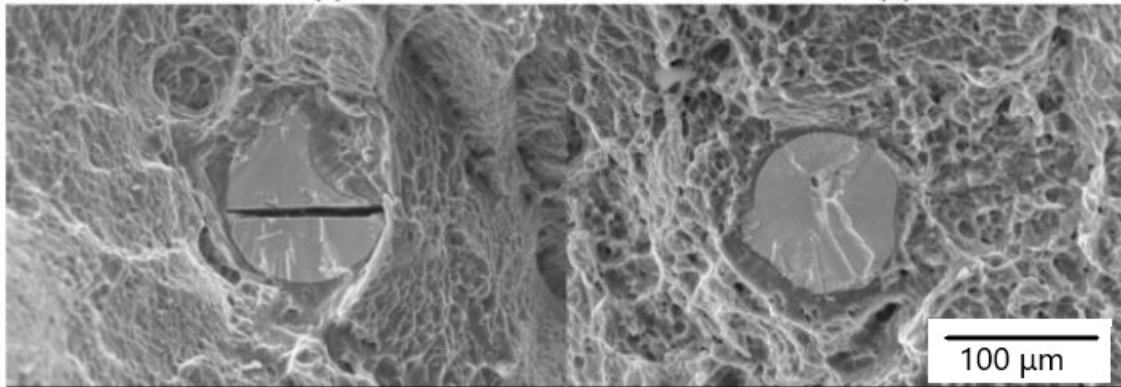


Figure 2.8: Oxide inclusions in AM part [55]

The complexity of the process and the inhomogeneity of the observed defects are challenges that need to be addressed in order to fabricate high quality structural parts. The presence of these defects are strongly material dependant and originate from different sources and are found in varying length scales. These inhomogeneities should be taken into consideration



while designing process monitoring systems, where different kinds of process abnormalities are able to be detected by different subsystems in real time.

## 2.5 Monitoring and Control

Mechanical testing, failure analysis and microstructure investigation is done only after a component is fully built. Building defective parts increases the material usage, power consumption, build time, and overall cost of production. Thus, real time detection of process and product anomalies not only saves money and material but can also improve the quality of the part. Necessary interventions and repairs can be in place to prevent the defective build. Feedback based control systems have the potential to dynamically adjust process parameters in order to build defect free parts [56].

These monitoring systems are based on the detection of a physical parameter that is known to influence the formation of a defect, and thus implying that understanding the defect formation mechanisms are important to design monitoring systems to avoid them. The following section discusses some of these systems.

### 2.5.1 Thermal based monitoring

These systems utilize the detection of heat or temperature in order to monitor the quality of the process. Infrared sensors have also been used to study the correlation between process parameters and weld bead geometry [57]. Special pyrometers have been used to monitor surface temperatures in order to be able to control the melting and solidification of the material [40]. A Complementary Metal Oxide Semiconductor (CMOS) camera based monitoring system was used to scan the shape of the weld pool in real time and fed into a FEM model which predicts the shape and temperature of the clad layers [41]. Infrared camera detection of process errors resulting from insufficient dissipation of heat has been used to identify pores and fusion defects [58].

### 2.5.2 Electromagnetic signal monitoring

These monitoring systems detect electro-magnetic signals across different wavelength scales to characterize process anomalies. A dual frequency electro-magnetic sensor was used to evaluate the extent of dilution between the build and the substrate, and is illustrated in Fig 2.9, where the sensor response varies with the extent of dilution [39]. Arc force, weld width, and penetration have been studied as a function of welding current using 2D X-Ray radiography [59]. 3D scanning cameras are also used to map AM builds and dynamically adjust process parameters and deposition rate based on the geometric profile of previously deposited layers [60].

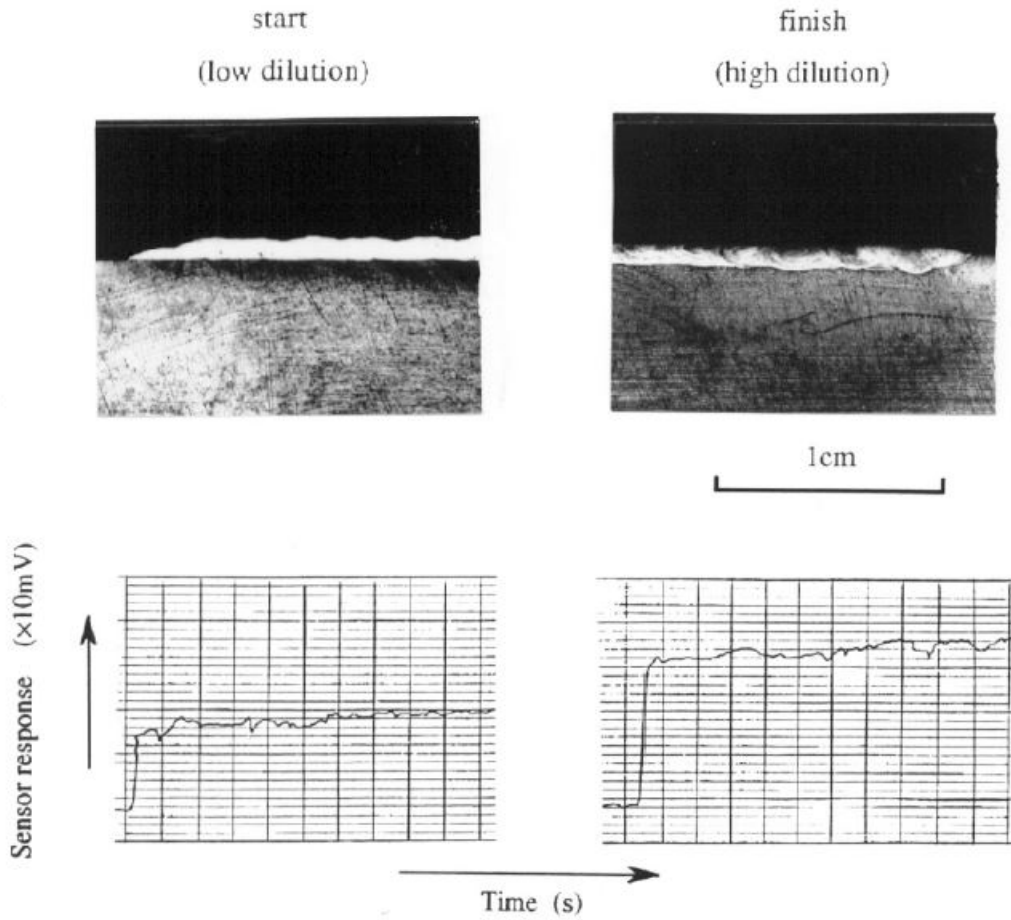


Figure 2.9: The differential dilution sensor response to continuous variation of laser cladding dilution in real time [39]

Correlating the effect of process parameters on the quality of the process, both individually and in tandem with each other, is an important feature of a monitoring system. The next section of this study focuses on one such system which characterizes the light emitted from the plasma arc in order to evaluate processing conditions.

## 2.6 Optical Emission Spectroscopy

In the last two decades, Optical Emission Spectroscopy (OES) has emerged to be a promising technique to monitor additive manufacturing and arc welding processes. The electromagnetic radiation emitted by the plasma arc is correlated with the processing conditions in order to characterize a process or product. It has been used to characterize plasma in a variety of manufacturing processes as a means for monitoring and control. The main advantages of OES is the high spatial resolution of the obtained signal and the ability to detect signals and process data in real time [61]. OES has seen applications in monitoring a multitude of manufacturing processes like semiconductor synthesis, gas metal arc welding, laser ablation, laser cladding and chemical vapour deposition [62, 63, 64, 65]

### 2.6.1 OES for monitoring and control

The existing studies that have investigated the use of OES as a monitoring tool for AM/welding processes have focused on establishing a correlation between the optical spectrum and processing conditions or the finished product. These studies are largely exploratory in nature and do not provide a reliable solution to develop an OES based monitoring system for commercial AM systems. Cerrai et al determined the relationship between the grain size and observed spectral line intensity of the metal sample. It concluded that grain boundaries enabled a more efficient distribution of energy into the bulk, thereby increasing the probability of a metal atom to vapourize [66]. The plasma temperature has been used to determine the quality of overlap builds during laser welding, by correlating it with the extent of metallic bonding. The spectroscopic observations have also been validated by microstructure studies [67]. OES has also been used to identify phase transformation in direct metal deposition by detecting the early stage of nucleation in alloy systems [68]. The temperature and concentration profile of the plasma generated in GMAW has been studied using OES [69]. Line intensity profiles of TIG welding have been used to evaluate the arc stability and detect anomalies in the welding environment [70]. Further applications of OES monitoring systems have been investigated for powder bed and laser deposition AM processes [71, 72].

### 2.6.2 Limitations and Knowledge Gaps

All the studies that analyse the use of OES in AM are focused on powder bed and laser deposition processes, with no study directly focused on the use of OES to characterize the WAAM process. The nature of the optical emission and the mechanism of plasma creation and metal transfer are different in WAAM, which has not been investigated before. The spectroscopic studies of processes similar to WAAM like MIG/MAG welding were limited to identifying plasma temperature and phase changes, and were focused on understanding the temperature and concentration profiles of the plasma arc. OES has been studied as a tool for quality control in TIG welding by correlating the optical spectrum with the arc length in order to detect anomalies and evaluate arc stability. However, the experiment setup uses a fixed spectrometer and a moving base table, which limits the application of this method to small scale studies. Although the studies established correlations between the OES signal and processing conditions, they did not provide any solution for handling and processing the large amount of data that is detected by the spectrometer during the process.

Monitoring systems require a robust setup that can collect reliable and repeatable data if it is to be used for quality control. A review of the state of the art indicates that OES is a feasible method to study arc radiation, but there is currently no application of this technique in a reliable monitoring system for commercial application. The application of plasma spectroscopy in arc welding has been focused more on understanding the plasma, without much focus on its application for quality control. Thus, there is potential to develop a reliable OES-based monitoring system that can be used to investigate the processing conditions and correlate them with the detected optical signal for quality control.

## 2.7 Objectives of this study

Above all, the state of the art indicates the feasibility of using OES to correlate optical emission signals to processing conditions of metal deposition and arc welding. This study

focuses on developing a reliable OES based monitoring system to study the WAAM process. This study focuses on understanding the physics of the plasma arc and correlating the detected optical emission from the arc to processing conditions like current, voltage and travel speed. This correlation is studied with the help of a self-programmed software that processes the collected optical spectrum and visualizes the processed signal. The research objectives of the study are summarised as following:

- Study the potential of developing a reliable OES based quality control and monitoring tool for WAAM,
- Design a reliable experiment setup and software tools to process optical spectrum data from the plasma arc,
- Validate the reliability of the setup and software by analysing data from different processing conditions,
- Investigate the correlation between the collected spectrum and the weld characteristics.

# Chapter 3

## Theory

### 3.1 Introduction

During the Wire Arc Additive Manufacturing (WAAM) deposition process, electric arc energy is supplied either through a consumable electrode used in Gas Metal Arc Welding (GMAW) or non-consumable electrode used in Gas Tungsten Arc Welding (GTAW) to the feeding wire and substrate. The feeding material (welding wire) melts and gets transferred into the melt pool which is induced by the electric arc. As the electric arc travels away, it results in a weld track/bead during the melt pool solidification. A welding torch is used to generate the electric arc and integrated on either a robotic arm or a gantry system and controlled by a power source. The WAAM deposition process or WAAM 3D printing is a CNC (Computer Numerical Control) additive process, in which the deposited weld tracks/beads are programmed as a toolpath and a 3D object can be produced layer-by-layer [73, 74].

A plasma (a collection of electrons, ions, molecules and atoms) forms between the electrode and the melt pool which can emit electro-magnetic radiation (in the visible spectrum) due to electronic transitions [75]. Metal atoms evaporate from the melt pool and further get ionised within the formed plasma. The optical emission is detectable using a spectrometer and it can be further characterized in order to monitor and control the process [75].

The following sections provide a theoretical background on the metal transfer mechanism in the WAAM process and the creation of the plasma arc. The physics behind the optical emission spectroscopy techniques used to characterize the electromagnetic radiation emitted from the plasma arc are also discussed in further detail.

### 3.2 Metal Transfer Mechanisms

Metal deposition in WAAM follows the same metal transfer mechanisms as Gas Metal Arc Welding (GMAW). In this technique, the feeding wire changes phase due to the input energy, which results in the formation of a liquid droplet at the tip of the wire. The liquid metal drop grows and gets detached from the wire. This process of droplet formation, detachment and transfer in the arc plays an important role in determining the weld quality and process stability. The metal transfer process is classified according to the size, frequency and characteristics of the transferred droplet. There are 3 broad modes of metal transfer [76]:

- Short-circuit mode: Repeated short circuits facilitate metal deposition when the liquid drop at the tip of the wire bridges the gap between the wire and the substrate,

- Globular mode: Large, irregularly shaped drops are transferred across the arc at a low average current,
- Spray mode: A stream of tiny molten droplets is sprayed across the arc at a high frequency from the wire to the substrate as a result of a high average current.

In this study, a Super Active Wire Production (SAW-P) mode was used for metal transfer. It is a proprietary technique developed by Panasonic that is based on the short-circuit metal transfer mode. The creation of the plasma depends on the mode of metal transfer between the wire and the base plate. The following section will elaborate on the short-circuit transfer mode in order to understand the mechanism of plasma creation to characterize optical emissions using OES.

### 3.2.1 Short-circuit Metal Transfer

In this transfer mode, a current and voltage input is passed through the wire, creating a plasma arc between the wire and base plate. The plasma causes the tip of the wire to melt and form a drop of liquid metal. This drop bridges the wire and melt pool in the base plate, resulting in the plasma arc no longer being present. The current passing through the wire increases, and is accompanied by an increase in the magnetic force at the tip of the wire. The electromagnetic force surrounds the wire tip and provides the ‘pinching’ force that squeezes the molten droplet from the tip of the wire. This pinch force and the surface tension of the liquid metal combine to detach the metal droplet from the wire. The arc then reestablishes itself and the whole process repeats between 20-200 times a second [77].

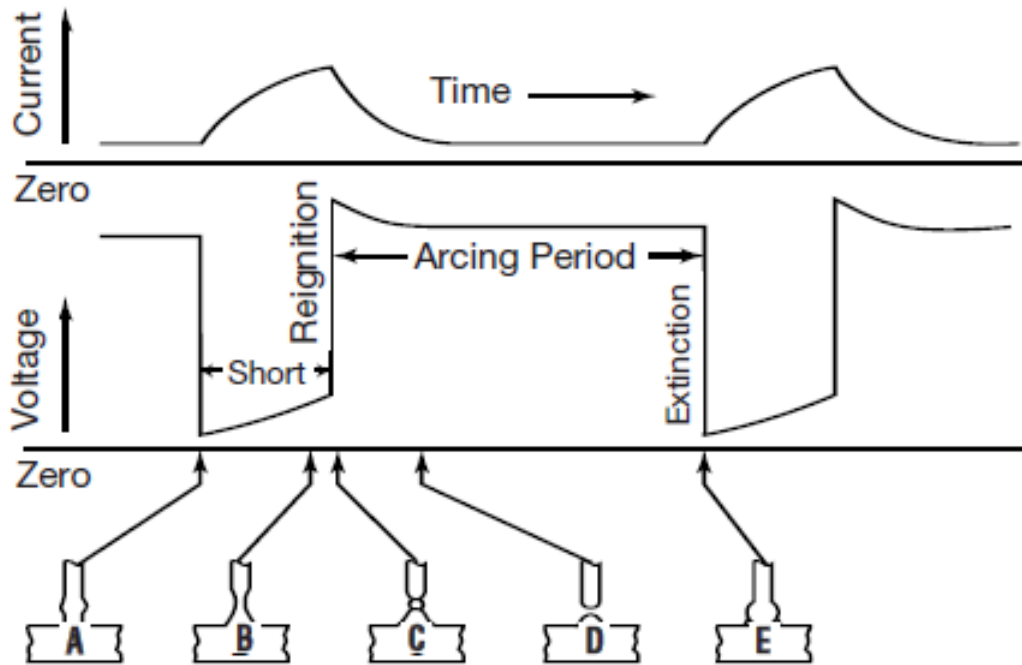


Figure 3.1: Oscillogram of short-circuit transfer [76]

Fig 3.1 shows the stages of metal transfer at different V-I conditions. In stage ‘A’, the wire makes physical contact with the melt pool/substrate, which marks the start of the short

circuit. Current flows through the electrode wire and the voltage goes to zero in the absence of the plasma arc. In stage ‘B’, the heat of the current flow causes a magnetic field to envelope the electrode wire. As the current increases, the heat due to wire resistance causes the wire to melt and start to neck. The voltage slowly increases and the current continues to climb to a peak value. In stage ‘C’, the molten droplet is forced from the electrode tip. The current reaches a maximum value. The droplet finally detaches in stage ‘D’ due to the magnetic pinching effect and the surface tension of the melt pool. The arc reignites after the droplet is detached and stage E shows the process repeating itself again.

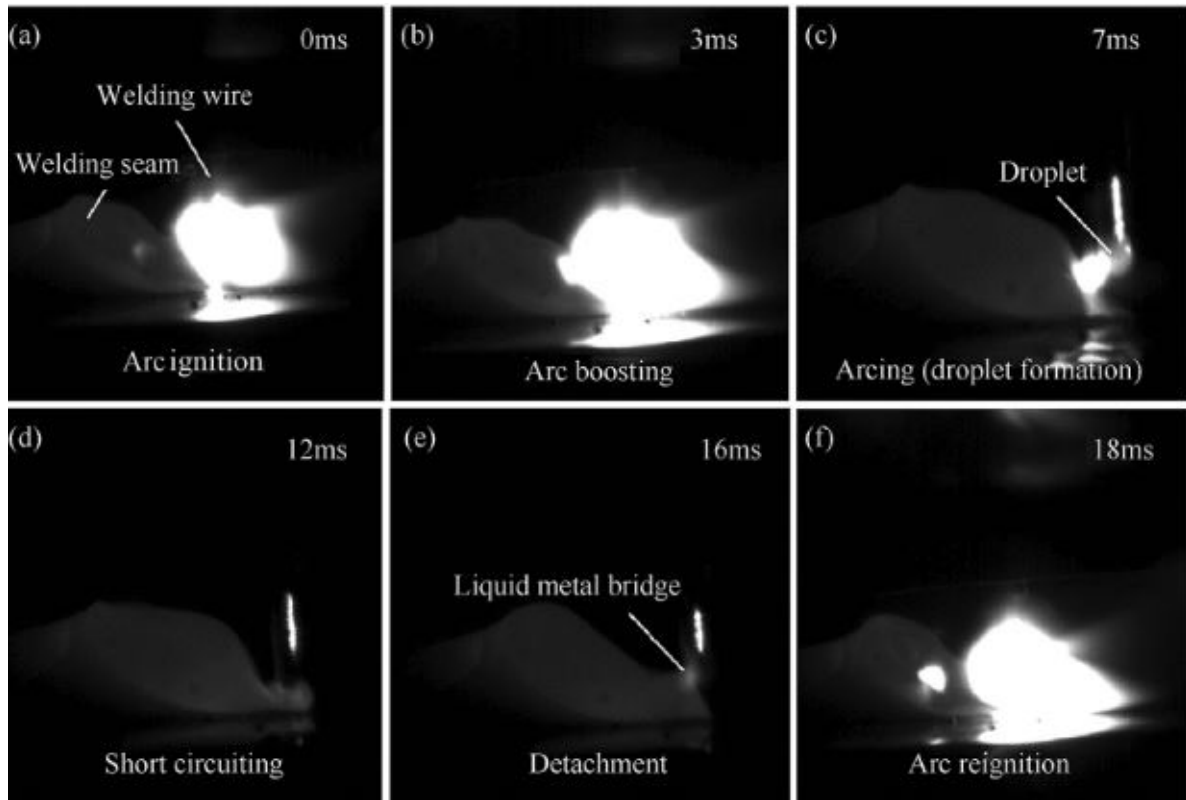


Figure 3.2: High speed camera images of metal transfer process in short-circuit transfer [78]

In this study, a Super Active Wire Production (SAWP) mode was used, which is a modification of short-circuit metal transfer mode. In this technique, the metal droplet detachment is assisted by a wire motion control servo motor. The system first detects a short circuit. After the short circuit is detected, the servo motor of the welding torch is reversed by digital process control, causing the retraction of the wire. This gives the weld more time to cool after each drop is detached compared to the short-circuit mode. The system used in this study integrates the retraction of the electrode, measures and controls the arc length, and the polarity of the welding current. This results in the formation of a relatively spatter-free smooth weld.

The optical emission radiated from the plasma arc can be detected and characterized. The following sections provide a theoretical background for the diagnosis of the plasma arc.

### 3.3 Thermodynamic Equilibrium

A homogeneous plasma's physical state contained in a vessel with isothermal walls at a temperature  $T$  is said to be thermodynamic equilibrium (TE) when its physical state can be described as a function of macroscopic properties like pressure, temperature and concentration its constituent species without complete knowledge of all the processes at smaller length scales [79]. For different plasma species the energy, velocity and particle distributions are governed by a deterministic set of equations. The velocity distribution of particles obeys the Maxwell equation. The Boltzmann and Saha equations define the excited state and level of ionization in the plasma. The spectral distribution of the electromagnetic radiation is governed by Planck's Law [80].

#### 3.3.1 Maxwell's Equation

This equation governs the velocity distribution function of the particles in the plasma. In this formulation, the change in particle density  $dN$  (any type of particle) that has a velocity in the range of  $v$  to  $v + dv$  is described by:

$$dN = Nf(v)dv \quad (3.1)$$

where  $N$  is the density of the particular species of particle considered.  $f(v)$  is the Maxwell velocity distribution function, which is formulated as:

$$f(v) = 4\pi r^2 \left( \frac{m}{2\pi kT} \right)^{3/2} \exp \left( \frac{-mv^2}{2kT} \right) \quad (3.2)$$

where  $m$  is the mass of the particle,  $T$  is the plasma temperature and  $k$  is the Boltzmann constant [75].

#### 3.3.2 Boltzmann's Law

This equation governs the population of the energy states in an atom or a molecule. If  $N_1$  and  $N_2$  are the densities of a given species of particles distributed in energy levels  $E_1$  and  $E_2$ , Boltzmann's law is formulated as:

$$\frac{N_2}{N_1} = \frac{g_2}{g_1} \exp \left( -\frac{E_2 - E_1}{kT} \right) \quad (3.3)$$

where  $g_1$  and  $g_2$  are the statistical weights of energy levels 1 and 2 at a temperature  $T$  [81].

The statistical weight  $g_1$  is also defined as the state density of an energy state  $E_1$ . It is related to the total angular momentum quantum number  $J$  - the sum of spin and orbital angular momentum quantum numbers. The total kinetic moment of a particle is equated to  $J_1$ , which is related to the statistical weight of the  $i$ -th level  $g_i$  by [81]:

$$g_i = 2J_1 + 1 \quad (3.4)$$

The particle density of the  $i$ -th energy level  $N_i$  at an average plasma temperature  $T$ , can be related to the total particle density  $N$  by the following equation:



$$N_i = N \frac{g_i}{U(T)} e^{-E_i/kT} \quad (3.5)$$

where  $U(T)$  is called the partition function, which acts as a normalization factor in the equation. This function is given by [81]:

$$U(T) = \sum_i g_i e^{-E_i/kT} \quad (3.6)$$

### 3.3.3 Saha's Equation

The generalization of Boltzmann's law for continuous states leads to the formulation of the Saha equation. This expression relates the ionization state of a gas in thermal equilibrium to the temperature. This expression is given by:

$$\frac{n_e^2}{n - n_e} = \frac{2}{\lambda^3} \frac{g_1}{g_0} \exp\left(\frac{-\epsilon}{kT}\right) \quad (3.7)$$

where  $n_e$  is the density of electrons,  $n$  is the total density of the gas with an ionization energy  $\epsilon$  at a temperature  $T$ .  $\lambda$  is the thermal De Broglie wavelength of an electron, and  $g_1$  and  $g_0$  are the statistical weights of the energy levels 1 and 2 respectively [81].

### 3.3.4 Local Thermodynamic Equilibrium

A state is said to be in thermodynamic equilibrium (TE) if its spatial and temporal temperature gradient is 0. For plasma systems, it represents an ideal set of conditions that are only observed in high-volume systems like in stellar bodies where large volumes can be seen at high temperatures. In smaller laboratory scales, these ideal conditions do not hold due to loss of radiation by the plasma. However, the local thermodynamic equilibrium (LTE) conditions can be assumed, where the plasma has a spatial temperature gradient but does not change as a function of time. The plasma physics laws governing total TE can also describe LTE, except Planck's law governing radiation, which is reformulated with a modified set of conditions. In this radiation field, the temperature  $T$  from the Saha equation (Equation 3.7) is equated to the temperature  $T$  from the Maxwell distribution (Equation 3.2) [82].

In an ideal plasma, an equilibrium is maintained between emission, absorption and photo recombination processes. Since radiation escapes from the plasma, emission dominates over photo-radiative processes, disturbing the equilibrium. The higher energy levels are weakly populated due to the absence of radiation compared to the overcrowded fundamental level. It is assumed that the depopulation rate of an energy level due to electron-electron collisions is greater than de-excitation, ionization and recombination processes due to the high electron density. LTE condition is said to be satisfied when the collisional depopulation rate of the atomic energy levels is greater than the radiative depopulation by a factor of 10 [83]. The minimum electron density needed to satisfy LTE is given by the McWhirter's criterion. Although the LTE condition is not experimentally validated for this study, numerous other studies have shown that McWhirter's criterion is satisfied in metal arc or laser induced plasmas and emission spectroscopy techniques can be used for plasma diagnostics by assuming LTE conditions [67, 68].

### 3.4 Plasma Diagnostics

The emitted radiation from the plasma arc forms a spectrum across a wavelength range. This radiation is a combination of the following components:

- **Line radiation:** It corresponds to radiation from transitions of electrons between levels in atoms and ions, and at low temperatures also in molecules. These are also called bound-bound transitions because they originate from electrons that are still bound to the ionized species. They show as discrete lines in the emission spectrum.
- **Recombination radiation:** It originates from the recombination of electrons with ions. These are also called free-bound transitions and are observed as continuum radiation in the emission spectrum.
- **Bremsstrahlung radiation:** This is seen when electrons emit radiation on being deflected in an electric field of the ions in the system. They are called free-free transitions and are also observed as continuum radiation in the emission spectrum.

The existence of discrete emission lines in the observed spectrum indicates the presence of a particular atomic species, with the wavelength of emission line acting as a fingerprint of the species. The atomic species is usually an element in its most common ionization state. The intensity of the detected radiation depends on the electronic structure as well as the kinetics of the observed plasma. The process of plasma diagnostics involves identifying the species involved from the wavelength and extrapolating properties like electron temperature and concentration from the intensity profile [75].

#### 3.4.1 Line Intensity Ratio

An emission line is defined as the energy emitted per second. In the diagnostics of plasma, LTE conditions are assumed to be valid, as discussed in 3.3.4. Enforcing this criteria assumes that the bound-bound electron collision processes dominate over free-bound and free-free electron transitions. The decay of the electron from the higher energy state  $E_2$  to the lower energy state  $E_1$  releases a photon of wavelength  $\lambda$ . This wavelength of the emission line is determined by the relation:

$$\lambda = \frac{hc}{E_2 - E_1} \quad (3.8)$$

with  $h$  and  $c$  being the Planck's constant and the speed of light in vacuum respectively [84].

The first step in the characterization of the plasma is the identification of the atomic species. This was done by calculating the wavelength of the emission line as mentioned above. The intensity of an emission line depends on the population of electrons in each energy level and the probability of transitioning between the two energy levels. The electron density in the higher energy state is represented by  $N_2$  and the probability of transition is represented by  $A_{21}$ , the Einstein coefficient for spontaneous emission. The emission intensity is given by:

$$I = A_{21} h \nu_{21} N_2 \quad (3.9)$$

It is convenient to express the electron density of  $i$ -th level  $n_i$  as a fraction of the total number density  $n$ :

$$\alpha_i = \frac{n_i}{n} \quad (3.10)$$

Thus, the Intensity Ratio (IR) of two emission lines can be expressed by the equation below, with the subscripts denoting the atomic constants of the selected peaks.

$$\frac{I_2}{I_1} = \frac{\nu_2 A_2 \alpha_{i,2}}{\nu_1 A_1 \alpha_{i,1}} \quad (3.11)$$

This ratio is independent of  $n$  and only depends on the electron density of the chosen emission peak and is easily measurable, as  $I_1$  and  $I_2$  are measured in the same experimental conditions. The ratio  $r_{21} = \frac{\alpha_{i,2}}{\alpha_{i,1}}$  is an exponential function of temperature, and is given by:

$$r_{21} = \rho_{21} \exp\left(\frac{-E_{21}}{kT}\right) \quad (3.12)$$

with  $\rho_{21}$  as a constant or a weak function of temperature. The intensity ratio  $\frac{I_2}{I_1}$  is a function of the temperature and it is formulated as [85]:

$$T = \frac{-E_{21}}{k \log\left(\frac{I_2 \nu_1 A_1}{I_1 \nu_2 A_2 \rho_{21}}\right)} \quad (3.13)$$

The line intensity ratio has been used to correlate the detected optical emission with the local concentration of the metal vapour in direct metal deposition processes [68]. It has also been used to correlate the intensity of absorption lines with the heat input in laser metal deposition [64]. In this study, intensity ratio profiles are plotted in order to investigate if there is a correlation with the processing conditions of the WAAM process.

### 3.4.2 Boltzmann Plot Method

Compared to intensity ratio, more accurate temperature calculations are made using the Boltzmann Plot method. In this technique, a larger number of emission peaks are considered to calculate the plasma temperature. By combining Equation 3.5 and Equation 3.9, the intensity of an emission line can be expressed as:

$$I = A_{21} h \nu_{21} N \frac{g_2}{g_1} \exp\left(\frac{-E_2}{kT}\right) \quad (3.14)$$

The terms in the above equation are simplified and rearranged. The relationship between the emission intensity of the  $i$ -th peak  $I_i$  at a wavelength  $\lambda_i$ , with a statistical weight  $g_i$ , Einstein's constant  $A_i$  and upper energy level  $E_i$  and the plasma temperature  $T$  is given by [85]:

$$\ln\left(\frac{I_i \lambda_i}{g_i A_i}\right) = -\frac{1}{kT} E_i + C \quad (3.15)$$

The temperature is calculated by first selecting 2-4 peaks from the emission spectrum - the accuracy of the calculation increases by considering a higher number of peaks. The noisy nature of the emission spectrum and the uneven superposition of discrete and continuum radiation across the wavelength range give rise to several criteria for the selection of emission lines to be diagnosed for temperature calculations[68]. These criteria are listed below:

- The selected emission lines are well resolved and free from the spectral interference from the same element or other elements.
- The selected emission lines have small continuum components.
- The intensity of the selected lines are not more than 80% of the spectrometer range to avoid processing saturated signals.

The wavelength and intensity of the emission lines are obtained from the detected spectrum and the other atomic constants are obtained from the NIST Atomic Spectra Database. For each selected peak, the term in the left hand side of Equation 3.14 is plotted against the right hand side. The slope of the linear regression line of the plotted data points is used to calculate the value of the average plasma temperature. An example of one such calculation is shown in Fig 3.3, and the atomic constants are taken from the NIST Atomic Spectra database and shown in Table 3.1.

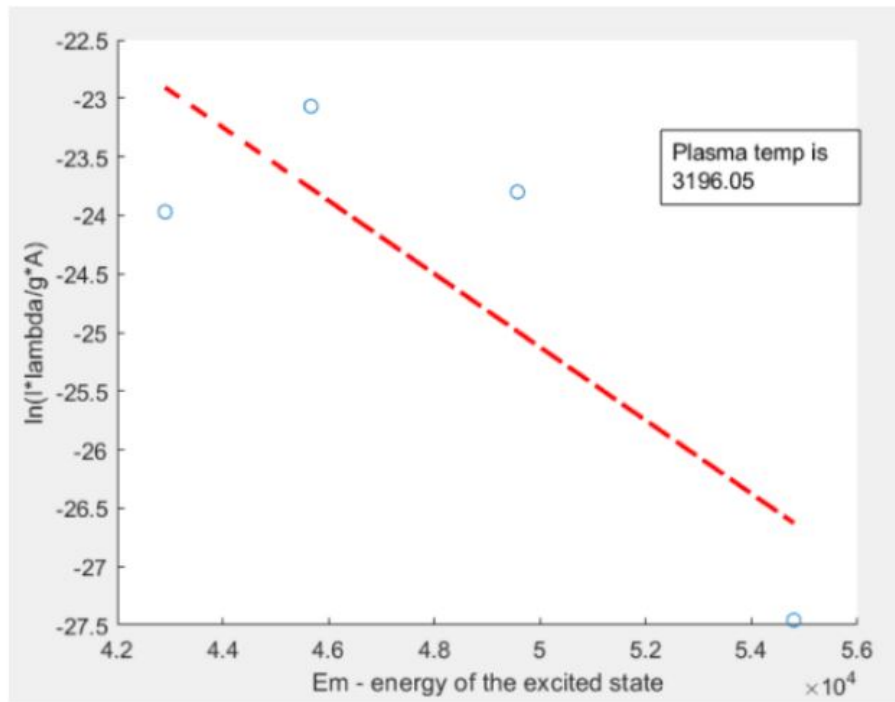


Figure 3.3: Example of plasma temperature calculation for 4 Chromium emission lines of wavelengths between 474-481 nm

Table 3.1: Chromium emission line data from NIST database for temperature calculation in Fig 3.3

Wavelength (nm)	$g^*A$ (sec <sup>-1</sup> )	$E_m$ (cm <sup>-1</sup> )
474.46	1.8e7	42908
475.619	8.1e8	54800
477.512	2.6e7	49572
481.42	1.7e7	45663

### 3.5 Conclusion

This chapter details the theoretical background behind the metal transfer processes that occur during GMAW-based WAAM deposition process. The metal transfer process creates a plasma arc between the wire and the base plate which emits radiation that is detected by the spectrometer. The principles of thermodynamic equilibrium and the laws of plasma physics are discussed in order to understand the techniques used to characterize the plasma radiation. Plasma diagnostic techniques like the intensity ratio and plasma temperature profiles are introduced in order to study their correlation with the processing conditions of the experiments. These profiles are calculated by detecting optical emissions from the plasma and processing the collected data. The next chapter details the experimental setup to collect optical emission data from the plasma arc and the post-processing algorithms used to visualize the plasma diagnostic techniques are also discussed in the chapter.



## Chapter 4

# Materials and Methods

### 4.1 Introduction

In this chapter, the basic setup of the WAAM cell and its various components are introduced. The material compositions of the wire feed, base plate and shielding gas are tabulated. The design of a self programmed application to study the collected OES data is presented. The application implemented post processing algorithms to identify and characterize the emission spectrum and calculate intensity ratio and plasma temperature profiles for different processing conditions. The spectrometer data collection parameters were optimised and the self programmed application was tested for three different processing conditions. The setup for all the experiments are detailed in this chapter.

### 4.2 Experiment Setup

WAAM experiments were performed using Super Active Wire Production mode (S-AWP, MAG welding with Inomaxx Plus shielding gas) with a Panasonic TM-1400WG3-AWP 6-axis welding robot and an additional welding table as shown in Fig 4.1 and Fig 4.2. Lincoln Electric LN316 LSi welding wire (diameter of 1.0 mm) was used in the experiments. An S355 steel plate with dimensions of 250 x 60 x 10 mm<sup>3</sup> was used as substrate. The chemical compositions of the wire, base plate and shielding gas are presented in Tables 4.1, 4.2 and 4.3 respectively. This material combination was chosen to be able to support the larger Aim2Excel project for future research.

A pivot arm was attached to the torch to hold one end of the Ocean Insight solarization resistant optic fibre with a core size of 600  $\mu\text{m}$ . This end was connected to a 74-DA Direct-attach Collimating Lens, which was pointed at the plasma arc to collect optical emissions with a pilot laser to ensure the alignment. The other end of the optic fibre was connected to an OceanOptics HR4000 spectrometer, which was further connected to a personal computer via a USB cable. The positioning of the spectrometer and its data collection parameters were optimized as part of this study in order to obtain reliable and repeatable data. The OceanView software was used to trigger the spectrometer and set data collection parameters. The collected spectrum data was processed with an app that was self-programmed in the MATLAB R2019b App Designer Toolbox. The app was developed and used to implement the post processing algorithm characterizing optical emissions and serve as a visualization tool for the collected data. The collected data was used to perform off-line plasma characteristics,

e.g. the plasma temperature was calculated and the spectral intensity ratio between different species were analysed.

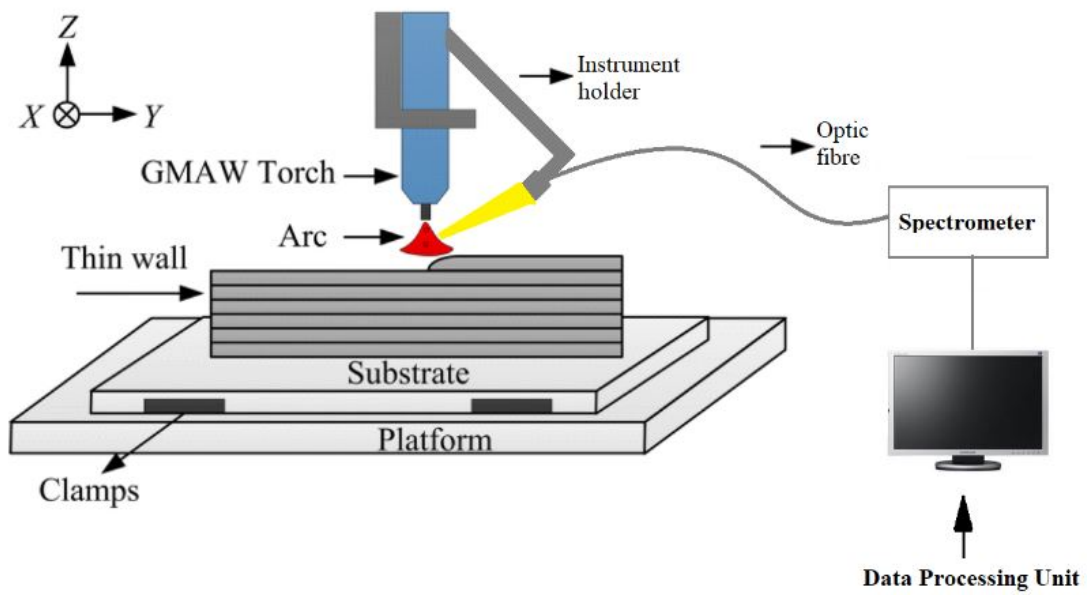


Figure 4.1: Schematic diagram of WAAM Setup



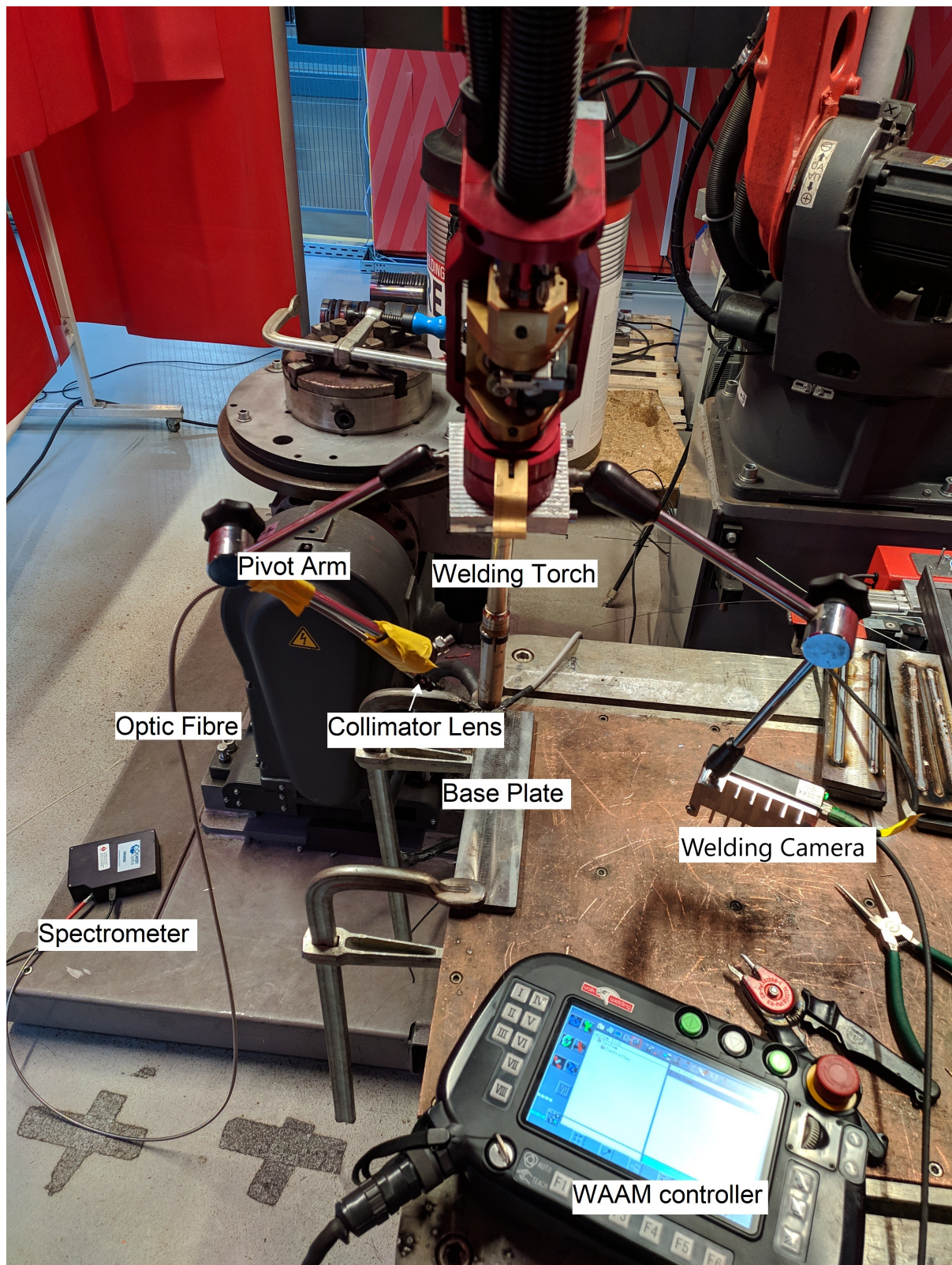


Figure 4.2: WAAM Experimental Setup

### 4.3 Materials Used

The chemical composition of all the materials used in the experiments of this study are detailed in the tables below.

Table 4.1: Composition of LN316 LSi welding wire

Element	Fe	Cr	Ni	Mo	Mn	C
Composition wt %	65.48	18.7	11.8	2.3	1.7	0.02

Table 4.2: Composition of S355 steel plate

Element	Fe	Mn	Si	Cu	C	P
Composition wt %	97.075	1.6	0.55	0.55	0.2	0.025

Table 4.3: Composition of Inomaxx Plus shielding gas

Element	Fe	Mn	Si	Cu	C	P
Composition volume %	97.075	1.6	0.55	0.55	0.2	0.025

Table 4.4: Composition of NiCrMoFe wire

Element	Ni	Cr	Mo	Fe
Composition wt %	59	23	16	2

Table 4.5: Composition of Ferromax Plus shielding gas

Element	He	CO2	Ar
Composition volume %	20	12	68

Table 4.6: Composition of X90 steel wire

Element	Fe	Cr	Ni	Mn	Mo
Composition wt %	73.2	23	2	1.5	0.3

Table 4.7: Composition of Abicor Binzel ceramic spray

Material	Acetone	Propane	Butane	Butanone
Composition wt %	30	30	30	10

### 4.4 Self-programmed Software for OES data analysis

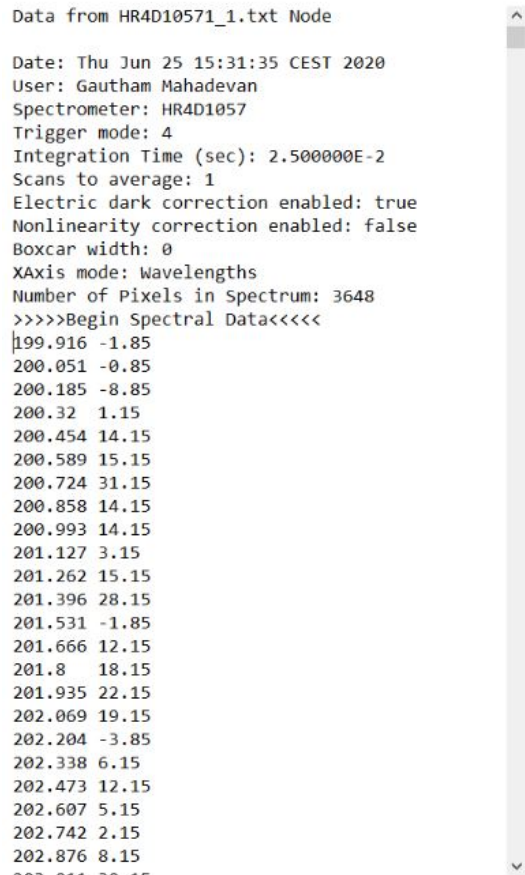
The detected optical spectrum was collected through the OceanView software and the data was stored as text files. The data was fed into post-processing algorithms to i) detect back-



ground radiation, ii) identify and characterize the discrete emission lines (peaks) in the broadband emission spectrum, iii) process the intensity profiles for plasma temperature computation, iv) and intensity ratio calculations. The developed app GUI was also used to plot data from the high-frequency V-I measurements. To implement these algorithms and visualize the results, a digital application was designed in the MATLAB App Designer environment. The working of these algorithms and the graphical user interface (GUI) of the app is further elaborated in the following sections.

#### 4.4.1 Spectral Data Collection

Each data file generated by the spectrometer has two columns - wavelength and intensity. The wavelength range is from 200-650 nm, with a resolution of 0.135 nm. The detected intensity falls in the range of 0-16000 intensity units. The trigger settings of the spectrometer determines the frequency of data collection. The input data files are named sequentially such that they can be easily indexed and queried by the app. Each file also contains metadata encoding the spectrometer collection settings. An example of a data file generated by the spectrometer is shown in Fig 4.3.



```
Data from HR4D10571_1.txt Node

Date: Thu Jun 25 15:31:35 CEST 2020
User: Gautham Mahadevan
Spectrometer: HR4D1057
Trigger mode: 4
Integration Time (sec): 2.500000E-2
Scans to average: 1
Electric dark correction enabled: true
Nonlinearity correction enabled: false
Boxcar width: 0
XAxis mode: Wavelengths
Number of Pixels in Spectrum: 3648
>>>>Begin Spectral Data<<<<
199.916 -1.85
200.051 -0.85
200.185 -8.85
200.32 1.15
200.454 14.15
200.589 15.15
200.724 31.15
200.858 14.15
200.993 14.15
201.127 3.15
201.262 15.15
201.396 28.15
201.531 -1.85
201.666 12.15
201.8 18.15
201.935 22.15
202.069 19.15
202.204 -3.85
202.338 6.15
202.473 12.15
202.607 5.15
202.742 2.15
202.876 8.15
203.011 10.15
```

Figure 4.3: Sample data file generated by the spectrometer

### 4.4.2 NIST database

The National Institute of Standards and Technology (NIST) maintains an open source database of all atomic spectra lines [86]. The elements that constitute the wire, base plate and shielding gas are queried into this online database as shown in Fig 4.4 and the wavelength, energy of electronic transition  $E_m$ , statistical weight  $g_1$  and Einstein's coefficient  $A_1$  values are obtained for all wavelengths. Data from this table is scraped and stored offline for every constituent element. This data is then indexed and queried by the app while performing peak identification and temperature/intensity ratio calculations.

Figure 4.4: NIST Atomic Spectra database [86]

### 4.4.3 Baseline Estimation

As explained in Section 3.4, the detected optical emission is a superposition of radiation from multiple sources. The presence of continuum background radiation in the detected signal is undesirable because it can contribute to the saturation of the signal. This algorithm estimates the baseline contribution due to continuum radiation. The baseline estimation is an implementation of an algorithm developed for Raman spectroscopy [87]. This implementation uses a small window moving average smoothing filter to extract the baseline from the signal passed as the input. The mathematical basis for this algorithm is as follows: The measured data  $\mathbf{m}$  can be represented as  $\mathbf{m} = (\mathbf{b}+\mathbf{x})*\mathbf{p} + \mathbf{n} = \mathbf{b}*\mathbf{p} + \mathbf{x}*\mathbf{p} + \mathbf{n}$ , where the pure or

underlying signal vector  $\mathbf{x}$  plus the baseline  $\mathbf{b}$  is convolved (\*) with the instrument blurring function  $\mathbf{p}$  and measurement noise  $\mathbf{n}$  is added. The purpose of baseline estimation is to produce an estimate for  $\mathbf{b}*\mathbf{p}$  from  $\mathbf{m}$ . This is done in the following way:

- The first iteration uses a zero-order Savitzky-Golay filter to estimate the baseline [88],
- Signals above the estimated baseline are stripped and the estimation is repeated, with an increase in the effective filter window on further iteration,
- A large window narrows the frequency pass band and increases signal rejection, allowing more signal to be processed,
- This is repeated through many iterations until a certain stopping criterion is reached. In this case, it is when the area between the 3rd order polyfit and the first derivative of the residual baseline is greater than 15% of the area below the first derivative after a certain number of iterations.

The baseline estimation algorithm is summarized in the flowchart shown below in Fig 4.5

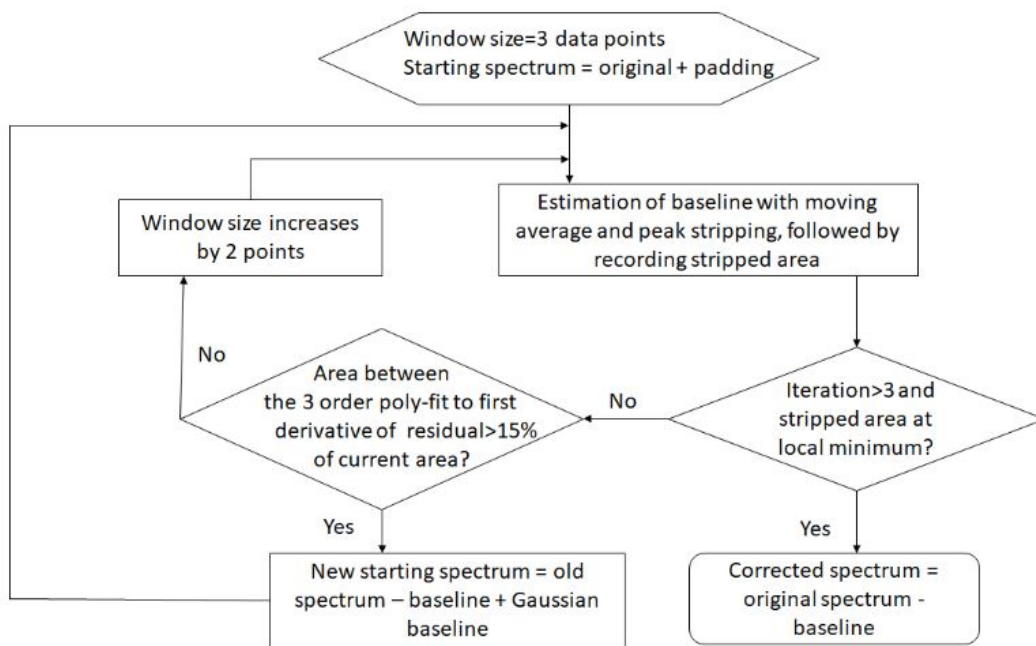


Figure 4.5: Flowchart for baseline estimation algorithm

#### 4.4.4 Peak Characterization

The discrete emission lines from the detected spectrum act as a ‘fingerprint’ of the chemical species present in the system. The wavelengths of the emission peaks are unique to the individual species present based on the energy released during electronic transitions between energy states. These peaks were identified using a differential smoothing algorithm and the

wavelength of these peaks were matched to the NIST database to identify the species. These algorithms are further elaborated below, and summarized in Fig 4.6. The GUI of the software application implementing this algorithm is shown in Fig 4.7.

#### 4.4.4.1 Finding Peaks

The peak-searching function was written to count the positive peaks in a noisy dataset like the emission spectrum, with the wavelength and intensity data as the input. The function smoothens the noise by passing the derivative function of the input data through a moving average filter. Downward zero crossings of the filtered output were detected as peaks if they exceed a certain amplitude threshold. The function outputs a list containing the wavelength and intensity of all the detected peaks.

#### 4.4.4.2 Matching Peaks

The peak-matching function was written to match the detected peaks with data from the NIST database. The wavelength and intensity are input into the function. The peak is matched to a chemical species if the difference between the wavelengths of the detected peaks and wavelengths from the NIST database of that species is less than a certain wavelength threshold. This threshold is calculated as half the resolution of the spectrometer. This process is repeated for all the constituent elements in the printing environment.

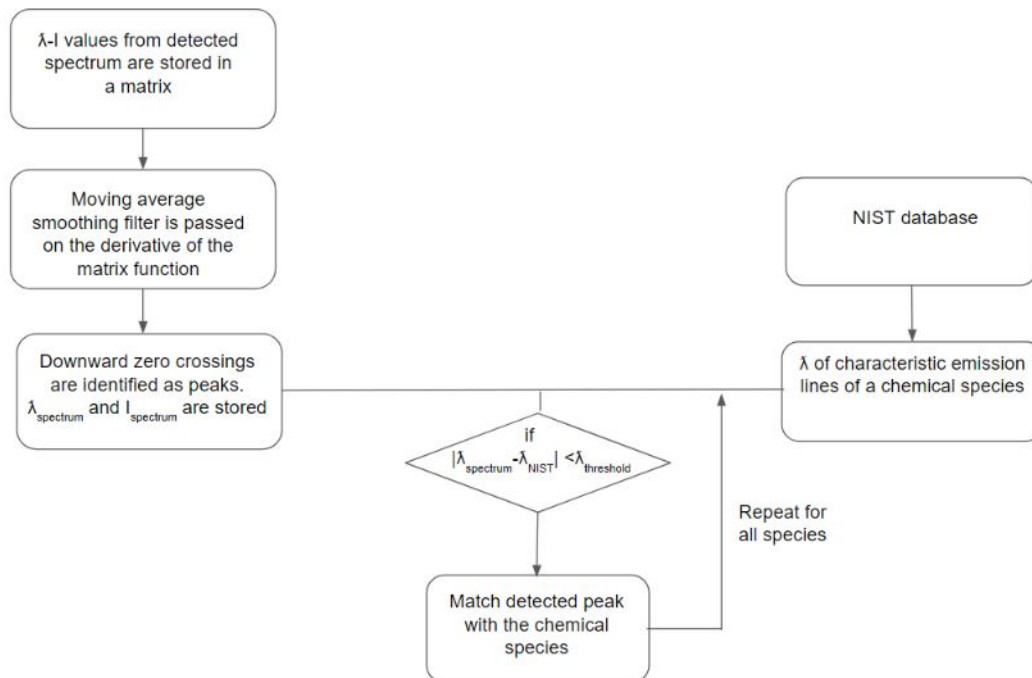


Figure 4.6: Flowchart for Peak Matching algorithm

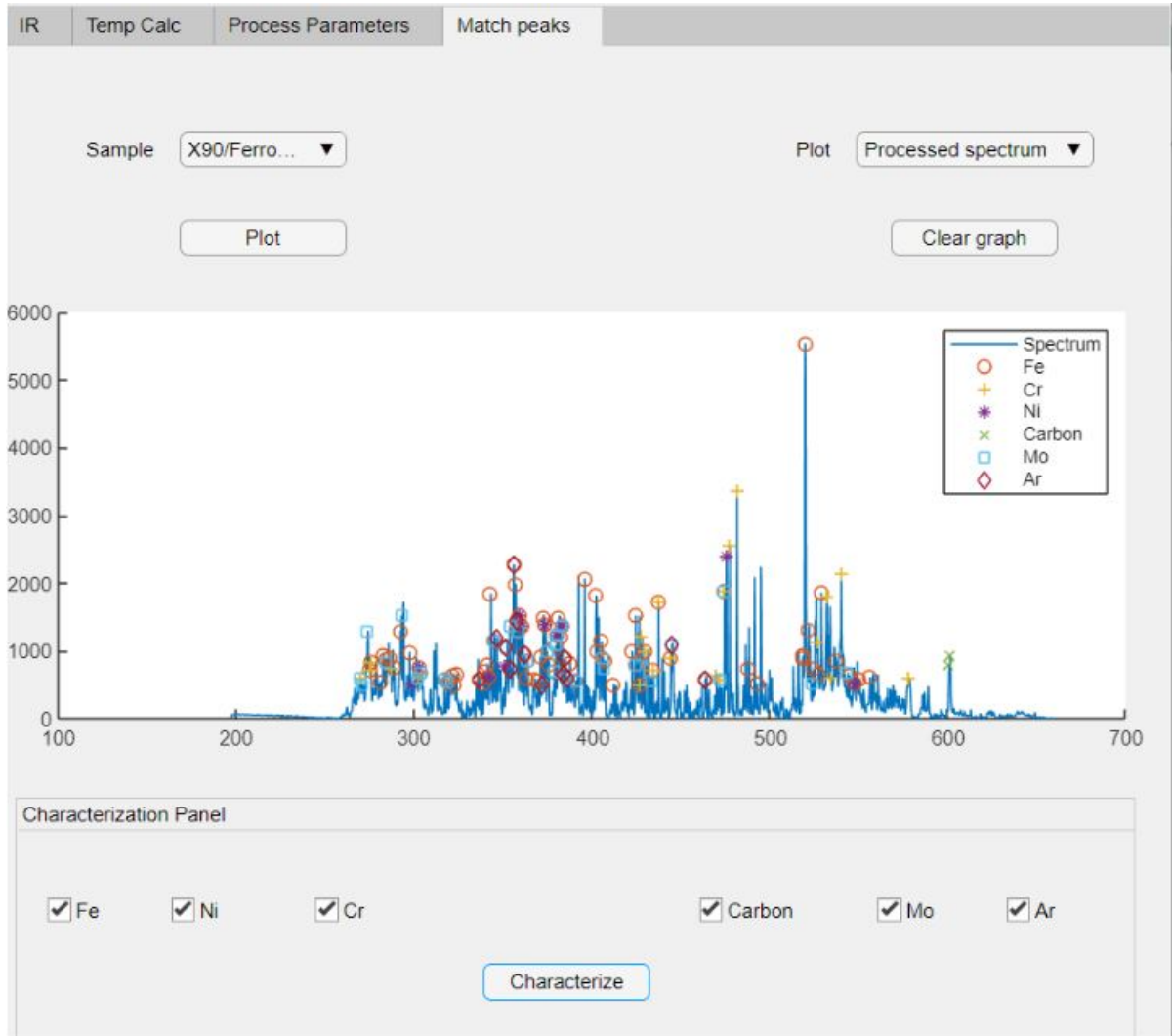


Figure 4.7: Software Application GUI of peak characterization

#### 4.4.5 Intensity Ratio and Temperature calculations

The spectrometer was triggered at the start of the metal deposition. Data files were generated and stored in the target folder at a set frequency determined by the integration time of the spectrometer, further discussed in Section 4.5.1.3. The  $\lambda$ -I data of all the files in one deposition are stored in a table structure. Intensity values at wavelengths corresponding to emission peaks are then queried by the app and used for intensity ratio and temperature calculations.

##### 4.4.5.1 Intensity Ratio

One of the theoretical goals of the study was to investigate the correlation between the intensity ratio and processing conditions like current, voltage and surface anomalies on the base plate. To this end, a GUI was designed to visualize intensity ratio as a function of distance. The backend of the software implemented the peak matching algorithms detailed

in Section 4.4.4. From that list of detected peaks, specific emission lines are chosen for study based on the criteria detailed in 3.4.2. For each selected input data set, the species and wavelength of the matched peaks are taken as the input and the program outputs a plot with the intensity ratio on the y-axis and the distance from the ignition of the first arc in millimeters on the x-axis. The app GUI also enabled the comparison of IR profiles of two different datasets. This program also enables the study of emission peaks from any of the species present in the processing environment. The GUI of this program is shown in Fig 4.8

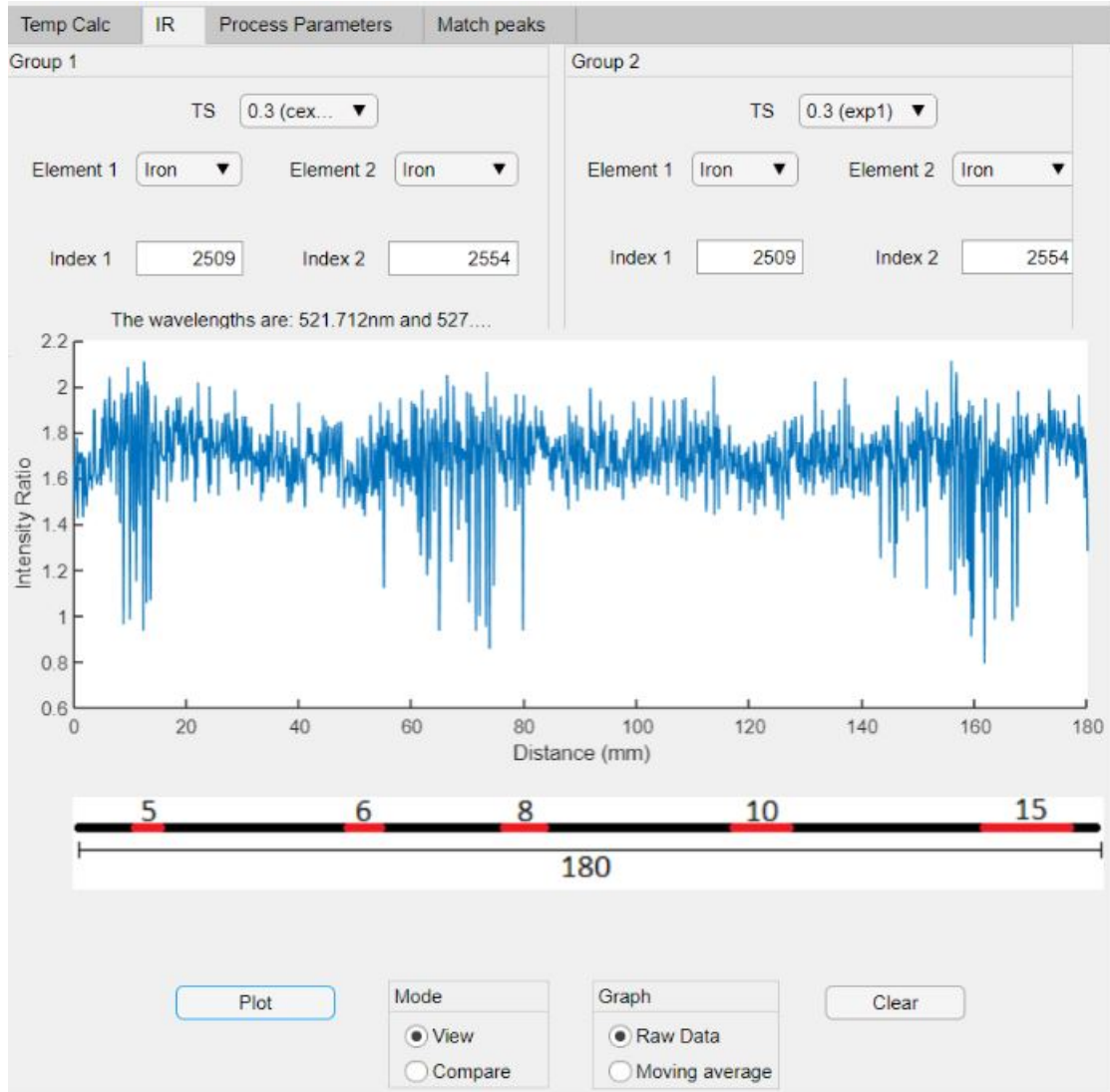


Figure 4.8: App GUI to visualize Intensity Ratio profiles

#### 4.4.5.2 Implementation of Boltzmann Plot

$$\ln \left( \frac{I_i \lambda_i}{g_i A_i} \right) = -\frac{1}{kT} E_i + C$$

The input data is passed through the peak characterization algorithm detailed in Section 4.4.4 to obtain the wavelength and intensity of the detected emission peaks. Emission lines



are chosen for temperature calculation according to the criteria presented in Section 3.4.2. These values are plugged in Equation 3.15 as  $I_i$  and  $\lambda_i$  respectively. The MATLAB program takes the atomic species and wavelength of the selected peaks as the input. The backend of the program matches the wavelengths with the NIST database to obtain the values of the transitional probability  $A_i$ , statistical weight  $g_i$ , and the energy of the upper excited level is  $E_k$  for each of the selected emission lines. The term on the left hand side of the above equation is plotted as a function of  $E_i$  for all the selected emission lines. The temperature can be calculated from the negative inverse of the slope of the linear regression line of the plotted data points. The app plots the calculated plasma temperature as a function of distance. The app GUI also allows for the comparison of two different temperature profiles. This feature was used to study the difference in temperature profiles of different datasets.

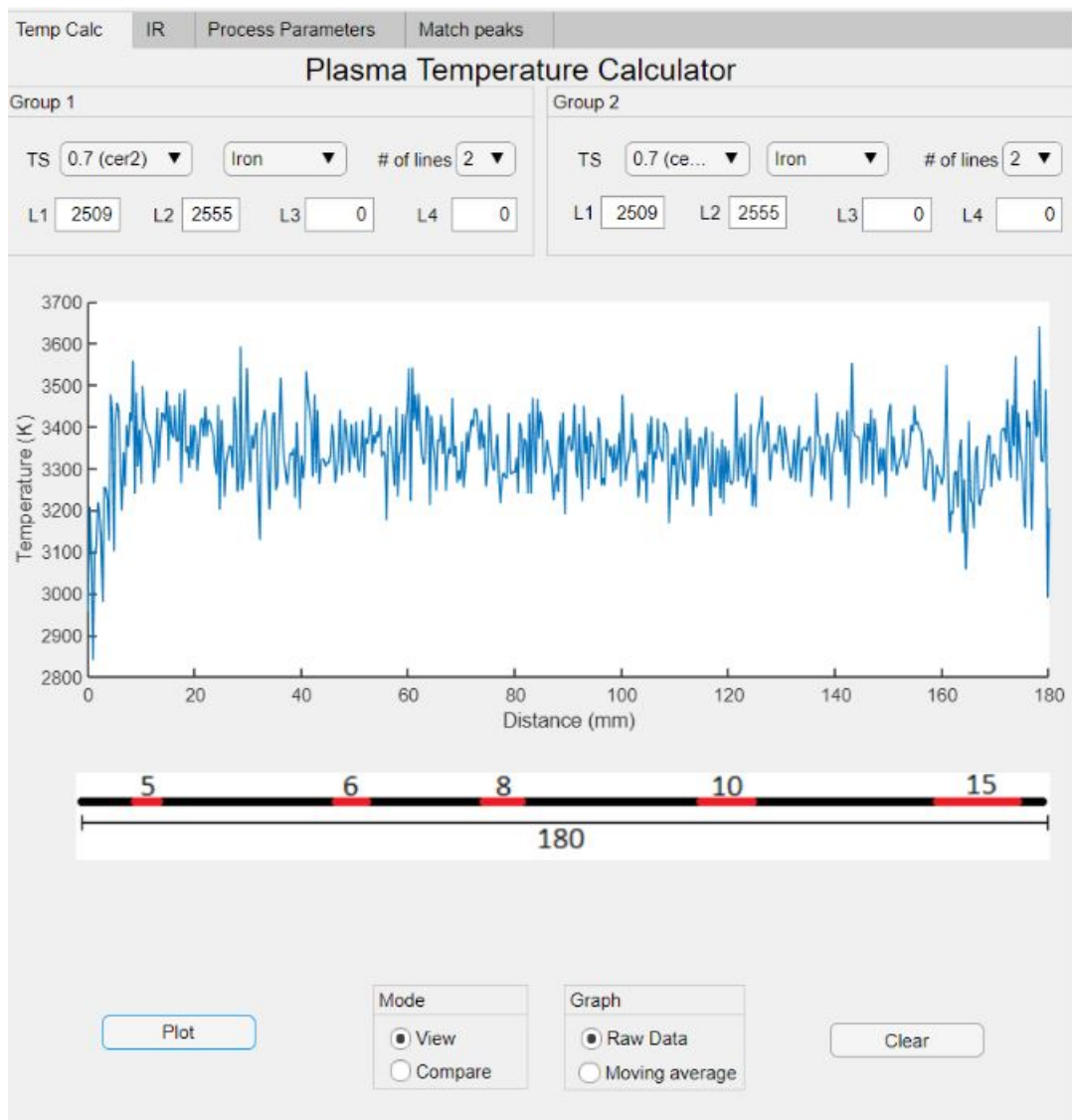


Figure 4.9: App GUI to visualize Plasma Temperature profiles

#### 4.4.6 Process Parameters Visualization

The app GUI also enables the visualization of the high frequency current and voltage data that was collected from the anomaly detection test experiment via a Hall effect sensor. The application of this high frequency data is further elaborated in Section 5.6.2.1. The program takes the dataset and the x-axis limits as the input and outputs two plots with current (A) and voltage (V) on the y-axis as a function of distance, as shown in Fig 4.10. The app also enables the comparison of data from two different datasets in order to characterize differences in processing conditions.

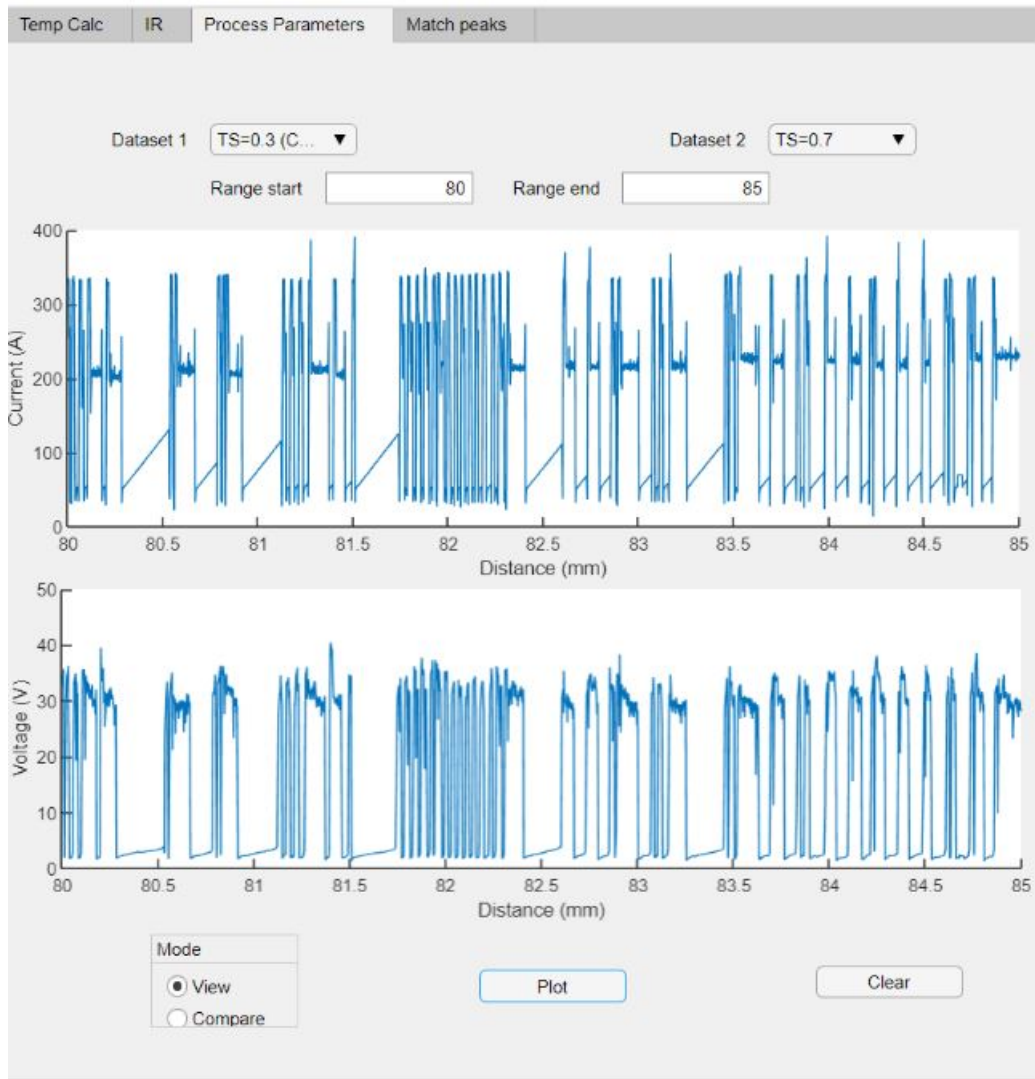


Figure 4.10: App GUI to visualize high frequency V-I data

### 4.5 Experiment Design

The post processing algorithms were used to implement the equations of plasma physics on the detected optical emission spectrum and study its correlation with the processing con-

ditions. The research objective of this study was to design a reliable experimental setup, software tools and validate its reliability by correlating spectral data with the processing conditions. The first set of experiments determined the optimum data collection conditions of the spectrometer. This was followed by testing the repeatability of optical spectrum characteristics for a certain processing condition. The reliability of the experimental setup and software tools were tested for three different processing conditions - a peak characterization test with different material combinations, a ramping test where the energy input into the WAAM system was incrementally increased, and an anomaly detection test where the presence of an artificially deposited impurity on the base plate was characterized using OES. Potential correlations between the collected spectrum with process stability and bead characteristics are studied. The results of the anomaly detection test are also validated by optical microscopy, high frequency V-I data and high-speed video footage.

### 4.5.1 Spectrometer Optimization

As the main monitoring instrument in this study, it was important to ensure that the data collected by the spectrometer was accurate and reliable. The reliability of the collected data was ensured by:

- Robust positioning: Ensuring that the optic fibre always points at the wire tip where it covers the plasma arc and the melt pool,
- Preventing signal saturation: Use of a lens filter and experimentally verifying the optimum angle of observation,
- Ensuring repeatability: The processed emission signals show minimum variation when the processing conditions are the same.

#### 4.5.1.1 Positioning

Data is collected using the spectrometer via an optic fibre cable. One end of the fibre is connected to the spectrometer, and the other end is taped to a pivot arm firmly to maintain the steadiness. The pivot arm is securely screwed to the side of the welding torch as seen in Fig 4.11 to avoid any possible shift.



Figure 4.11: Spectrometer Positioning Setup

To ensure that the collimator is always pointed at the wire tip, a red ‘pilot laser’ is used. The spectrometer end of the fibre is disconnected and light from the laser is passed through this end. This light passes through the optic fibre and forms a spot where it is focused. The arm is adjusted such that the spot is focused just below the wire tip. This is done to ensure that the optical emission is always collected from the plasma arc that forms between the wire tip and base plate. The fibre was connected back to the spectrometer after the position was fixed.

Another function of the pilot laser was to calculate the angle of observation between the optic fibre and the plasma arc. A measuring scale was placed perpendicular to the laser spot between the torch and welding table, such that the projection on the scale was a circle as shown in Fig 4.12. Subsequently, the scale was placed on the table such that the projection of the laser spot is an ellipse. The diameter of the circle and major axis length of the ellipse were noted. The angle of observation is calculated using trigonometry, as shown in

the 2-dimensional schematic diagram in Fig 4.13. The diameter of the circle is equal to AB and the diameter (major axis) of the ellipse is given by BC. The angle  $\theta$  is calculated as  $\sin^{-1}(AB/BC)$ . For the example shown in 4.12, the angle calculated using the method described above is  $56.4^\circ$ .

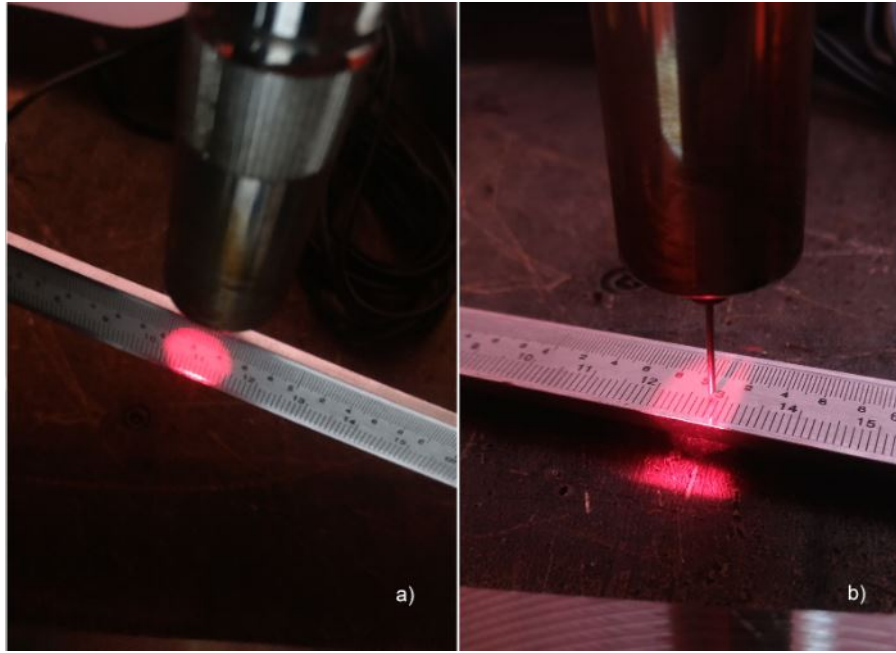


Figure 4.12: Angle calculation using pilot laser

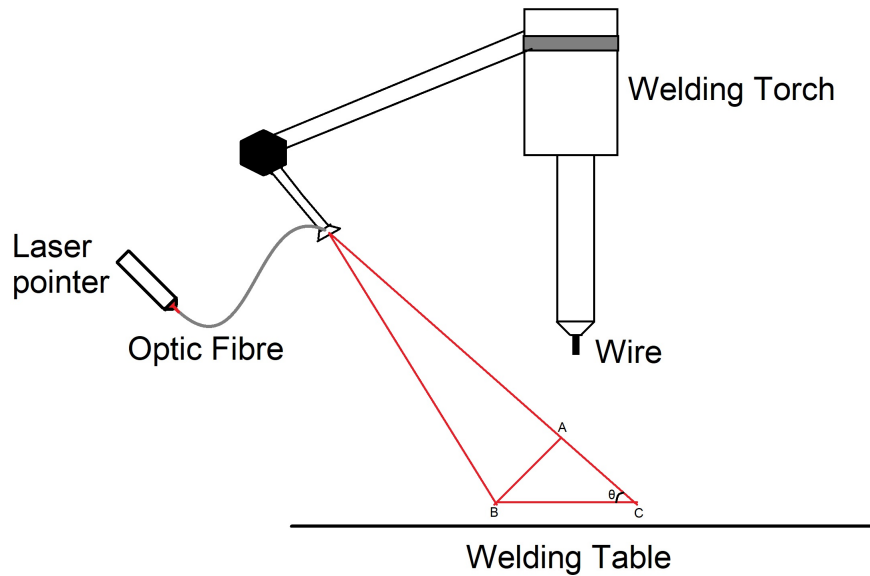


Figure 4.13: Two dimensional schematic representation of angle calculation using pilot laser

#### 4.5.1.2 Signal Saturation

Signal saturation occurs when the intensity of the optical emission exceeds the detection range of the spectrometer. This is undesirable as the temperature and intensity ratio profiles cannot be calculated if the intensity of the emission peaks exceeds the spectrometer range of 16000 intensity units. The following techniques were used to avoid the saturation of the signal:

- Optimize spectrometer settings: The trigger settings of the spectrometer determine the intensity of the collected spectrum,
- Minimize signal contribution from continuum radiation: The use of a optic filter and optimizing the angle of observation reduces the background radiation.

#### 4.5.1.3 Integration Time

A charged-couple device (CCD) spectrometer was used in this study. The integration time of the spectrometer was adjusted to optimize data collection. The integration time determines the CCD readout frequency and therefore the exposure time of the detector. The longer the integration time, the more light is exposed to the detector during a single scan, and higher the intensity of the signal. If the integration time is too low, the signal to noise ratio decreases, resulting in an attenuated signal and false positives in the peak matching algorithm. The HR4000 spectrometer used in this study has an integration time range from 5-200 ms. The optimum integration time was obtained by trial and error, and was determined to be 25 ms for all the experiments done in this study.

#### 4.5.1.4 Optic Filter

The light emitted by the plasma arc was observed to saturate the detected spectrum at different wavelength ranges, as shown in Fig 4.14a for example. To prevent the saturation of the signal, a polymer tape was used to cover the entrance of the collimating lens and act as a physical filter. The filter only has an effect on the relative intensity of detected radiation. OES characterization techniques use relative intensity values and therefore are not affected by the filter. The effect of the filter is illustrated in Fig 4.14 comparing the detected spectrum for the same processing conditions with and without the filter.

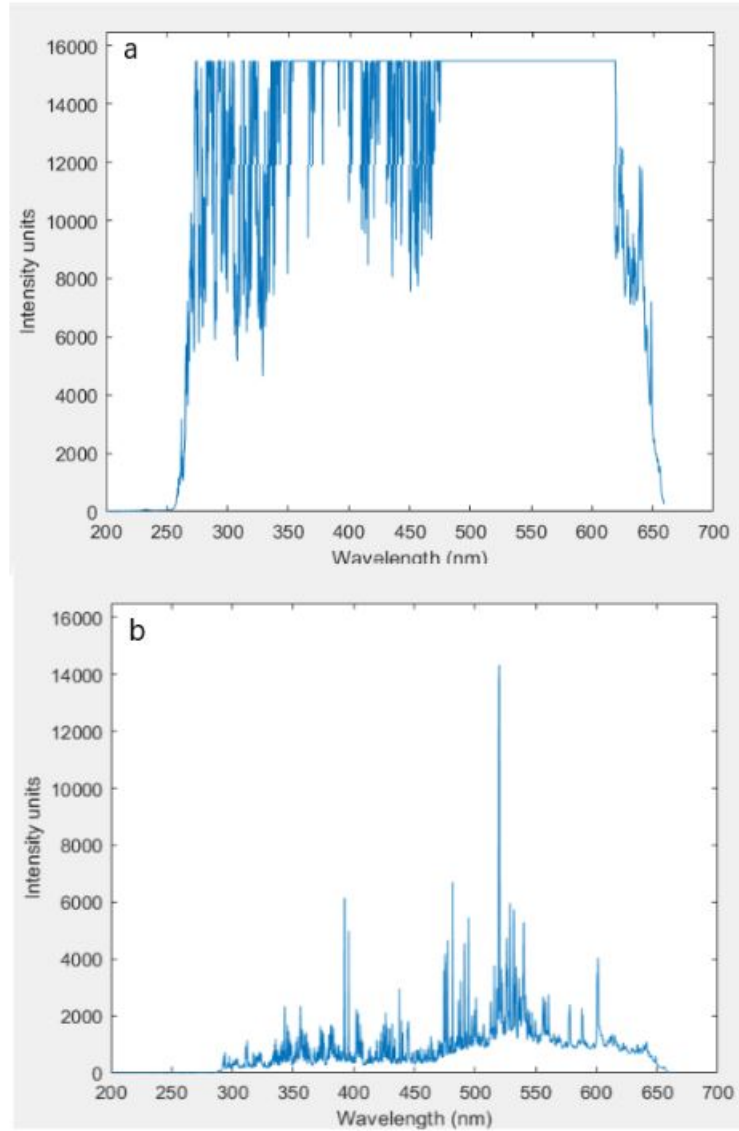


Figure 4.14: a) OES spectrum without filter b) OES spectrum with filter

#### 4.5.1.5 Angle Optimization

As discussed in Section 3.4, the detected optical emission is a superposition of radiation from multiple sources. The plasma emits discrete line radiation that is seen as peaks in the emission spectrum. The liquid melt pool and the metal vapour emit black body continuum radiation characterized by Planck's equation. The presence of continuum background radiation in the signal can lead to signal saturation when superimposed with the discrete radiation. This background radiation is however not the same in all directions - the metal vapour and melt



pool are not symmetrical but have a complex shape determined by the forces acting on it. The superimposed contribution of emission peaks from the plasma arc, metal vapour and melt pool is asymmetric and depends on the angle of observation.

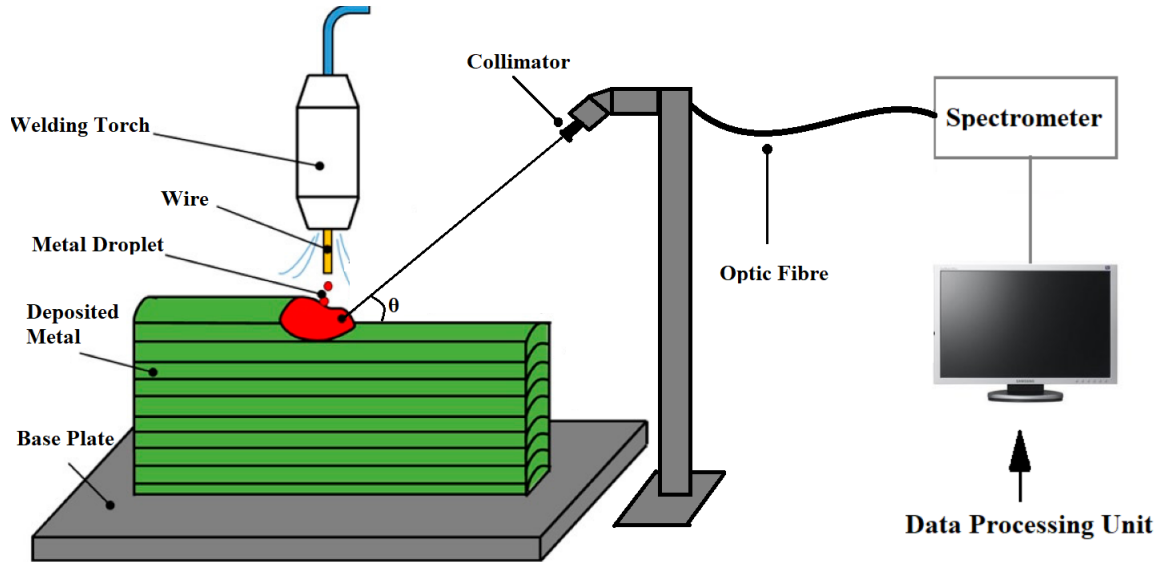


Figure 4.15: Experimental setup for angle test

The aim of this experiment was to determine the optimum angle of observation. The experiment setup consisted of the WAAM robotic arm described in Section 4.2. The 316L wire was deposited on an S355 steel base plate at a speed of 0.7 m/min. An adjustable stand was used to fix the collimator and optic fibre, which was connected to the spectrometer. Five identical weld beads were printed, where the observation angle  $\theta$  was increased incrementally by  $10^\circ$  from  $20^\circ$  to  $60^\circ$ . Angles beyond  $60^\circ$  could not be measured as the welding torch blocked the light path. The detected optical emission was then passed as the input for the baseline estimation algorithm in order to determine the background continuum component of the signal. From this experiment, the optimum angle of observation was determined for future experiments, and discussed in Section 5.1.

#### 4.5.1.6 Signal Repeatability

The reliability of a monitoring system is tested by performing repeated experiments with the same processing conditions and comparing the OES observations to characterize differences. If the detected signals are observed to have the same characteristics with only minor differences, the repeatability of the system is validated. To illustrate this, identical weld beads of 180 mm in length were printed on the base plate with a weld current of 160 A and voltage of 18 V and travel speed of 0.7 m/min using the experimental setup described in Section 4.2. To evaluate the repeatability of the signal, an Fe I emission line at a wavelength of 444.8 nm was selected. The intensity of the radiation at this wavelength is plotted for all the collected data in a single weld bead. The plasma temperature profiles were also plotted for each bead choosing three Cr I emission lines at 526.54 nm, 528.76 nm and 531.84 nm. Intensity ratio profiles were calculated for both sets of welds by studying the Fe I emission lines at 491.21 nm and 494.93 nm. This process is repeated for the same conditions, but with a travel speed of 0.3 m/min. The same profiles are calculated for a pair of beads with a travel speed of



0.3 m/min, but the observation angle of the spectrometer was changed in order to illustrate the difference in the detected signals for the same processing conditions when the observation angle is disturbed. The processed OES signal for all depositions are presented and discussed in Section 5.3.

### 4.5.2 Setup and Software Validation

The previous sections described how to collect reliable data relying on the proper setup, the algorithms used to process and visualize the emission spectrum. One of the research objectives of the study was to validate the experimental setup and self programmed software through correlating emission data from the plasma arc for different processing conditions. To this end, three experiments were designed and the collected spectrums were processed by the software in order to study the processed optical spectrum. The first experiment tested the peak matching software using different combinations of materials for the wire and shielding gas. The second experiment was a ramping test where input current and voltage were incrementally increased. The last experiment was an anomaly detection test, where OES was used to characterize the presence of an artificially deposited anomaly on the base plate. The results of the anomaly detection test were additionally validated by optical microscopy, high frequency V-I data and footage from a Phantom high-speed camera at 4100 FPS.

#### 4.5.2.1 Peak Characterization Test

The goal of this experiment was to test the functionality of the peak matching algorithm with different combinations of wire feed material and shielding gas. The peak characterization algorithm is also used in plasma temperature and intensity ratio calculations. By testing the software on different material combinations, it is shown that the OES characterization techniques developed in this study can be used for any WAAM system. In this experiment, three different material combinations were used for the wire feed and shielding gas. The first wire/gas material combination was 316L wire with Inomaxx Plus shielding gas, with the compositions described in Tables 4.1 and 4.3 respectively. The second material combination was an NiCrMo alloy (Alloy 59) with Ferromax Plus as the shielding gas, with the compositions described in Tables 4.4 and 4.5 respectively. The last material combination was X90 steel wire with pure argon shielding gas, with the composition of the wire described in Table 4.6. The experimental setup described in Section 4.2 is used and the collected OES data is fed into the software. The characterized emission peaks for all material combinations are shown in Section 5.4

#### 4.5.2.2 Ramping Test

The goal of this experiment was to study the correlation between the detected OES signal and WAAM process parameters like current and voltage. This was done by varying the input parameters to observe differences in the detected signal. These variable conditions are designed in the form of a ramping test, where the current and voltage was incrementally increased in 5 steps. The increase in heat input is expected to supply more energy into the system and reflect in the intensity of the plasma arc that is created in the process.

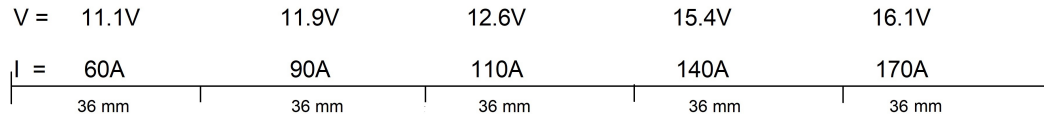


Figure 4.16: Schematic drawing of Ramping Test processing conditions along a deposition line of 5x36 mm

The experimental setup of the system is shown in Fig 4.2, and uses the WAAM setup described in Section 4.2. Three beads of 180 mm in length were deposited, with a travel speed of 0.3, 0.7 and 1.2 m/min respectively. The current and voltage was incrementally increased every 36 mm as shown schematically in Fig 4.16 and OES data was collected and processed for all the printed beads. The correlation between the detected OES spectrum and the ramping conditions were studied by visualising the processed OES signal in the app that was developed. The results of this experiment are presented and discussed in Section 5.5.

#### 4.5.2.3 Anomaly Detection Test

The goal of this experiment was to study the potential of detecting an artificially deposited ‘anomaly’ on the base plate using the OES based monitoring system. A common problem encountered during the printing of metal components is the presence of anomalous conditions in the printing environment. These anomalies are in the form of oxidized spatter from a nearby weld path, a base plate contaminated with oil or dirt, or improper shielding conditions. The presence of these anomalies can act as a barrier between the wire and the base plate, which can further affect the melt pool conditions and geometry of the weld bead [89]. In the printing of components, inhomogeneous weld bead geometry can result in undesirable defects like porosity and lack of fusion and increases the likelihood of early failure [90]. The purpose of this experiment was to detect the presence of intentionally introduced anomalies during the printing using OES technique.

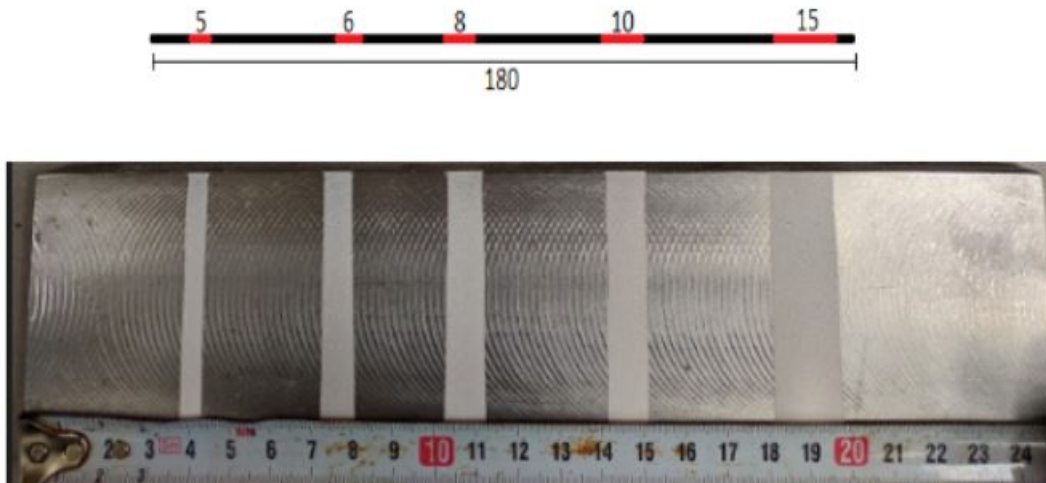


Figure 4.17: Ceramic pattern on S355 base plate for the Anomaly Detection Test

Two S355 steel base plates were used, with one plate coated with a ceramic pattern as shown in Fig 4.17. Abicor Binzel Ceramic spray was used to deposit a thin layer of ceramic on the

base plate, which had a chemical composition described in Table 4.7. This material simulates the presence of an impurity in the printing environment since it affects the metal transfer mechanism and shape of the weld pool. Two sets of identical welds were made on both base plates. Each set consisted of three beads of 180 mm in length that were deposited on the plate with a TS of 0.3 m/min, 0.7 m/min and 1.2 m/min, with a constant current of 160 A and voltage 18 V. The width of the ceramic pattern was increased incrementally as shown in Fig 4.17 in order to study possible correlations between the emission spectrum and the size of the simulated impurity. The results of this experiment are presented and discussed in Section 5.6.

#### **4.5.2.4 Validation of Anomaly Detection Test**

In the experiments described above, OES was used to characterize the presence of anomalies on the printing surface. In this part of the study, independent analysis techniques were used to validate the results obtained from OES. These techniques studied the effect of the anomaly on the weld geometry and metal transfer process. These studies were done to further understand the plasma processes that are characterized by OES observations. A Hall effect based high frequency sensor was used to measure the current and voltage passing through the workpiece at a frequency of 25 kHz. The recorded data shows the difference in V-I waveforms between the two sets of experiments done in the anomaly detection test. A Phantom high-speed camera was used to shoot videos of the WAAM process at a frame rate of 4100 FPS to better understand the metal transfer process behaviour of the plasma arc, and correlate the data obtained from OES and the high frequency V-I measurements. To understand the differences in the weld bead geometry, cross-sections of the base plate with the printed welds were made and Optical Microscopy was used to study the geometry and shape of the printed bead.



## Chapter 5

# Results and Discussion

The collected OES data was processed via a self-programmed application that was described in Section 4.4. The spectrometer optimization followed by three experiments with different processing conditions - a peak characterization test, ramping test, and the anomaly detection test. The OES data from these experiments were processed and the results are presented in this chapter. From the obtained results, the correlation between the detected signals and the experimental processing conditions are also discussed in detail.

### 5.1 Spectrometer Optimization: Angle Test

#### 5.1.1 Results

In this experiment, OES data was collected at 5 different observation angles  $\theta$  shown in Fig 4.15 from  $20^\circ$  to  $60^\circ$  for the processing conditions described in Section 4.5.1.5. The collected data was passed through the baseline estimation algorithm in order to deconvolute the signal and extract the baseline contribution from continuum radiation. The estimated baseline of the signals from all the measurement angles is shown in Fig 5.1. Fig 5.2 shows an example of the calculated baseline for an observation angle of  $20^\circ$

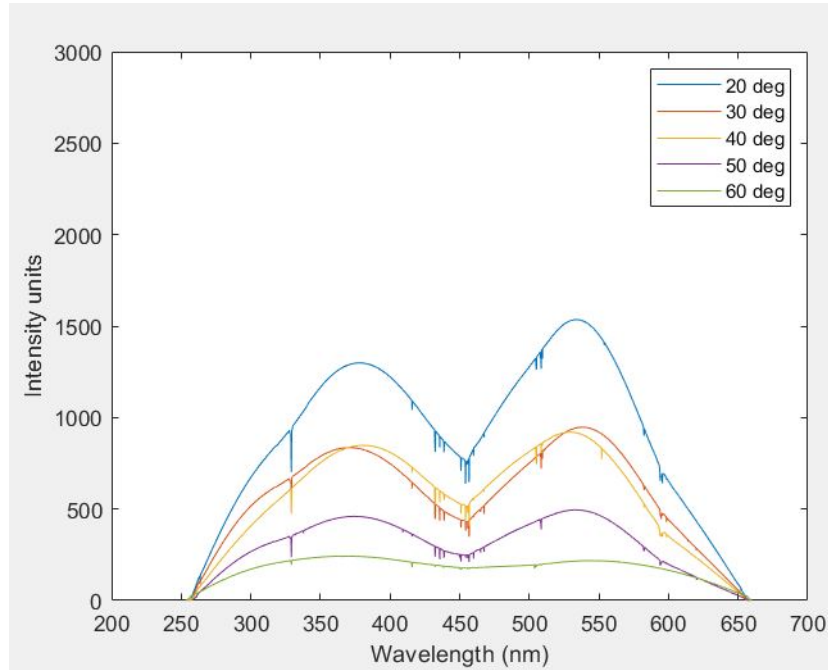


Figure 5.1: Angle Test baseline profiles

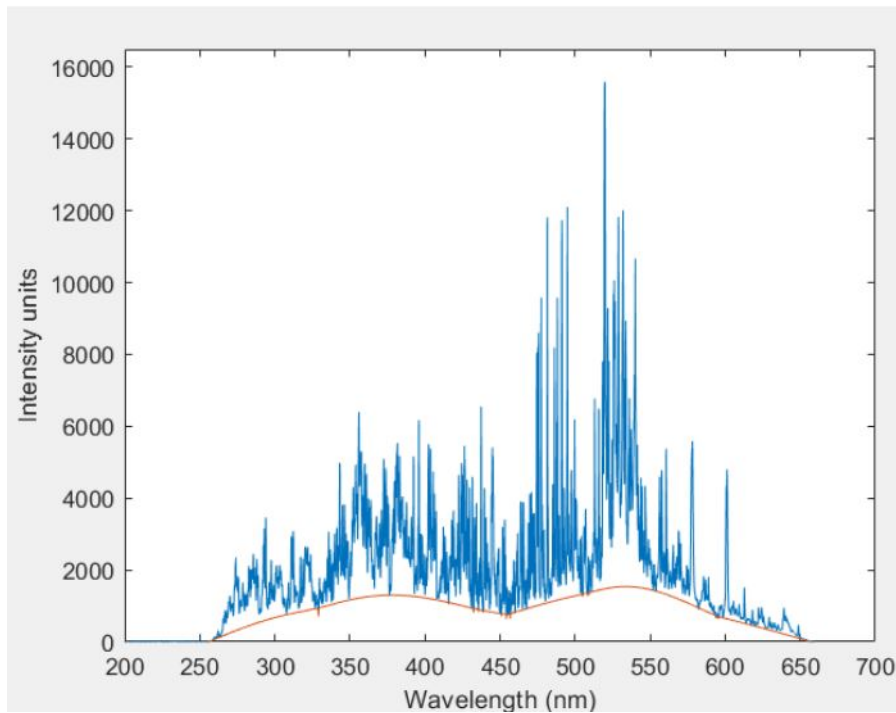


Figure 5.2: Sample baseline calculation for an observation angle of 20°

From the plot in Fig 5.1, it can be seen that the baseline plots have a correlation with the angle of observation. At the lowest angle of observation, the calculated baseline has the highest intensity. As the angle of observation was increased, the intensity of the baseline reduces at all wavelengths in the detection range. It is also seen that all plots have roughly

the same profile. There are two peaks between 350-400 nm and 500-550 nm and a valley between 400-500 nm. The peaks and valleys are sharper at lower angles of observation. As the observation angle is increased, the profiles become more rounded. Another observation is the presence of downward discontinuities on the calculated baseline found in wavelength ranges of 300-350 nm, 400-450 nm and 500-550 nm. These discontinuities were observed for all of the calculated profiles at the same wavelengths.

### 5.1.2 Discussion

The calculated baseline profile is a superposition of continuum radiation from the melt pool and metal vapour. From Fig 5.1, it can be inferred that the continuum radiation is not the same in all directions and therefore depends on the angle of observation. The plotted profiles indicate that the metal vapour from the weld dissipates more towards the sides than upwards in the direction of the torch. This results in a higher observed background radiation at lower angles of observation.

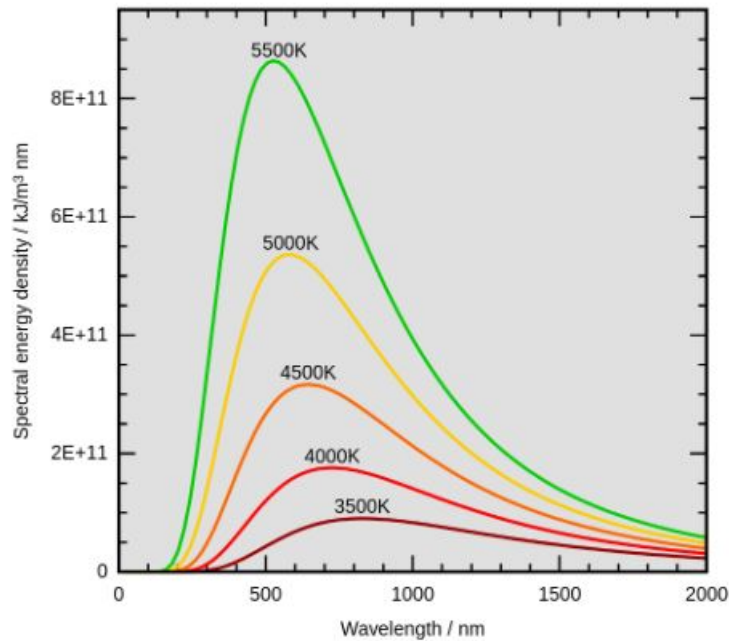


Figure 5.3: Planck's black body radiation curve

In the WAAM process, the state of the material undergoes a change from a solid to liquid melt, followed by melt to metal vapour and finally from metal vapour to plasma. The optical emissions detected in the process come from the plasma arc as well as the melt pool on the base plate. The plasma is formed by the ionization of the evaporated atoms from the melt pool. The vapour atoms get ionized after absorbing the energy from the arc during excitation. The radiation emitted by the melt pool is considered to be continuum black body radiation. As elaborated in Section 3.4, the continuum radiation emitted by free-free and free-bound electrons are the result of inelastic collisions and de-excitation of high energy free electrons with atoms and ions in the plasma. The radiation detected by the spectrometer is a superposition of characteristic emission lines with the continuum background radiation. The state of the metal vapour determines whether an emission or absorption line is detected.

The observed spectra show that the profile of the continuum radiation is a deviation from the classic Wein's displacement curve for Planck's black body radiation as shown in 5.3. A possible explanation for the presence of the 'valley' seen in the wavelength range of 400-500 could be the presence of the absorption phenomena [91].

Characteristic absorption lines (discrete lines) appear whenever an electron is excited from a lower energy level of a species to an upper (excited) energy level. Characteristic radiation (emission lines) is emitted whenever an electron decays from an upper level of a species to a lower energy level. Absorption lines from an element will appear if there are atoms of the element present in a low-density gas which lies between the detector and the source of radiation. The observed spectra also indicate that the deviation from the theoretical black body spectrum could be due to the absorption of radiation by the Fe and Cr ions in the metal vapour. The presence of the downward discontinuities on the baseline profiles could also be attributed to the absorption effect. Although, it is not the focus of this study, investigating absorption as well as emission lines could provide further insight into the correlation between the optical emission and the processing conditions. One such study was done by Ya et al. where the intensity ratio of the absorption lines was correlated to the clad geometry during laser metal deposition [64].

## 5.2 Selection of Emission Peaks

The calculation of plasma temperature and intensity ratio profiles require the selection of emission line peaks in order to process the OES data. The criteria for the selection of these peaks were elaborated in Section 3.4.2. Based on these criteria, three Cr I emission lines at wavelengths 526.54 nm, 528.76 nm and 531.84 nm were selected for calculating the plasma temperature profiles as shown in Fig 5.4. The same criteria were used to select emission lines for intensity profile calculations. Two Fe I intensity lines were selected at wavelengths 491.21 nm and 494.93 nm as shown in Fig 5.5. These selected lines were used to generate the temperature and IR profiles in the following sections.

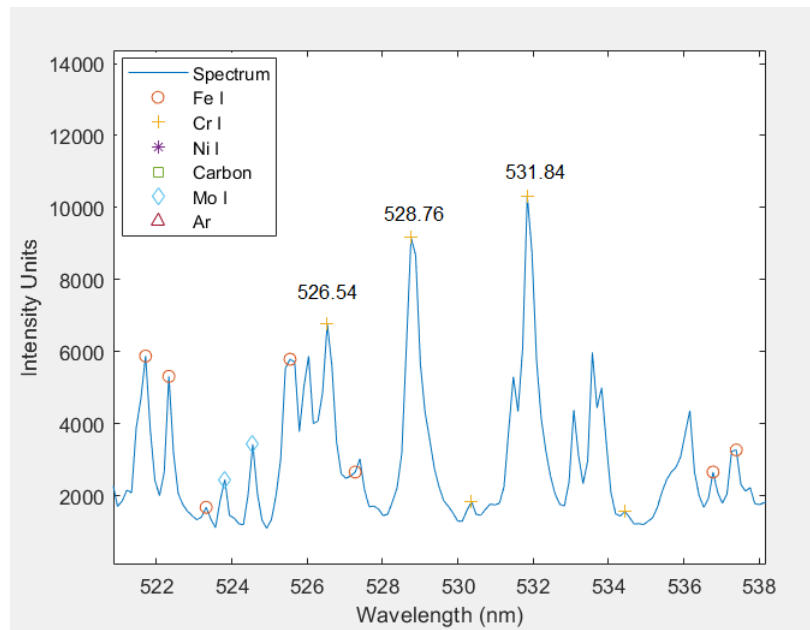




Figure 5.4: Cr I peaks chosen for temperature calculations

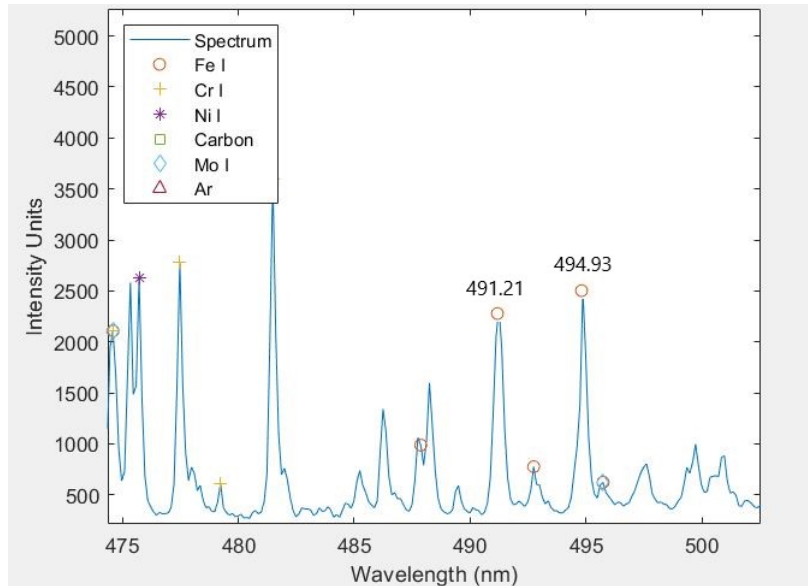


Figure 5.5: Fe I peaks chosen for intensity ratio calculations

### 5.3 Spectrometer Optimization: Signal Repeatability

The reliability of the spectrometer data collection setup was tested by verifying the repeatability of the detected signal for the same processing conditions. Two sets of weld beads were printed at travel speeds of 0.3 and 0.7 m/min as explained in the experiment setup in Section 4.5.1.6. To evaluate the repeatability of the signal, an Iron emission line at a wavelength of 444.8 nm. The intensity of the radiation at this wavelength is plotted for all the collected data in a single weld bead. The plasma temperature profiles were also plotted for each bead choosing 3 Chromium emission lines at 526.54 nm, 528.76 nm and 531.84 nm. Finally, intensity ratio profiles were calculated for both sets of welds by studying Fe emission lines at 491.21 nm and 494.93 nm. These lines were selected from different wavelength ranges and atomic species in order to validate signal repeatability. The peak intensity, plasma temperature and intensity ratio profiles for both sets of welds are presented in Figures 5.6 and 5.7. The processed signals from 2 trials with the same processing conditions are superimposed over each other in order to compare the profiles. The same profiles are calculated for a pair of beads with a travel speed of 0.3 m/min, but the observation angle of the spectrometer was changed in order to illustrate the difference in the detected signals for the same processing conditions when the observation angle is disturbed, and is shown in Fig 5.8

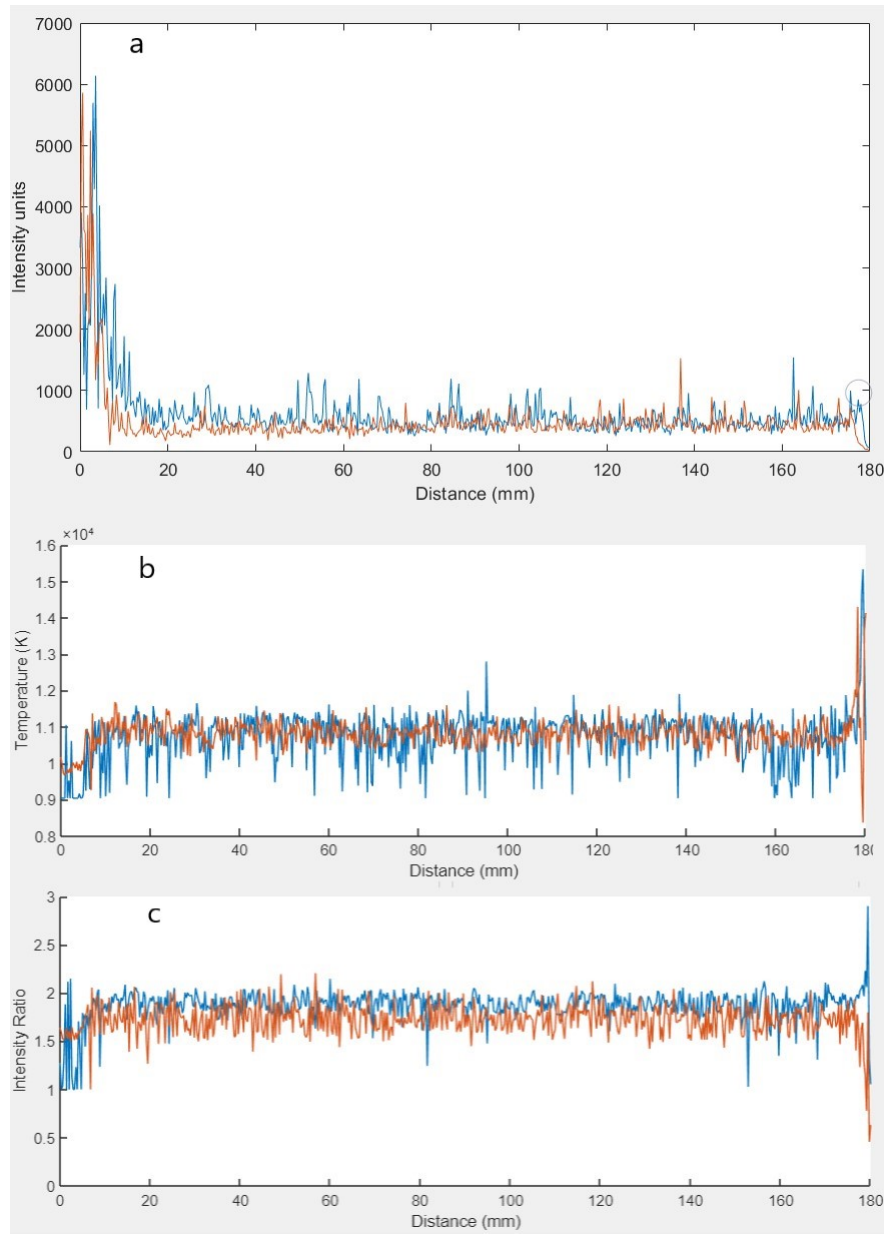


Figure 5.6: Repeatable signal comparison at  $TS = 0.7$  m/min a) Intensity profile b) Plasma Temperature profile c) Intensity Ratio profile

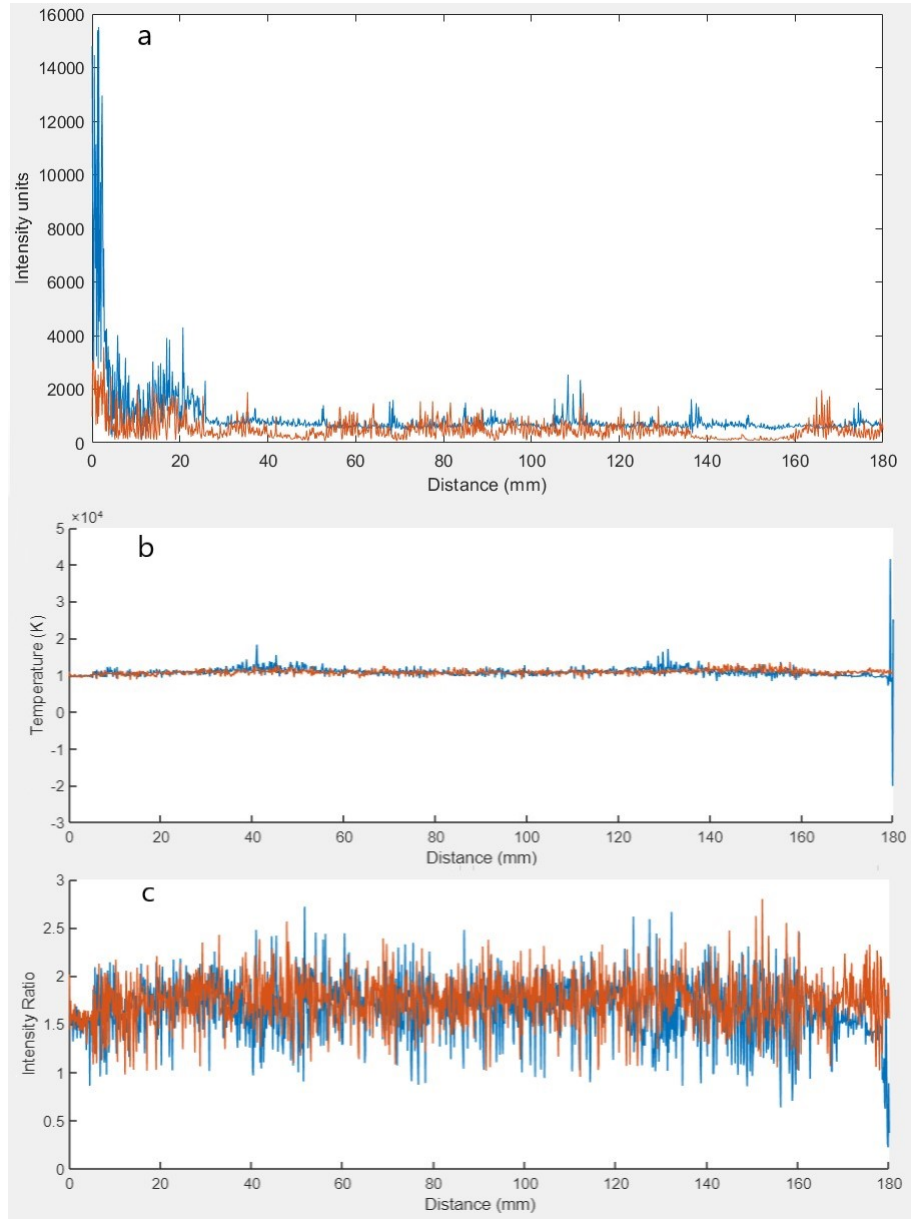


Figure 5.7: Repeatable signal comparison at  $TS = 0.3$  m/min a) Intensity profile b) Plasma Temperature profile c) Intensity Ratio profile

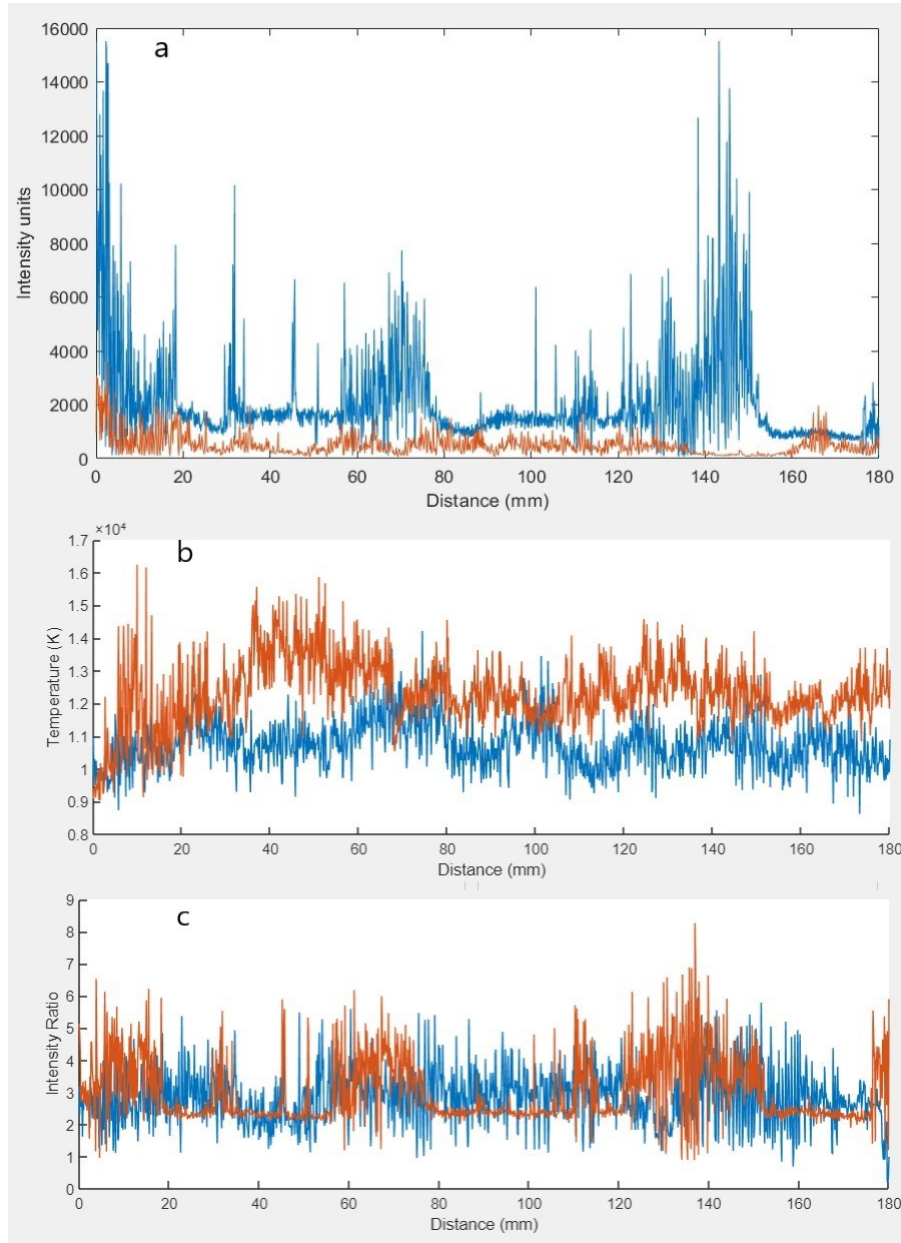


Figure 5.8: Example of non repeatable signal for same processing conditions at  $TS = 0.3$  m/min a) Intensity profile b) Plasma Temperature profile c) Intensity Ratio profile

From the graphs that were obtained in this experiment, it can be inferred that repeatable signals can be obtained if the processing conditions as well as the spectrometer configuration remains unchanged while depositing the weld beads under the same process conditions. Disturbing the spectrometer configuration can be a possible source of error in OES calculations.

For a travel speed of 0.7 m/min, the intensity of the Fe I peak at 444.8 nm follows the same profile for both beads. The profiles for the plasma temperature and intensity ratio are also similar for the pair of identical welds. The similarity in the profile characteristics of peak intensity, plasma temperature and intensity ratio is also shown for the pair of welds deposited with a travel speed of 0.3 m/min. Small variations between the profiles are observed,

but these differences are minimal and can be due to small vibrations of the welding torch causing collimator lens to move slightly. The superimposed signals in Fig 5.8 do not show the same profile even though the process parameters were the same with just a difference in the spectrometer configuration and observation angle. If the profiles of the superimposed signals show different features for the same processing conditions, it cannot be used for comparing OES profiles while analysing processing conditions.

## 5.4 Software Validation: Peak Characterization

### 5.4.1 Results

In this experiment, different material combinations of wire feedstock and shielding gas were used in the WAAM setup. This experiment was done to illustrate the versatility of the developed software. Only one combination of materials were used in this study. However, this experiment demonstrated that the post processing algorithms that were developed can be used for any WAAM system. Fig 5.9 shows the characterized peaks of the system with 316L wire and Inomaxx shielding gas. Fig 5.10 shows the characterized peaks of the system with NiCrMo wire and Ferromaxx shielding gas and finally Fig 5.11 shows the characterized peaks of the system with X89 steel wire and argon shielding gas.

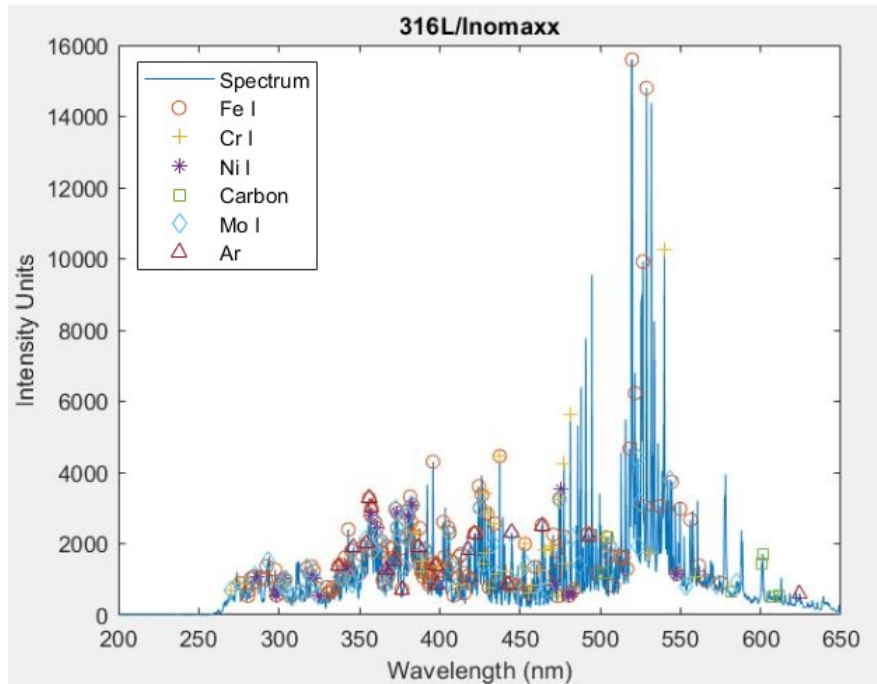


Figure 5.9: Peak characterization of signal from with 316L wire and Inomaxx shielding gas

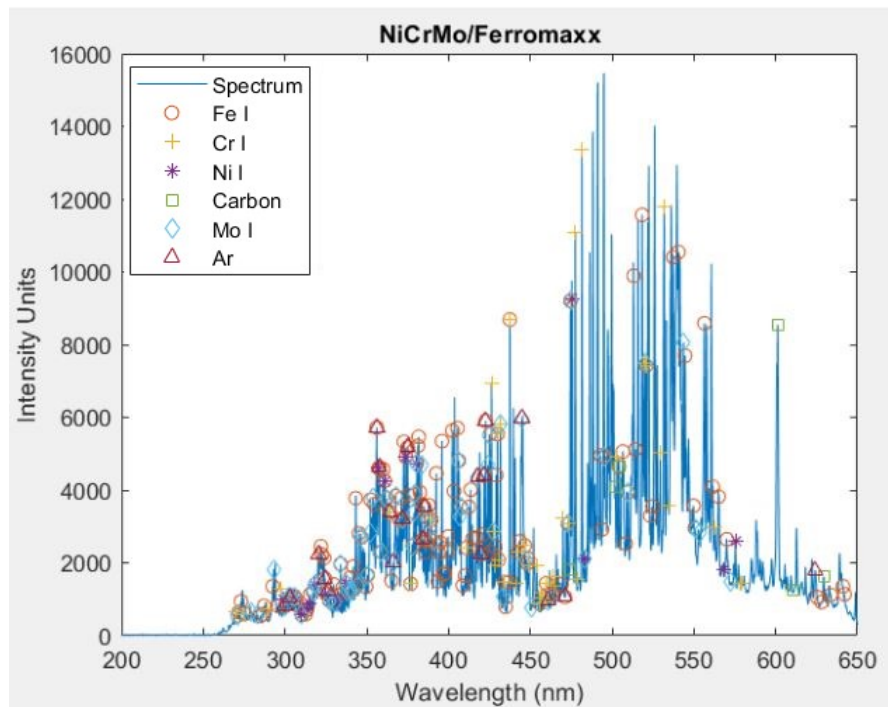


Figure 5.10: Peak characterization of signal from with NiCrMo wire and Ferromaxx shielding gas

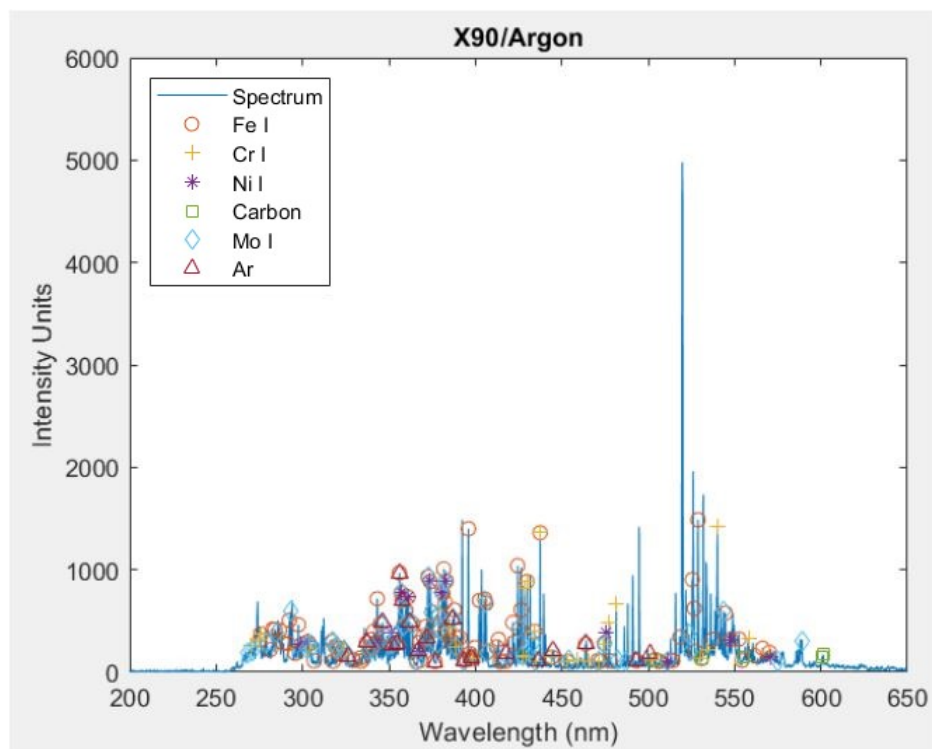


Figure 5.11: Peak characterization of signal from with X89 steel wire and Argon shielding gas

### 5.4.2 Discussion

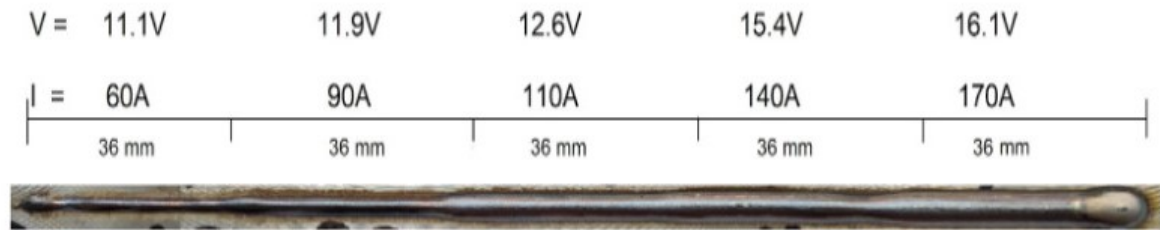
It was examined that the software is able to identify and characterize emission peaks detected for different material combinations. However, not all of the peaks in the spectrum are identified by the software. This could be attributed to the software only characterizing the most common ionization state of the metal species - Fe I, Cr I and Ni I. This is observed because the first ionization state of the metals in the system have the highest probability of electron transition ( $A_{21}$ ) from the NIST database [86]. Although other ionization states are present in the system, they are not stable and hence cannot be used for the plasma characterization. It can also be observed that some emission peaks are characterized by more than one element. This could be due to the fact that both the elements have an emission peak listed in the NIST database where the difference in their wavelengths is less than the resolution of the spectrometer (0.135 nm) and the collected raw spectra are all superimposed with the detectable emission sources multiple species in which the overlap of the peaks can occur. To avoid errors in processing OES data, emission lines are selected such that they are matched to a single element. The peak characterization software can identify emission lines in the spectrum for any material combination, provided the constituent elements are known and the peaks fall within the detection range of the spectrometer.

## 5.5 Software Validation: Ramping Test

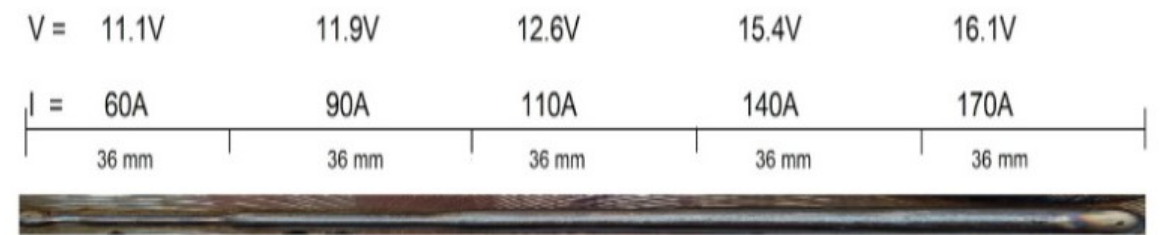
In this experiment, the current and voltage input to the WAAM system was incrementally increased in five steps and the collected OES signals were processed to investigate the potential correlations with the processing conditions. A 316L wire was deposited on an S355 steel base plate with Inomaxx Plus shielding gas. A chromium emission peak with a wavelength of 528.76 nm was selected to study the peak intensity for all travel speeds. It is to be noted that this peak does not have any special characteristics and any emission line can be chosen if it is consistently observed for all the OES data files obtained. The plasma temperature and intensity ratio profiles were also plotted for all speeds to study correlations with ramping conditions. The selection of emission line peaks for these calculations are described in Section 5.2 and shown in Fig 5.4 and Fig 5.5 The weld beads printed in different travel speeds are shown in 5.12. It is observed that the width of the weld bead increases with each ramping step as the current and voltage input were increased.



TS = 1.2 m/min



TS = 0.7 m/min



TS = 0.3 m/min

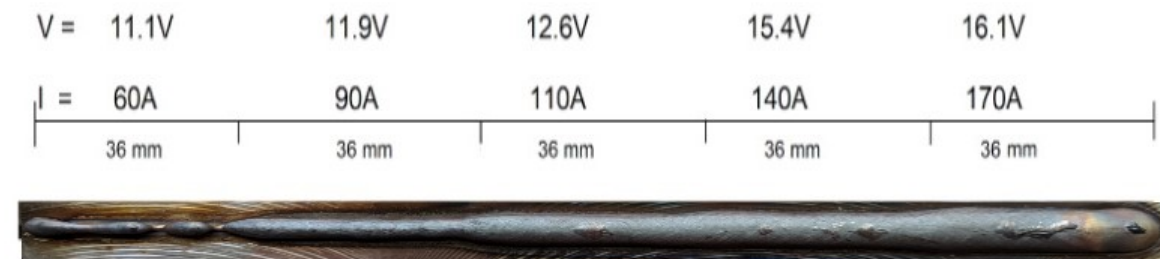


Figure 5.12: Weld beads for different travel speeds in ramping conditions



### 5.5.1 Intensity Profiles

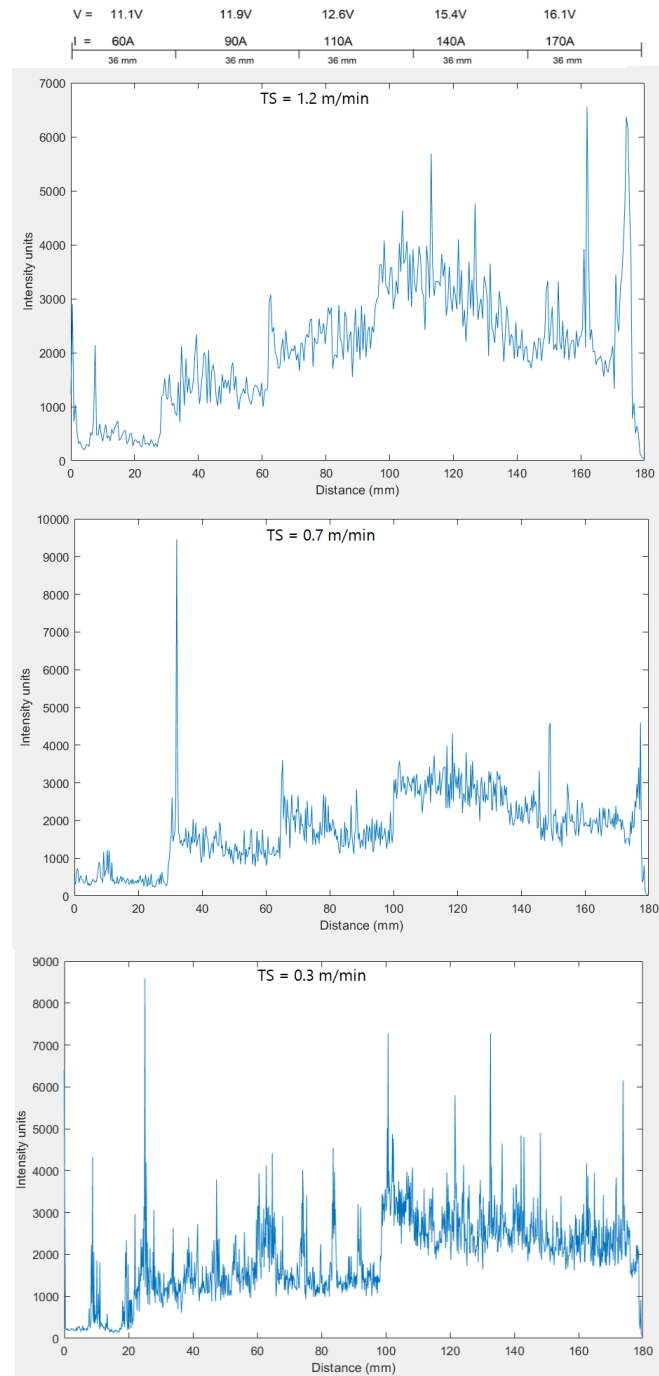


Figure 5.13: Intensity profile of a Chromium emission peak 527.2 nm

For all travel speeds, the intensity of the emission peak shows a strong correlation with the increasing current and voltage conditions. The intensity of the peak increases with the increasing heat input for all speeds. The final ramping step, where the current and voltage reduce to the arc off (crater conditions with lower values of current and voltage), was also noticed. The intensity profile can be attributed to the increasing input energy provided to

the wire. A higher current corresponds to more number of electrons flowing through the wire and the plasma Arc. As seen in Equation 3.9, the intensity of light emitted by the plasma arc is proportional to the density of electrons in higher energy levels. Thus, the intensity profile shows a stepped profile when the input current and voltage are ramped incrementally.

### 5.5.2 Temperature and Intensity Ratio Profiles

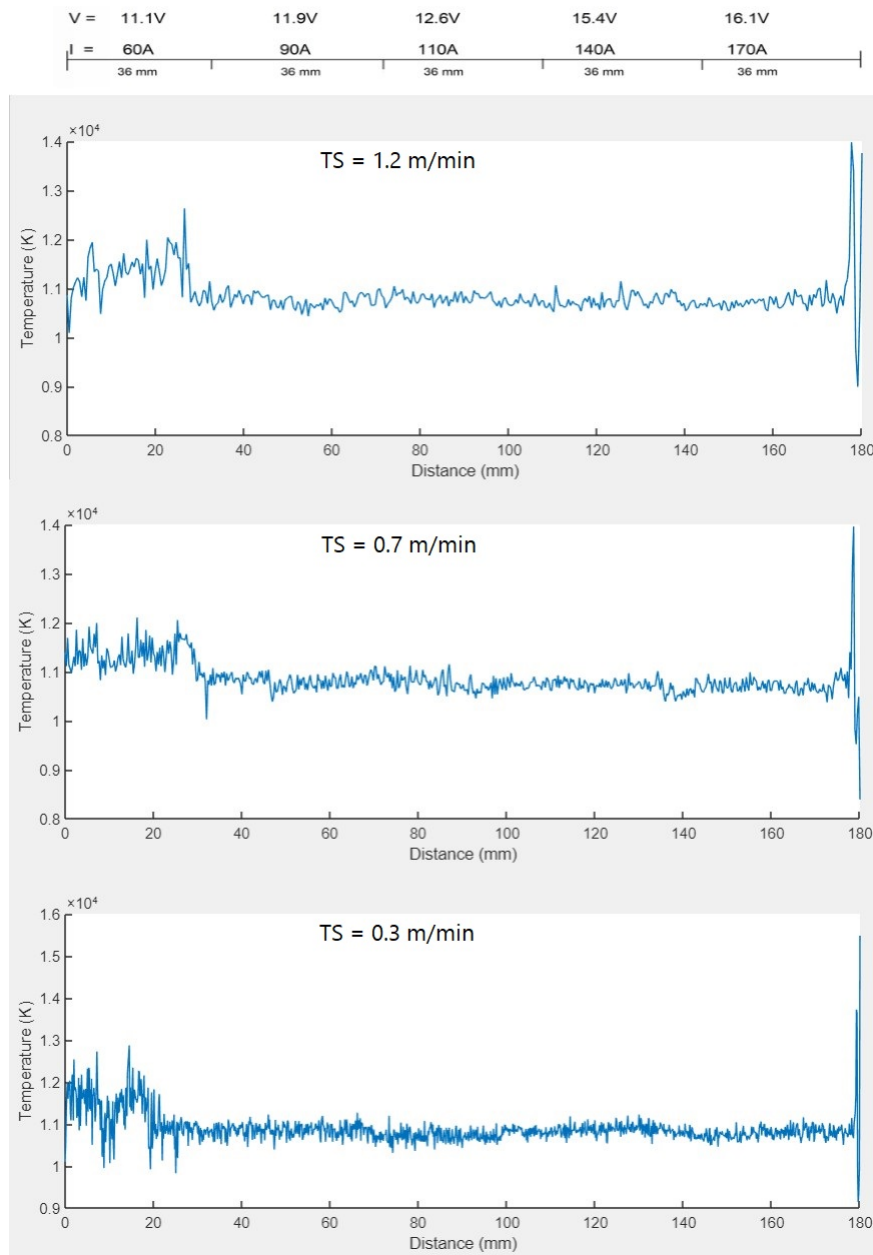


Figure 5.14: Plasma Temperature profiles from Ramping Test for different travel speeds

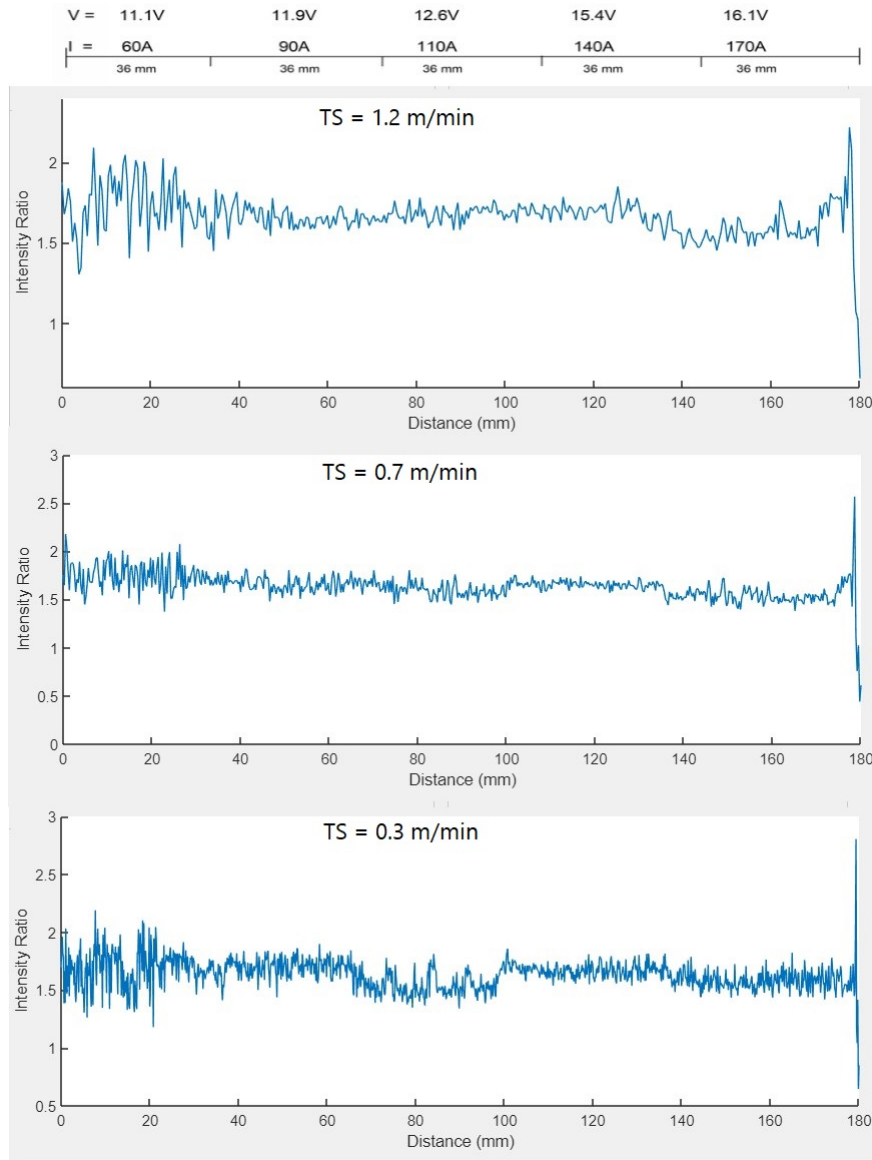


Figure 5.15: Intensity Ratio from Ramping Test for different travel speeds

The temperature and intensity ratio for all travel speeds in ramping conditions show the same profile. The temperature profile shows instability in the first ramping region, before stabilizing to a more stable profile. However, the temperature profile does not show any observable variation when the process parameters are ramped in the next four ramping regions.

The intensity ratio also shows a similar profile to the plasma temperature. There is an instability observed in the first ramping region for all travel speeds. Although each ramping region can be distinguished in the intensity ratio profile, the correlation with the processing conditions is not strong enough to characterize the increasing current and voltage input. These observations can be explained by correlating the processed signal with the heat input into the system. For the first ramping region, the current and voltage values are the lowest and the arc energy is insufficient for stable metallic bonding. This is also reflected in the uneven weld

appearance of the first ramping region seen in Fig 5.12. However, the arc energy is sufficient for stable metallic bonding from the second ramping region and is thus not reflected in the temperature profile. The intensity ratio is more sensitive to processing conditions compared to the plasma temperature, and reflects a small change in value at the location where the heat inputs are ramped. However this change is too small to accurately characterize the ramping process. A possible reason for this observation is that the Super Active Wire Production metal transfer mode is self-stabilizing, and the feedback controlled process maintains a stable plasma arc after the heat input energy is sufficient for stable metallic bonding.

There are two key results from this experiment - the intensity of the detected radiation from the plasma increases as a function of the electrical energy input into the system. The plasma temperature and intensity ratio profiles can be used to characterize the beginning of stable metallic bonding, but difficult to accurately describe the ramping conditions of the experiment at the moment. More dynamic variation tests are needed to be performed to further explore its potential.

## **5.6 Software Validation: Anomaly Detection**

### **5.6.1 Results**

In this experiment, the collected OES data was used to characterize the presence of an intentionally deposited ceramic as anomaly on the base plate for three different torch travel speeds - 1.2 m/min, 0.7 m/min, and 0.3 m/min. A 316L wire was deposited on an S355 steel base plate with Inomaxx Plus shielding gas. OES data was collected for all three travel speeds to compare peak intensity, plasma temperature and intensity ratio profiles. An emission peak at a wavelength of 528.76 nm was chosen to study the intensity profile. The selected wavelengths for plasma temperature and intensity ratio calculations were presented in Section 5.2 and shown in Fig 5.4 and Fig 5.5 respectively. The results of this experiment are presented in this section. These results are discussed and further validated with the help of secondary investigation techniques like optical microscopy, analysing voltage waveforms and high-speed camera footage.

### 5.6.1.1 Intensity Profiles

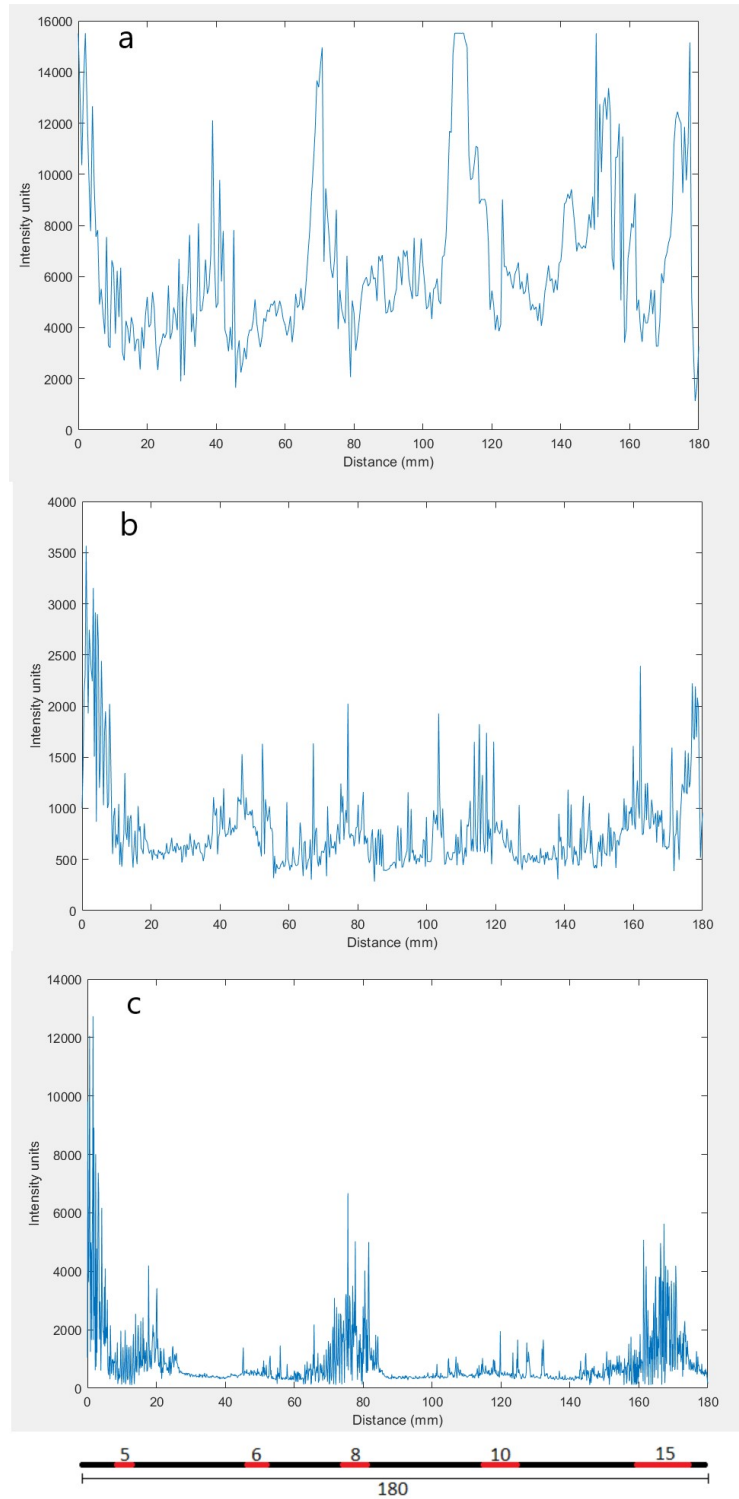


Figure 5.16: Intensity of Cr I emission line at wavelength of 528.76 nm at a) TS = 1.2 m/min b) TS = 0.7 m/min c) TS = 0.3 m/min

The intensity profiles shown in Fig 5.16 at a TS of 1.2 m/min show clear peaks at the locations of the deposited ceramic anomaly. The ignition of the arc at the start of deposition shows instability at all TS values. The intensity profiles obtained for TS of 0.7 m/min and 0.3 m/min does not show a characterizable correlation with the presence of all the ceramic strips. The intensity profile at 0.7 m/min does show peaks at the location of the anomaly, but there are multiple peaks at other locations as well making it difficult to characterize the anomaly's presence. For a TS of 0.3 m/min, the intensity profile appears as peaks only for three out of the five deposited ceramic strips, and is thus not reliable for characterizing the presence of the anomaly.

### 5.6.1.2 Plasma Temperature

TS = 1.2 m/min

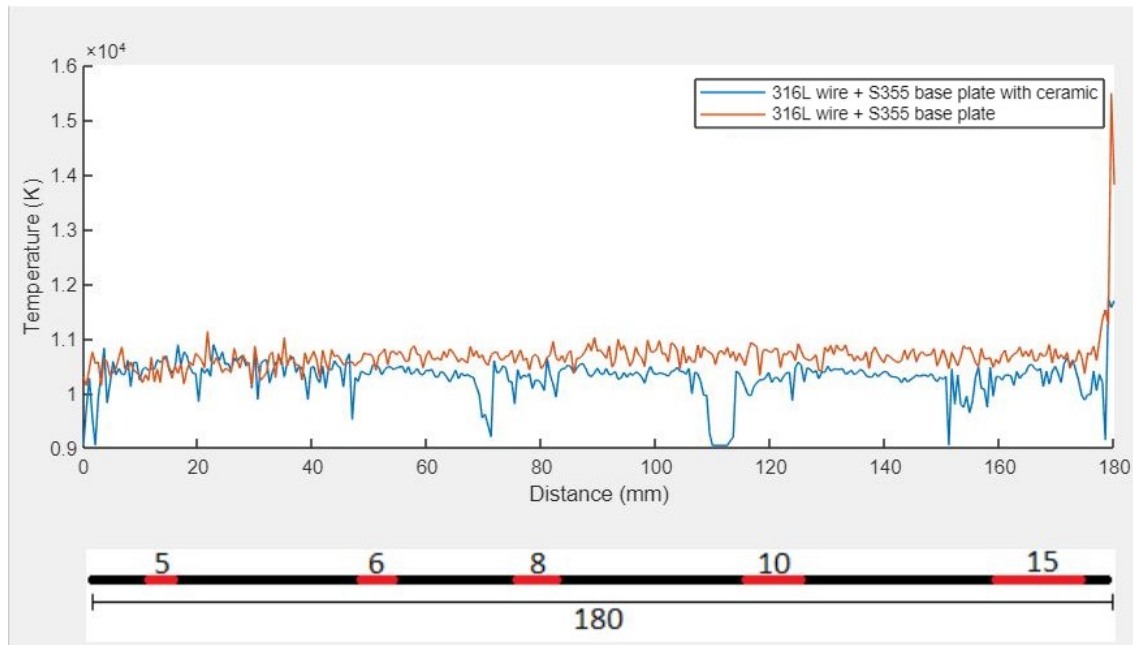


Figure 5.17: Comparison of plasma temperature profiles in anomaly detection test at TS = 1.2 m/min

The plot of plasma temperature versus distance is shown in Fig 5.17 for both sets of welds printed at a TS of 1.2 m/min. It can be seen that the presence of the ceramic pattern can be differentiated based on the superposition of both sets of welds. The signal obtained from the weld without the ceramic pattern shows a relative uniform temperature profile with only small variations. The profile obtained from the weld printed on the ceramic pattern however shows sharp drops in plasma temperature when the torch deposited metal over the ceramic regions. The drop in temperature is not the same for each of the 5 ceramic strips in the base plate. There is an instability and lowering of the temperature during arc ignition that is seen in both profiles. The reduction in temperature is not the same for all the ceramic strips. However, this temperature reduction does not have any correlation with the size of the simulated anomaly.

TS = 0.7 m/min

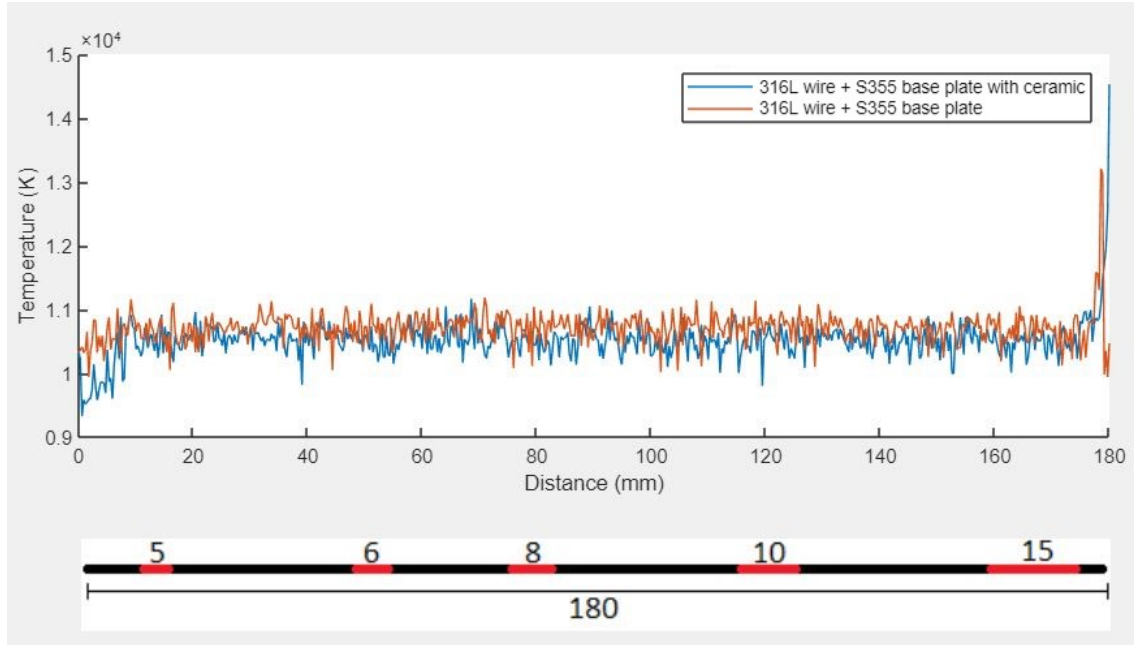


Figure 5.18: Comparison of plasma temperature profiles in anomaly detection test at TS = 0.7 m/min

For a travel speed of 0.7 m/min, there is no characterizable difference between the temperature profiles of the weld beads with and without the ceramic pattern as seen in Fig 5.18. An instability in the temperature profile was observed at the starting of the process but after the signal stabilizes, there is no discernible difference between the OES signals obtained from printing on both the base plates.

**TS = 0.3 m/min**

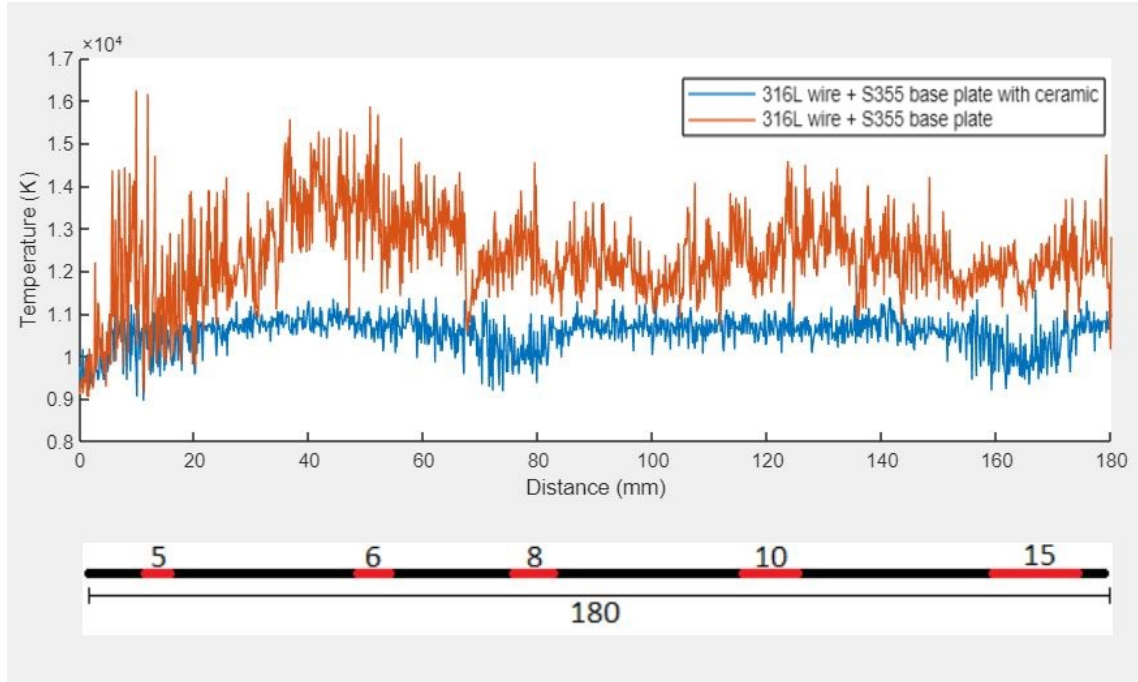


Figure 5.19: Comparison of plasma temperature profiles in anomaly detection test at TS = 0.3 m/min

For a travel speed of 0.3 m/min, the temperature profiles indicates the presence of only 2 out of the 5 ceramic patterns on the base plate as seen in Fig 5.19. The temperature profile shows instability near at the starting of the deposition for both sets of welds. When the torch deposited metal over the ceramic patterns of width 8mm and 15mm, it showed a drop in temperature, but it is not significant enough to be able to characterize the presence of the ceramic pattern. Another observation was the signal obtained from the ceramic-free printing environment also showed a higher degree of variation and instability compared to the temperature profiles obtained from the other 2 travel speeds.



### 5.6.1.3 Intensity Ratio

TS = 1.2 m/min

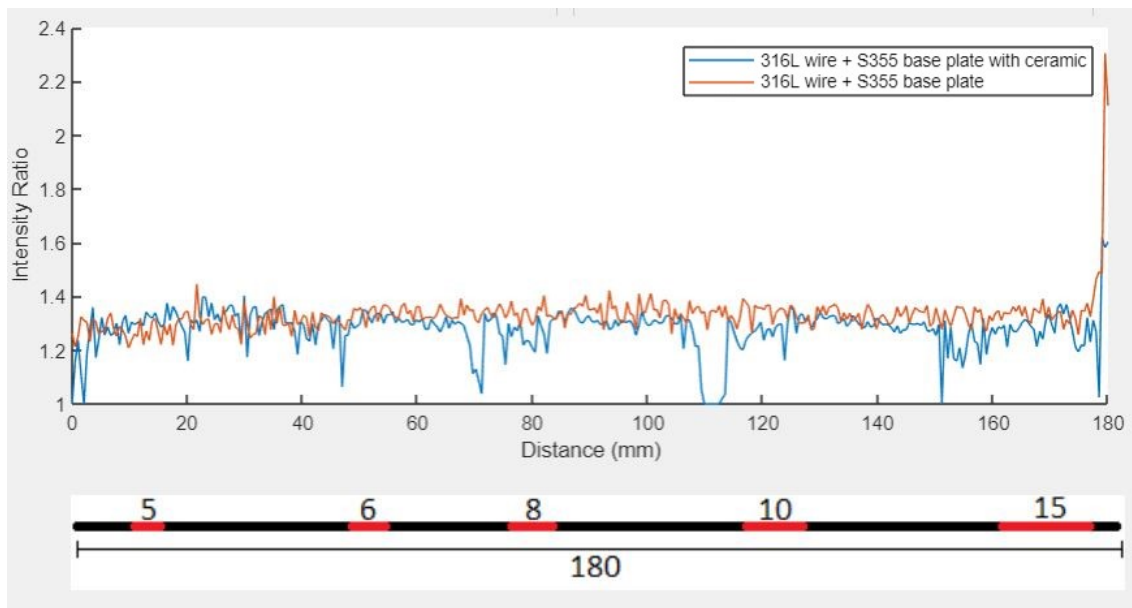


Figure 5.20: Comparison of intensity ratio profiles in anomaly detection test at TS = 1.2 m/min

The intensity ratio profile for a travel speed of 1.2 m/min has a similar trend to the calculated temperature profile, as shown in Fig 5.20. The presence of the simulated ceramic anomaly can be differentiated from IR profile without the ceramic. The intensity ratio drops when it enters a ceramic region and then rises back to the baseline value. Although the reduction of the intensity ratio is seen for all the ceramic strips, the signal does not reflect the varying size of the ceramic pattern.

**TS = 0.7 m/min**

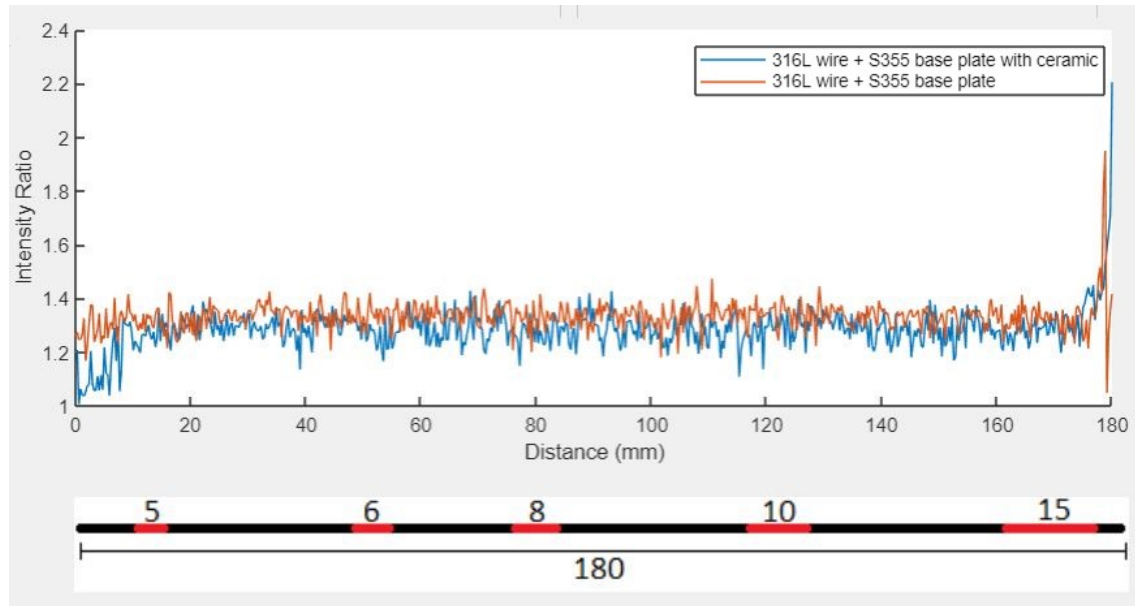


Figure 5.21: Comparison of intensity ratio profiles in anomaly detection test at TS = 0.7 m/min

The intensity ratio profiles for the weld beads printed with and without the ceramic pattern on the base plate have similar profiles. Although the profile of the weld printed on the ceramic has a lower intensity ratio on average, the profiles cannot be used to differentiate between printing on a clean base plate and with a ceramic pattern deposited on it, as shown in Fig 5.21.

**TS = 0.3 m/min**

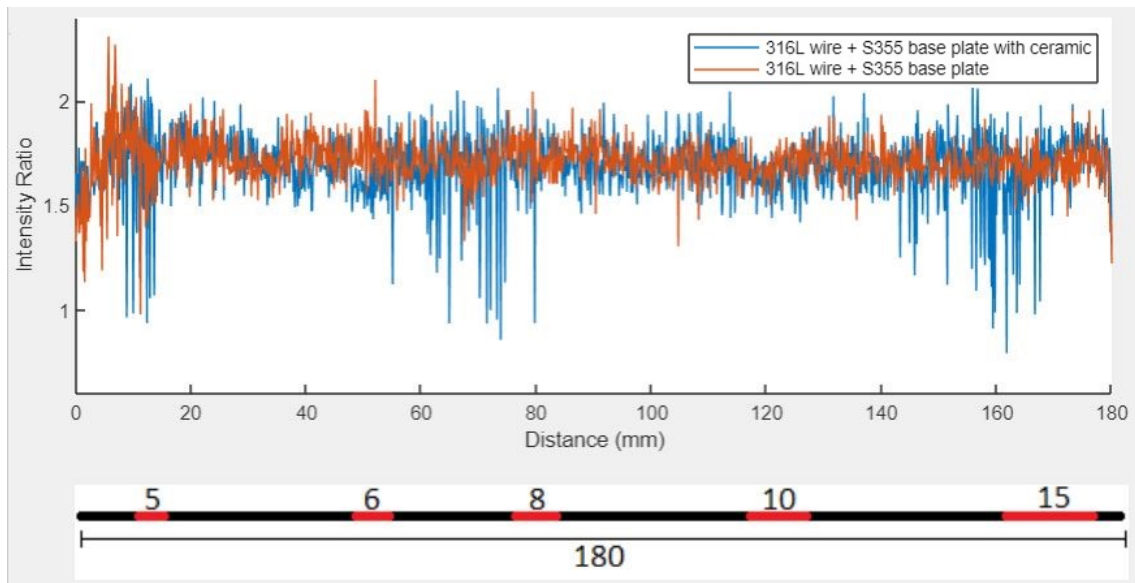


Figure 5.22: Comparison of intensity ratio profiles in anomaly detection test at  $TS = 0.3$  m/min

The intensity ratio profiles for the weld beads printed at a travel speed of 0.3 m/min indicated that IR values can be correlated to the presence of the ceramic, but is not consistent for all of the ceramic depositions on the base plate, as seen in fig 5.22. The IR signal collected from printing on a clean base plate shows instability and large variation in signal across the whole length of the bead. The variation of IR observed in this signal is greater than what was seen for a travel speed of 0.7 m/min and 1.2 m/min. The profile collected from the weld printed on the ceramic pattern shows a reduction of the intensity ratio where the ceramic strip width was 5 mm, 6 mm, 8 mm and 15 mm. The intensity ratio is lower than the baseline of the profile between the ceramic strips of 6 mm and 8 mm. The intensity ratio does not correlate to the presence of the ceramic strip of 10 mm.

### 5.6.2 Discussion

The peak intensity, plasma temperature and intensity ratio profiles plotted for different travel speeds shows that the collected OES signal can be correlated to processing conditions, but only for certain values of the torch travel speed. For the fastest travel speed of 1.2 m/min, the peak intensity profile showed an increase in the presence of the ceramic anomaly, and both the plasma temperature and intensity ratio profile showed a reduction in signal when printing over a ceramic region. For the slowest travel speed of 0.3 m/min, the peak intensity and intensity ratio profile has a stronger correlation to the presence of the ceramic compared to the plasma temperature, but the signal does not reflect the presence of all the ceramic deposited strips. Additionally, the signal obtained from the deposition on the ceramic free metal surface also showed a higher level of instability in both the plasma temperature and intensity ratio profiles compared to the other two travel speeds, indicating that metal deposition at a travel speed of 0.3 m/min results in the plasma arc being less stable compared to the other travel speeds in this study. The intensity, plasma temperature and intensity ratio profiles could not be correlated to the presence of the ceramic pattern for the intermediate travel speed of 0.7 m/min. Therefore, under the stable process conditions, using the OES for anomaly detection is promising.

The intensity of light emitted by the plasma is proportional to the density of electrons and increases with arc current, as studied in the ramping test and seen in Equation 3.9. The increase in the intensity of the emission for  $TS$  of 1.2 m/min could be attributed to the fact that the presence of the anomaly affects the flow of electrons from the wire to the base plate and could accumulate in the plasma arc, and more number of excited electrons are detected in the plasma. An explanation for the lowering of temperature and IR values could be that the presence of the ceramic anomaly affects the surface tension of the melt pool by acting as a barrier between the liquid metal drop and the melt pool. The presence of an anomaly would also affect the flow of electrons (current) from the liquid metal drop to the base plate, and thus affect the creation of the plasma. The lowering of the temperature and IR profiles indicates that the anomaly lowers the heat input during the deposition process. The lower heat input could be due to the recombination of the accumulated electrons above the ceramic region with the electrons input into the system via the welding current. This observation of the increase in intensity and reduction in temperature and IR has a strong correlation with the OES signals only for a travel speed of 1.2 m/min and not for 0.3 m/min or 0.7 m/min is

difficult to be explained with just the temperature and intensity ratio calculations and requires further investigation with different designed experiments. A possible explanation could be the limitation of the integration time of the spectrometer that reduces the sensitivity of the observed spectrum.

To validate the above hypothesis and investigate the correlation of the travel speed with the observed OES signal, independent investigation techniques were used to study the metal transfer process in greater detail. Voltage and current data was collected from the experiment at a frequency of 25000 Hz using a Hall effect based sensor. A Phantom High Speed camera was also used to take footage of the metal transfer process with the ceramic impurity deposited on the base plate at 4100 FPS. Data from the V-I sensor was used to differentiate the current and voltage waveforms from the welds that were deposited with and without the ceramic. The high speed camera footage was used to study the metal transfer process in greater detail and correlate it with the high frequency current and voltage data and the processed OES spectrum. The effect of the anomaly on the geometry of the weld bead and shape of the weld profile was investigated by studying cross sections of the base plate using optical microscopy.

### 5.6.2.1 High Frequency Voltage Analysis

The WAAM setup in this study used Super Active Wire Production mode, a modification of the short-circuit metal transfer mode discussed in Section 3.2. A voltage difference is maintained between the torch tip and the base plate, which was clamped to the welding table. The liquid metal drop from the torch tip creates a short circuit when it bridges the gap between the wire tip and base plate. After the metal transfer, the voltage returns to the set input value resulting in the ignition of the plasma arc. V-I data was collected in the anomaly detection experiment using a Hall effect based sensor at a frequency of 25000 Hz. For every travel speed, voltage data was compared between the weld beads printed with and without the ceramic deposition on the base plate. Fig 5.23 shows the voltage waveform of metal deposition on a ceramic-free base plate at a TS of 0.7 m/min.

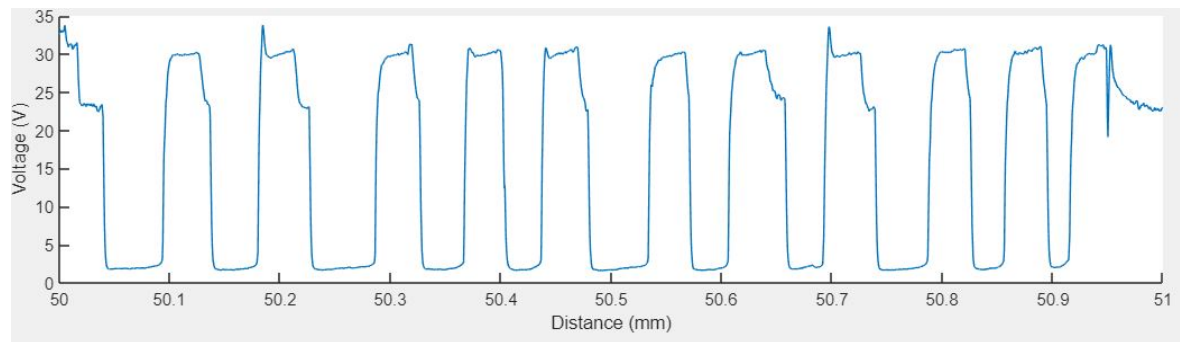


Figure 5.23: Detected voltage waveform of SAWP metal transfer mode on a ceramic-free base plate at a TS of 0.7 m/min

In the previous section it was hypothesised that the reduction of the plasma temperature and intensity ratio signals observed during metal deposition over a ceramic region was caused by the ceramic particles interfering with the metal transfer process by affecting the conductivity of the base plate. This hypothesis is validated in this section by comparing the detected voltage waveforms with and without the ceramic pattern on the base plate.

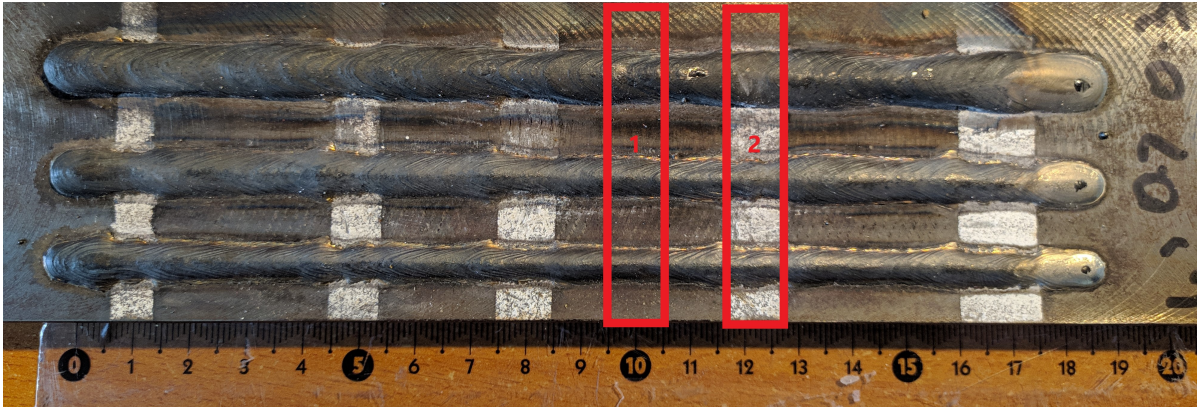


Figure 5.24: Selected regions for comparative study of voltage waveforms

Fig 5.24 shows the three weld beads that were printed on the base plate with the ceramic deposition. Two regions 1 and 2 are selected to study the voltage waveforms - region 1 does not have any ceramic present and region 2 has ceramic present. The voltage waveforms from a 2mm wide area in these regions were superimposed with the data collected from the weld beads printed on a clean base plate for all travel speeds and are presented in Fig 5.25, Fig 5.26 and Fig 5.27.

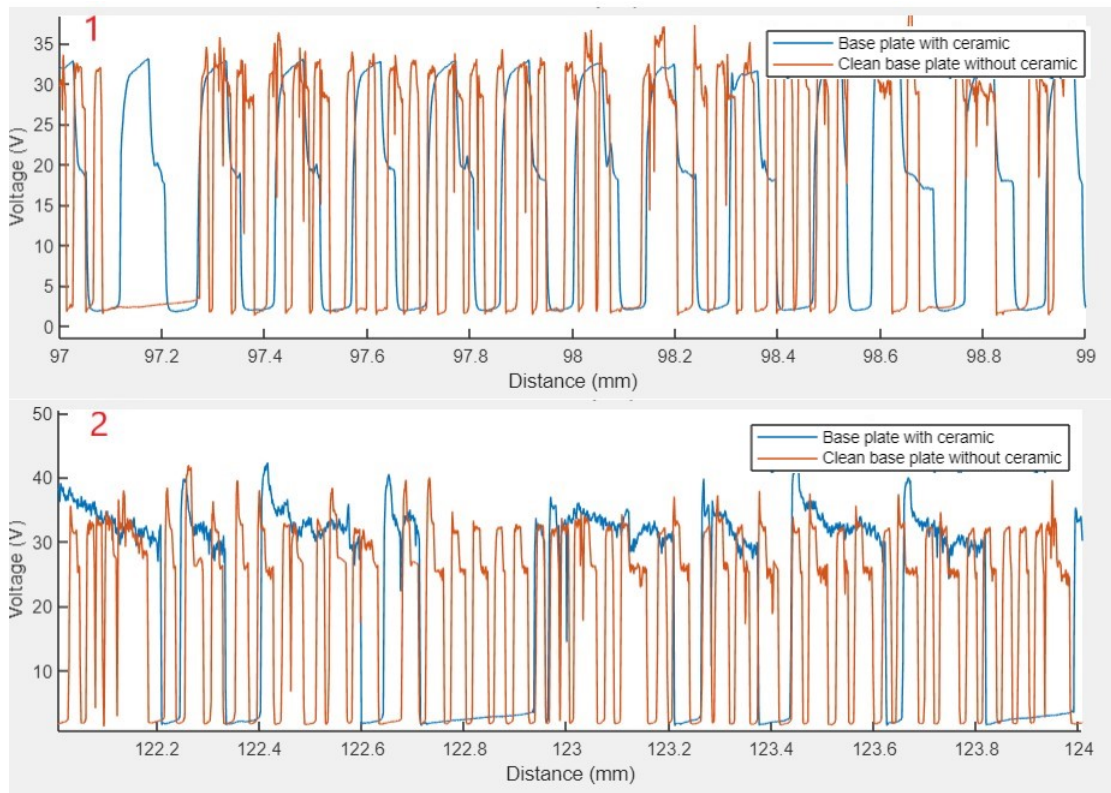


Figure 5.25: Voltage waveform from region 1 and 2 at TS = 1.2 m/min



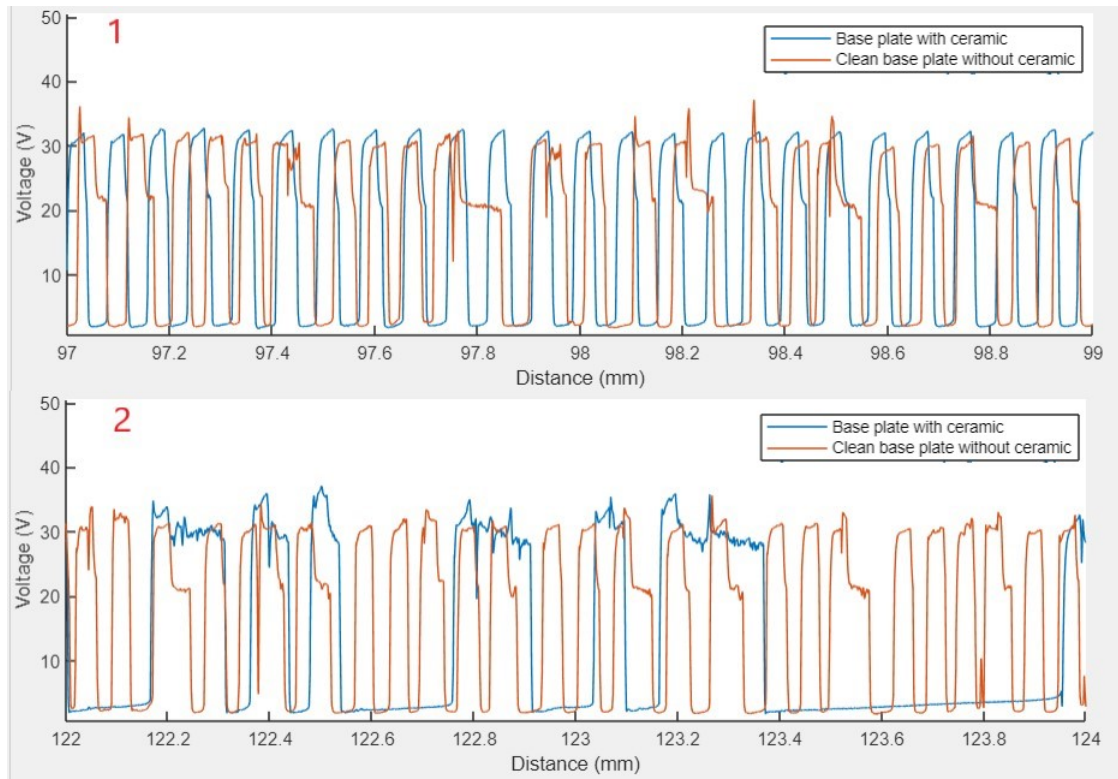


Figure 5.26: Voltage waveform from region 1 and 2 at  $TS = 0.7$  m/min

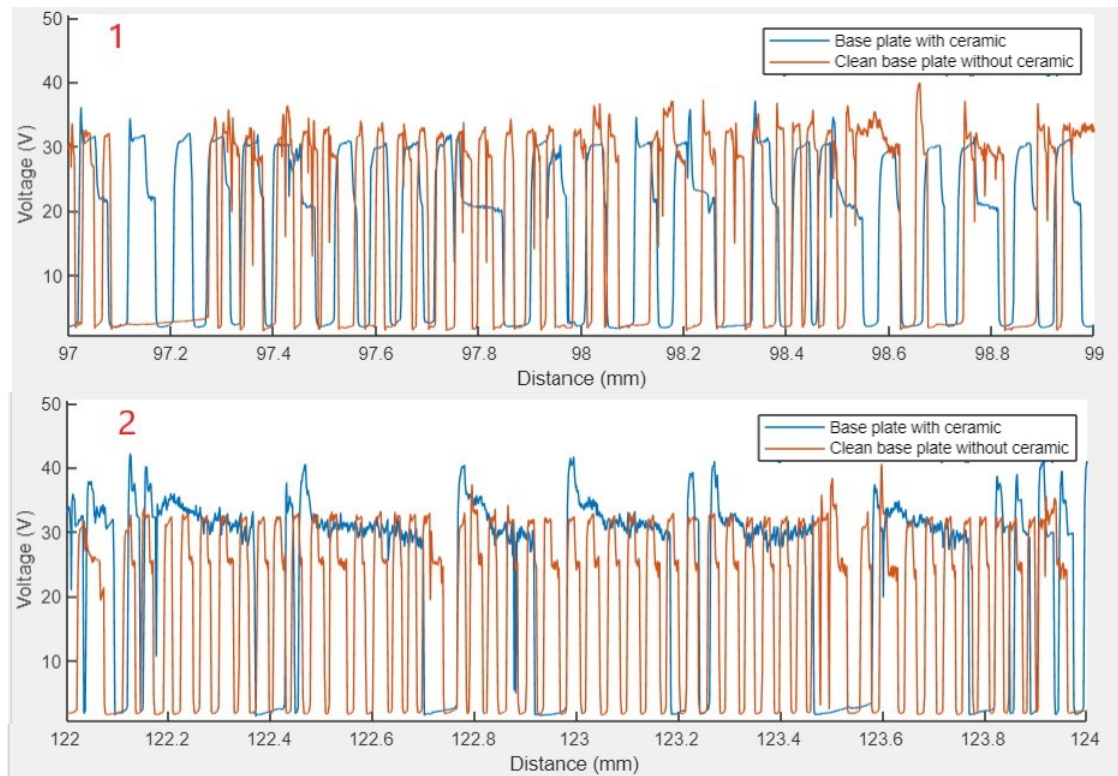


Figure 5.27: Voltage waveform from region 1 and 2 at  $TS = 0.3$  m/min

The collected high-frequency voltage data could be used in tandem with OES to validate the spectroscopic observations in a monitoring system by quantifying the short-circuit data and correlating it with the presence of the anomaly. However, this quantification was not the focus of this study and the comparative voltage waveforms were only used to qualitatively validate the OES observations.

For all the travel speeds, the voltage waveforms from for regions 1 and 2 show different profiles. Region 1 for all travel speeds shows a voltage waveform that is similar for both the clean base plate as well as the base plate with the ceramic deposition. Small inconsistencies can be attributed to localised instability in the plasma arc, but these observations were not consistently present in the waveforms. The voltage waveforms in Region 2 for all travel speeds show that the number of short circuits is significantly lesser compared to Region 1. Even after the voltage reaches the minimum value, the short-circuit time in Region 2 is higher than in Region 1.

These results support the hypothesis proposed in Section 5.6.2. The presence of the ceramic pattern prevents the liquid metal drop at the wire tip from detaching and falling into the melt pool. The instability in the voltage waveform between short circuits indicates that the ceramic acts as a barrier, affecting the surface tension of the melt pool and detachment of the droplet from the wire. Arc ignition takes place after the liquid metal is detached and the voltage goes back up to the peak value. Lesser number of short circuits per unit time can affect the density of metal ions in the plasma and concentration of the metal vapour, and as a result reflect in the plasma temperature and intensity ratio profiles calculated from the detected OES signal. This hypothesis is further validated by high speed footage of the printing of a metal bead as it enters the ceramic region.

#### **5.6.2.2 High-speed camera investigation**

A Phantom High Speed camera was used to take video footage of the metal transfer process at a frame rate of 4100 FPS. The camera collected images from the metal deposition process before the torch prints over the ceramic region and the deposition on the ceramic. A monochromatic laser source was used to illuminate the torch tip and the melt pool. The camera captured the laser's reflection from the wire and liquid metal at a high frame rate to investigate the metal transfer process. The camera setup captured the deposition of a 316L wire on an S355 steel base plate with a torch speed of 0.7 m/min at a welding current of 160 A and a welding voltage of 18 V.

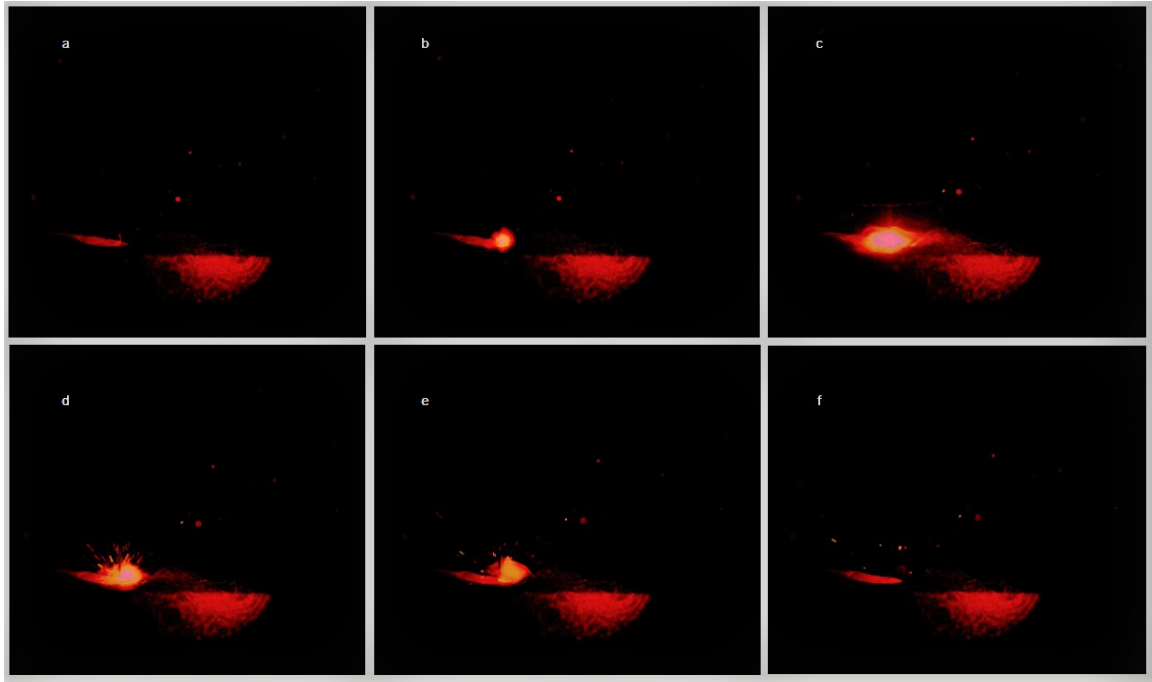


Figure 5.28: High speed camera footage of metal transfer in ceramic region a) Before arc ignition b) Arc ignition c) Wire pulled back up by servo motor d and e) Drop detachment f) Arc off

Fig 5.28 shows a series of images captured by the camera when printing on a metal region without the presence of the ceramic. Figure ‘a’ to ‘b’ shows the ignition of the plasma arc due to the applied current and voltage to the wire and creates a liquid metal drop at the wire tip. In ‘c’, the servo motor of the robot arm pulls the wire upwards along with the liquid drop, increasing the plasma intensity. ‘d’ and ‘e’ shows the detachment of the metal droplet into the melt pool. This detachment causes the liquid metal in the melt pool to spatter outwards and this process is seen to repeat again.

Fig 5.29 shows a series of images captured when depositing over the ceramic region. It is observed that the ignition of the plasma arc causes the liquid metal droplet to form at the torch tip. However, the ceramic anomaly affects the surface tension of the melt pool and reduces the force that causes the drop to detach. The drop does not detach into the melt pool every time the wire is drawn upwards by the servometer of the robot arm. The sequence of images in Fig 5.29 shows that the plasma arc increases and decreases in intensity when the wire is drawn upwards - it is drawn up and down several times before the droplet is detached.



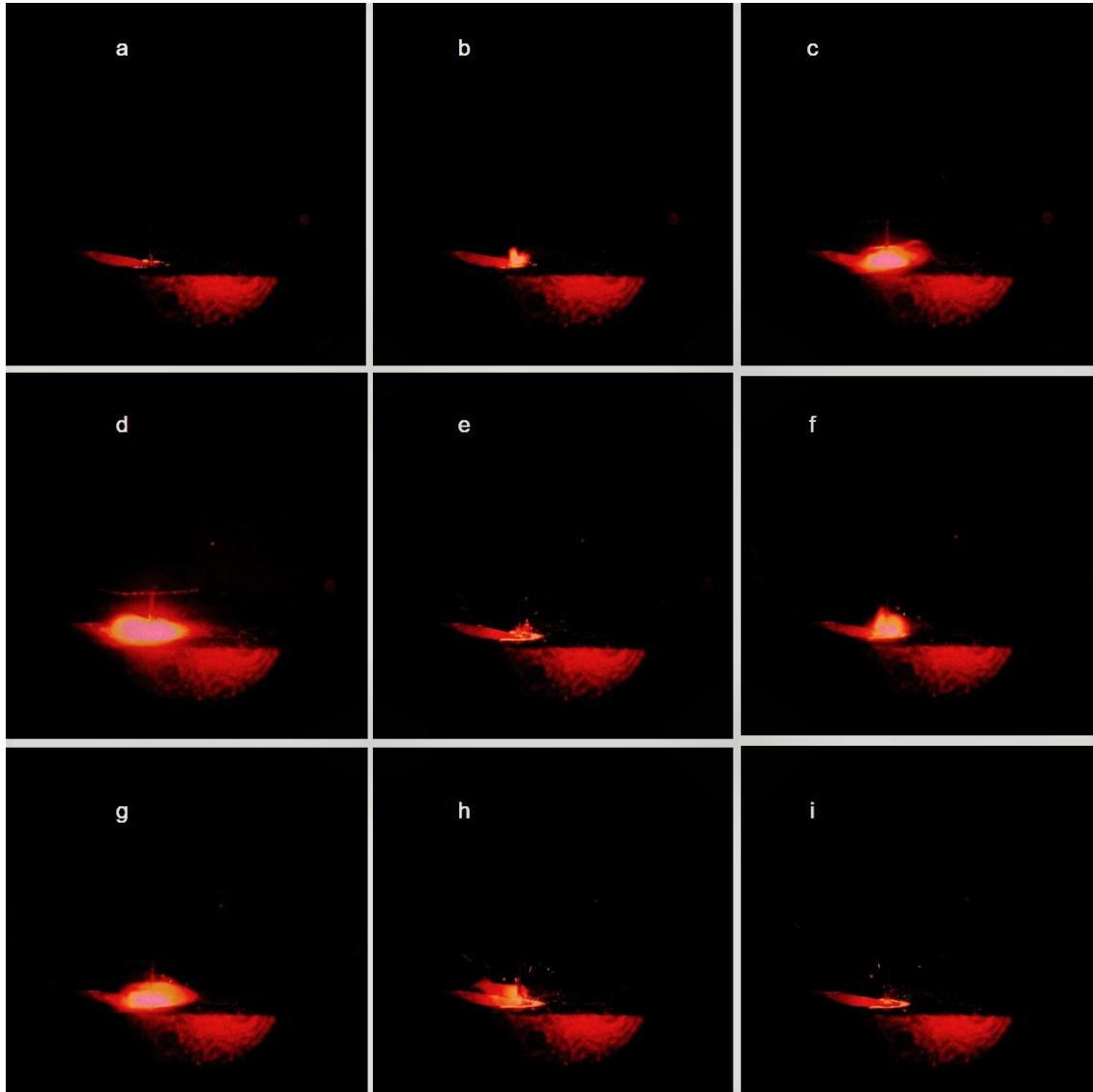


Figure 5.29: High speed camera footage of metal transfer in ceramic region a) Arc off b,c) Arc ignition d) Asymmetric arc e) Servo motor drawn up without droplet detachment f,g) Arc ignition h) Droplet detachment i) Arc off

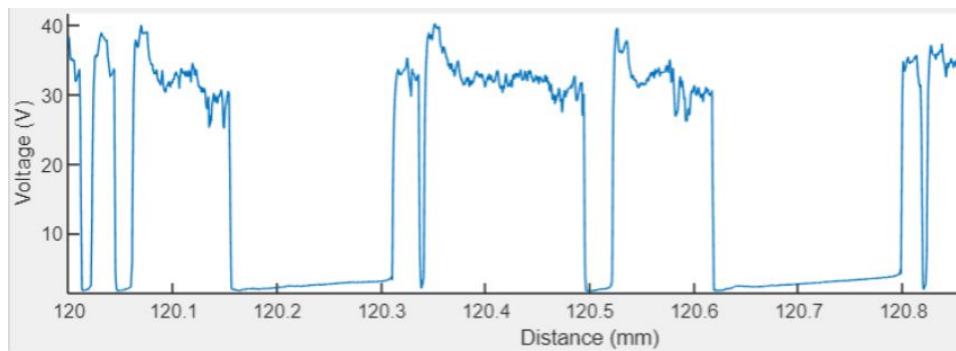


Figure 5.30: Voltage waveform in ceramic region

The voltage waveform from the ceramic region also confirms that the presence of the anomaly affects the frequency and mechanism of droplet detachment, as seen in Fig 5.30. The serrated waveform indicates that the presence of the anomaly does not allow the metal drop to act as a bridge between the wire and the base plate for each time the servo motor draws the wire upwards using digital process control.

It is also observed that the shape of the plasma arc becomes asymmetrical when the torch is printing over the ceramic anomaly, as shown in Fig 5.31 where the torch is moving from left to right. The presence of the ceramic is seen to affect the arc shape and hence will also have an effect on the geometry and depth of penetration in the weld sample.

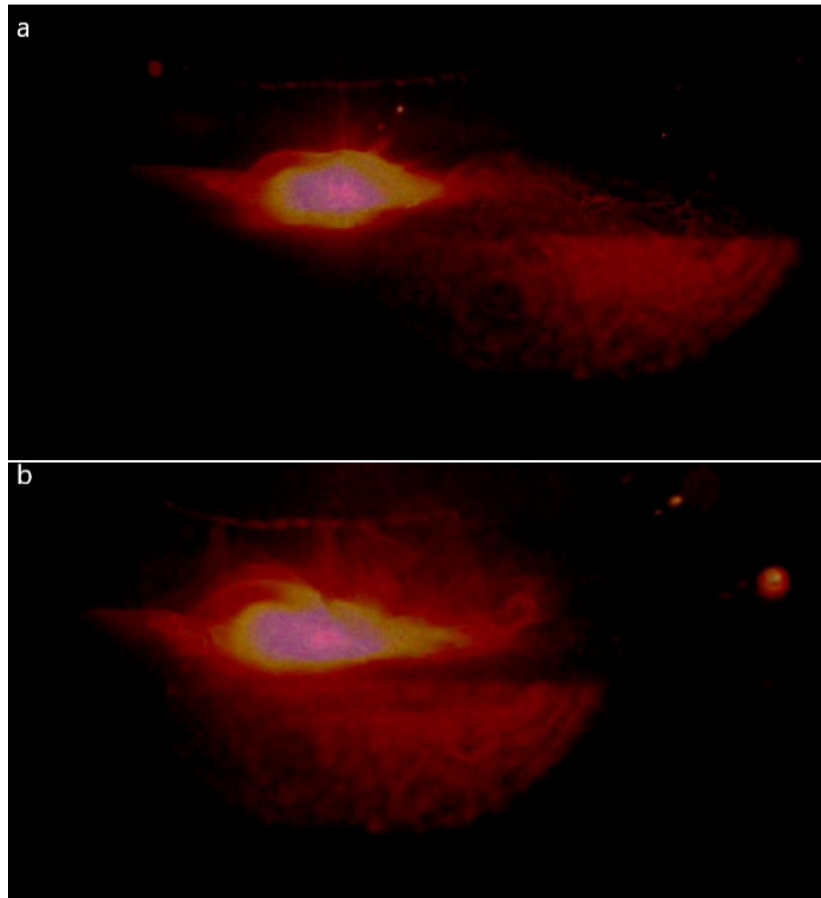


Figure 5.31: a) Symmetric arc in ceramic free region b) Asymmetric arc in ceramic region

### **5.6.2.3 Weld Appearance and Geometry**

The previous sections studied the correlation between the detected OES signal and the presence of a ceramic anomaly on the base plate. In this section, the effect of the anomaly on the geometry of the weld and penetration into the base plate is studied.

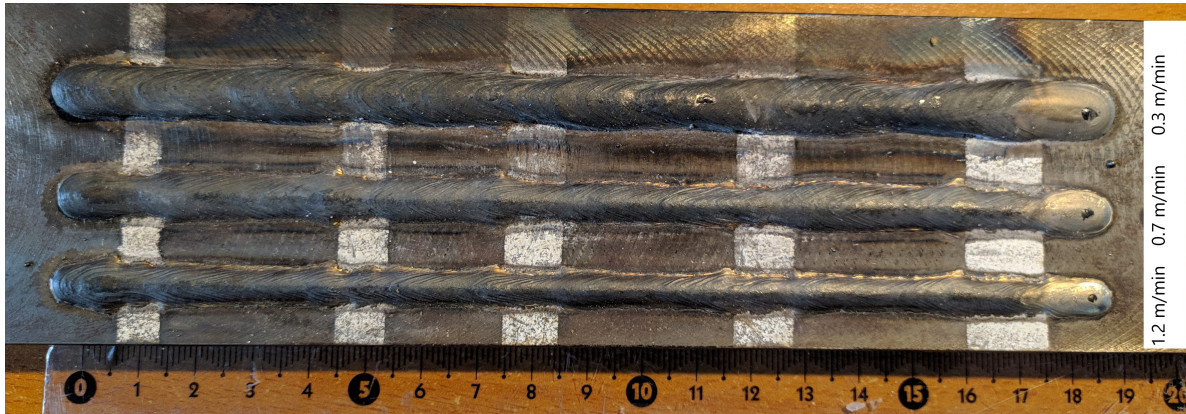


Figure 5.32: 180 mm welds of different travel speeds printed on the ceramic pattern for anomaly detection with welding current of 160 A and welding voltage of 18 V

Fig 5.32 shows the weld beads printed on the ceramic pattern for all travel speeds. It can be seen that the width of the weld bead reduces when it enters the ceramic region and increases again outside, creating a ‘neck’ shape over the anomaly. This observation can be explained by the voltage waveform and high speed camera footage - the increase in short circuit time and the dynamics of drop detachment is altered by the ceramic and results in lesser amount of metal being transferred from the wire to the base plate. The setup of the anomaly detection experiment had the ceramic strip increasing in width in order to study the effect of the size of the simulated anomaly on the collected spectrum as well as the weld geometry.

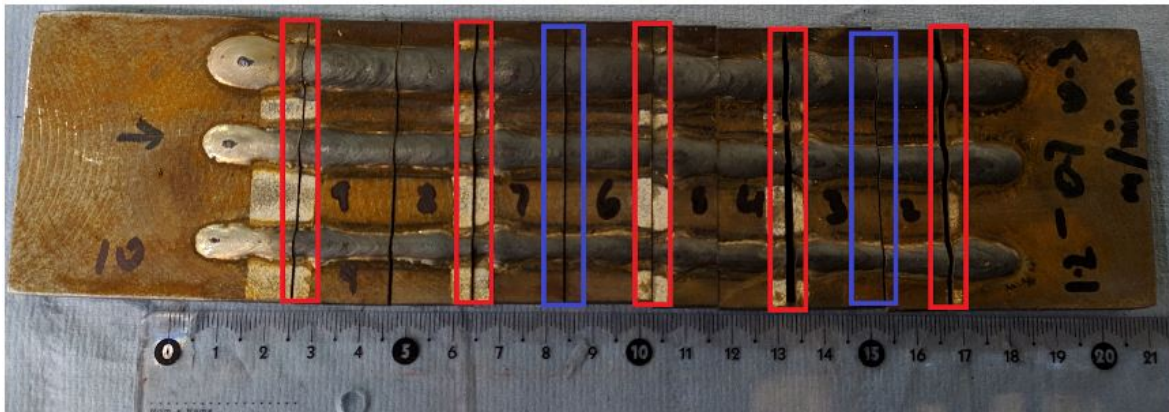


Figure 5.33: Sample cross-sections for optical microscopy analysis

The base plate was cut into section as shown in Fig 5.33. The sections marked in red were across each of the ceramic strips and the sections in blue were across the base metal with no ceramic present, and is referred as Metal Sample 1 and 2. The weld bead geometry was studied using an optical microscope for all travel speeds. The purpose of optical microscopy was to study the difference in the weld geometry between sections with and without the ceramic anomaly. Microscopy measurements were also done to correlate the weld geometry with the width of the simulated ceramic anomaly.

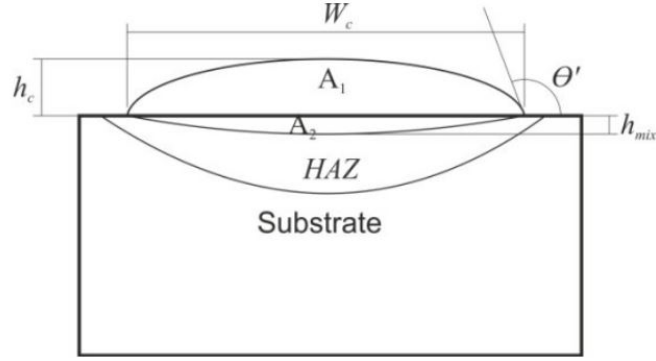


Figure 5.34: Schematic of a WAAM weld track [64]

For the cross-sections shown in Fig 5.34, weld geometry parameters like the height  $h_c$ , melt depth  $h_{mix}$  and width  $W_c$  were measured. For every travel speed, these parameters are tabulated for the five ceramic and two metal cross-sections in Tables 5.1, 5.2 and 5.3.

Table 5.1: Weld geometry parameters for TS = 1.2 m/min

Sample Cross section	$W_c(\mu m)$	$h_c(\mu m)$	$h_{mix}(\mu m)$
Ceramic 5 mm	6585	1283	1000
Ceramic 6 mm	5890	1194	550
Ceramic 8 mm	6321	1235	588
Ceramic 10 mm	5762	1195	599
Ceramic 15 mm	6537	1342	794
Metal Sample 1	7644	1539	1209
Metal Sample 2	7350	1394	1292

Table 5.2: Weld geometry parameters for TS = 0.7 m/min

Sample Cross section	$W_c(\mu m)$	$h_c(\mu m)$	$h_{mix}(\mu m)$
Ceramic 5 mm	7085	1872	774
Ceramic 6 mm	6262	1578	931
Ceramic 8 mm	6683	1617	657
Ceramic 10 mm	7772	1627	794
Ceramic 15 mm	7772	1871	991
Metal Sample 1	8457	1931	1098
Metal Sample 2	8274	1902	1123

Table 5.3: Weld geometry parameters for TS = 0.3 m/min

Sample Cross section	$W_c(\mu m)$	$h_c(\mu m)$	$h_{mix}(\mu m)$
Ceramic 5 mm	9830	5822	1049
Ceramic 6 mm	9234	4893	1607
Ceramic 8 mm	8135	4126	1029
Ceramic 10 mm	8104	3452	1232
Ceramic 15 mm	7830	2989	1774
Metal Sample 1	10273	5978	1255
Metal Sample 2	9673	5795	774

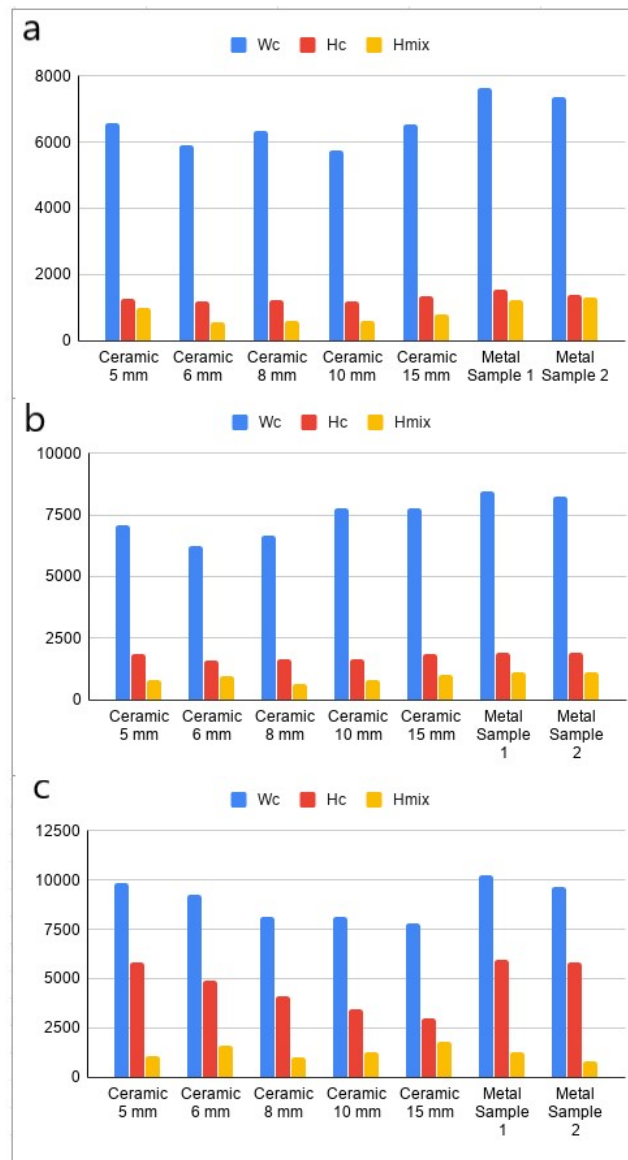


Figure 5.35: Weld geometry parameters for all samples at a) TS = 1.2 m/min b) TS = 0.7m/min c) TS = 0.3 m/min



The cross-sections underwent coarse polishing and was etched with 2% nital etchant. The etched samples were viewed under a Keyence optical microscope at a magnification of 20x in order to obtain the weld profile and calculate the weld geometry parameters.

The weld parameters have no observable correlation with the width of the simulated ceramic impurity for any travel speed under the current tested conditions. The melt depth  $H_{mix}$  shows a slight increase with increasing ceramic width, but this effect can be attributed to the accumulated heating of the base plate during deposition.

Another observation was that all the metal samples' welds showed a higher width, melt depth and height compared to the ceramic cross-sections, except one sample at TS= 0.3 m/min. This observation supports the high frequency voltage data and high-speed camera footage where it was determined that the ceramic hindered the metal transfer between the wire and base plate and hence leads to lesser amount of metal being deposited in a region with the surface having anomaly present. The deviation of the observations made for the metal sample at a TS = 0.3 m/min could be due to unstable printing conditions seen even in the ceramic free region as evidenced in the plasma temperature and intensity ratio observations.

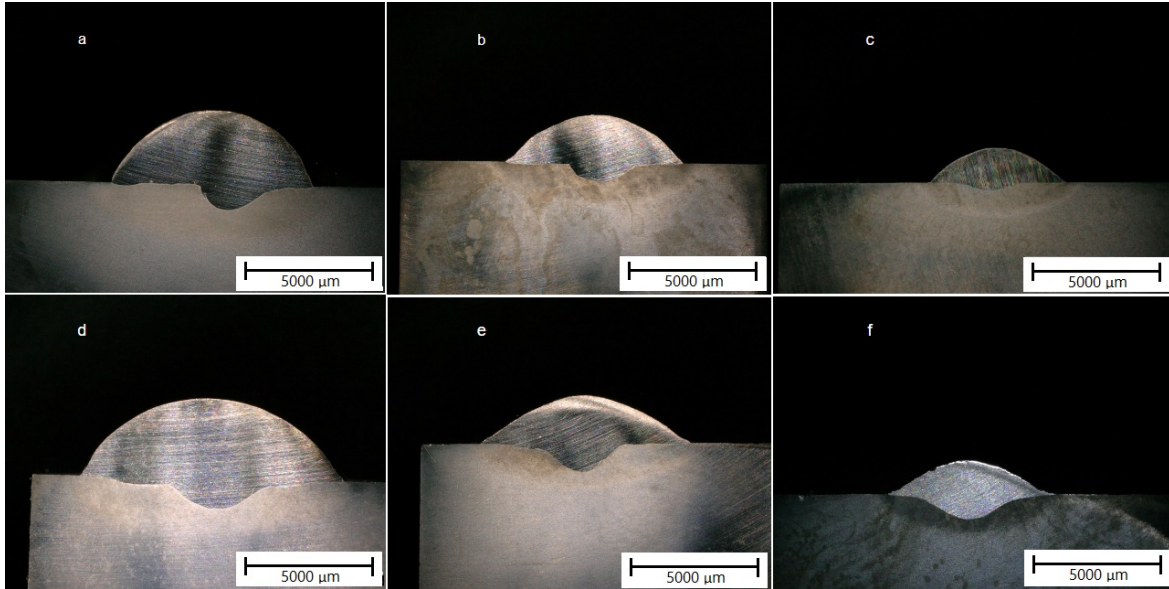


Figure 5.36: Optical micrographs of weld samples at a) TS = 0.3 m/min in ceramic b) TS = 0.7 m/min in ceramic c) TS = 1.2 m/min in ceramic d) TS = 0.3 m/min without ceramic e) TS = 0.7 m/min without ceramic f) TS = 1.2 m/min without ceramic

The shape of the observed weld profiles differ between the cross-sections of the ceramic and metal samples. The weld shape in the ceramic cross-section is asymmetric compared to the metal cross-sections. The asymmetrical plasma arc in the ceramic region observed in Fig 5.31 can be attributed as the reason for this observation.

### 5.6.3 Conclusions of Anomaly Test

Optical emission spectroscopy was applied during WAAM single bead deposition tests through optimizing OES data collection (setup, settings) and validating the data repeatability and reliability. The collected data was processed through the self-programmed app, which was

successfully developed, tested under different conditions and used for data analysis during this study.

Optical emissions from the plasma arc were collected and processed to detect the presence of an intentionally deposited ceramic pattern to simulate the presence of anomalies on the base plate during deposition. Plasma temperature and intensity ratio profiles were used to characterize the presence of anomalous conditions. It was found that the presence of the ceramic can be detected for a travel speed of 1.2 m/min, but is not completely reliable for travel speeds of 0.7 m/min and 1.2 m/min. High frequency voltage data and high-speed camera footage shows that the presence of the ceramic affects the short-circuit metal transfer mechanism from the wire to the base plate. The ceramic acts as a barrier and increases the short circuit time and slows down the metal deposition.

The processed OES signals do not have a correlation with the plasma temperature and intensity ratio profiles for travel speeds of 0.7 m/min and 0.3 m/min. A possible explanation for this observation can be attributed to the spectrometer data collection settings. The integration time of the spectrometer was set at 25 ms - which is the time the sensor is exposed to the arc light to generate one data file. The presence of the ceramic impurity has the same effect on the metal transfer for all travel speeds. However, the increase in short circuit time and inhibited metal transfer is only reflected when the travel speed is the highest at 1.2 m/min because there is a significant reduction in the intensity of the radiation in 25 ms when the torch is printing over the ceramic region. For slower travel speeds of 0.7 m/min and 0.3 m/min, despite a longer short circuit time and inhibited metal transfer, the number of voltage cycles in 25 ms is high enough to not have an effect on the intensity profiles. A possible solution for this could be using a spectrometer with a higher sensitivity such that the integration time can be set at a lower value without significantly affecting the signal to noise ratio of the collected spectrum.





## Chapter 6

# Conclusions and Future Directions

### 6.1 Conclusions

The main goal of this study was to explore an OES based monitoring system for the WAAM process and develop tools which help to achieve this. The following conclusions were made at the end of the study:

- The WAAM process, the physics of the plasma arc, and the laws of physics governing the plasma state were studied to build a reliable OES experiment setup to collect optical emission data.
- A self-programmed software was developed to process the collected data to evaluate the contribution of baseline continuum radiation, identify the emission peak lines of different atomic species, calculate the plasma temperature and intensity ratio profiles for studying the potential relationships among the optical emission signal and processing conditions.
- The optimum observation angle.  $60^\circ$  was chosen to be the observation angle for all experiments.
- The absorption of the plasma radiation by the metal vapours that are present due to high temperatures of the printing environment.
- A peak characterization experiment was done where the functionality of the peak matching algorithm was tested with different combinations of wire feed material and shielding gas. It was shown that the software was able to identify and characterize emission peaks detected for different material combinations.
- The intensity of the detected radiation from the plasma increases as a function of the increased electrical energy input into the system.
- The plasma temperature and intensity ratio profiles can be used to characterize the beginning of stable metallic bonding, but cannot be used to accurately describe the ramping conditions of the experiment.
- During the anomaly detection tests, the fastest travel speed of 1.2 m/min, both the plasma temperature and intensity ratio profile showed a reduction in signal when printing over a ceramic region. However data collected from travel speeds of 0.7 m/min and

0.3 m/min did not always show a characterizable signal to indicate the presence of the anomaly.

- Secondary investigation techniques like high-frequency V-I sensors and high-speed camera footage was used to investigate possible reasons for the OES observations. These investigations showed that the presence of the ceramic anomaly affects the short-circuit metal transfer mechanism from the wire to the base plate. The ceramic acts as a barrier and increases the short circuit time and slows down the metal deposition.

## 6.2 Future Directions

A key result of this study was the absence of a characterizable signal in the anomaly detection test for slower travel speeds of 0.7 m/min and 0.3 m/min. This observation was attributed to the integration time (25 ms) of the spectrometer, which may not capture the changes in the intensity of the plasma radiation as elaborated in Section 5.6.2. Lower values of integration time causes the detected signals to have a higher level of noise and false peaks in the emission spectrum. Using a spectrometer with a higher sensitivity would maintain the high signal-to-noise ratio while reducing the integration time.

With the setup and software in place, many more experiments can be conducted with different processing conditions to test the application of OES for further quality monitoring and control of the WAAM, e.g. - different metal transfer modes or detecting improper shielding conditions. Improved software systems can be designed to enable real time data collection and post-processing, which could be used as a tool to monitor arc stability while printing. The long term goal for the development of this monitoring system is to integrate with a feedback-based control system with the ability to self-correct the printing process. By further studying the correlation between the process parameters, weld geometry and the optical emission signal, processed spectrum data like plasma temperature and intensity ratio can be used to build a feedback system that controls the process parameters to maintain a predetermined weld geometry.

# Bibliography

- [1] Stephen T. Newman, Zicheng Zhu, Vimal Dhokia, and Alborz Shokrani. Process planning for additive and subtractive manufacturing technologies. *CIRP Annals*, 64(1):467–470, 2015. 3
- [2] Vinesh Raja, Shujun Zhang, John Garside, Chris Ryall, and David Wimpenny. Rapid and cost-effective manufacturing of high-integrity aerospace components. *The International Journal of Advanced Manufacturing Technology*, 27(7-8):759–773, January 2006. 3
- [3] M. G. Mehrabi, A. G. Ulsoy, and Y. Koren. Reconfigurable manufacturing systems: key to future manufacturing. *Journal of Intelligent Manufacturing*, 11(4):403–419, 2000. 3
- [4] Joost R. Duflou, John W. Sutherland, David Dornfeld, Christoph Herrmann, Jack Jeswiet, Sami Kara, Michael Hauschild, and Karel Kellens. Towards energy and resource efficient manufacturing: A processes and systems approach. *CIRP Annals*, 61(2):587–609, 2012. 3
- [5] A third industrial revolution. *The Economist*, 2012. 4
- [6] B Wu, C Myant, and SZ Weider. The value of additive manufacturing: future opportunities. 2017. xi, 4
- [7] KM Taminger and RA Hafley. Electron beam freeform fabrication: A rapid metal deposition. pages 1–6, Troy, MI, USA, 2003. Society of Plastic Engineers SPE. 4
- [8] Frank G. Arcella and F. H. Froes. Producing titanium aerospace components from powder using laser forming. *JOM*, 52(5):28–30, May 2000. 4
- [9] S. W. Williams, F. Martina, A. C. Addison, J. Ding, G. Pardal, and P. Colegrove. Wire + arc additive manufacturing. *Materials Science and Technology*, 32(7):641–647, May 2016. 4
- [10] Richard Hague, Saeed Mansour, and Naguib Saleh. Design opportunities with rapid manufacturing. *Assembly Automation*, 23(4):346–356, December 2003. 4, 5
- [11] J. Mehnen, J. Ding, H. Lockett, and P. Kazanas. Design for wire and arc additive layer manufacture. In Alain Bernard, editor, *Global Product Development*, pages 721–727. Springer Berlin Heidelberg, Berlin, Heidelberg, 2011. 4
- [12] Lishi Jiao, Zhong Chua, Seung Moon, Jie Song, Guijun Bi, and Hongyu Zheng. Femto-second laser produced hydrophobic hierarchical structures on additive manufacturing parts. *Nanomaterials*, 8(8):601, August 2018. xi, 5

- [13] D. T. Pham and S. S. Dimov. Applications of rapid prototyping technology. In *Rapid Manufacturing*, pages 87–110. Springer London, London, 2001. 5
- [14] N Hopkinson and P Dicknes. Analysis of rapid manufacturing—using layer manufacturing processes for production. *Proceedings of the Institution of Mechanical Engineers, Part C: Journal of Mechanical Engineering Science*, 217(1):31–39, January 2003. 5
- [15] Gideon N. Levy, Ralf Schindel, and J.P. Kruth. Rapid manufacturing and rapid tooling with layer manufacturing (Lm) technologies, state of the art and future perspectives. *CIRP Annals*, 52(2):589–609, 2003. 5
- [16] J.P. Kruth. Material increment manufacturing by rapid prototyping techniques. *CIRP Annals*, 40(2):603–614, 1991. 6
- [17] Mostafa Yakout, M.A. Elbestawi, and Stephen C. Veldhuis. A review of metal additive manufacturing technologies. *Solid State Phenomena*, 278:1–14, July 2018. xi, 6
- [18] William E. Frazier. Metal additive manufacturing: a review. *Journal of Materials Engineering and Performance*, 23(6):1917–1928, June 2014. 6
- [19] Fude Wang, Stewart Williams, Paul Colegrove, and Alphons A. Antonysamy. Microstructure and mechanical properties of wire and arc additive manufactured ti-6al-4v. *Metallurgical and Materials Transactions A*, 44(2):968–977, February 2013. 6
- [20] I. Gibson, D. W. Rosen, and B. Stucker. *Additive manufacturing technologies: rapid prototyping to direct digital manufacturing*. Springer, London ; New York, 2010. OCLC: ocn444428450. 6
- [21] E Brandl, C Leyens, and Dalle Donne. Deposition of Ti-6Al-4V using Nd:YAG laser & wire: Microstructure and mechanical properties. *NATO AVT-163 Specialists Meeting on Additive Technology for Repair of Military Hardware*, (01):1–13, 2009. 6
- [22] Suman Das, Martin Wohler, Joseph J. Beaman, and David L. Bourell. Producing metal parts with selective laser sintering/hot isostatic pressing. *JOM*, 50(12):17–20, December 1998. 6
- [23] Filippo Montevercchi, Giuseppe Venturini, Antonio Scippa, and Gianni Campatelli. Finite element modelling of wire-arc-additive-manufacturing process. *Procedia CIRP*, 55:109–114, 2016. 6
- [24] Stewart Bland and Nesma T. Aboulkhair. Reducing porosity in additive manufacturing. *Metal Powder Report*, 70(2):79–81, March 2015. 6
- [25] Waheed Ul Haq Syed, Andrew J. Pinkerton, and Lin Li. Combining wire and coaxial powder feeding in laser direct metal deposition for rapid prototyping. *Applied Surface Science*, 252(13):4803–4808, April 2006. 7
- [26] Waheed Ul Haq Syed and Lin Li. Effects of wire feeding direction and location in multiple layer diode laser direct metal deposition. *Applied Surface Science*, 248(1-4):518–524, July 2005. 7

- [27] Rui Vilar. Laser alloying and laser cladding. *Materials Science Forum*, 301:229–252, January 1999. 7
- [28] Andrew J. Pinkerton, Waheed Ul Haq Syed, and Lin Li. Theoretical analysis of the coincident wire-powder laser deposition process. *Journal of Manufacturing Science and Engineering*, 129(6):1019–1027, December 2007. 7
- [29] Young-Nam Ahn and Cheolhee Kim. Comparison of powder feeding and wire feeding in laser cladding. *Journal of Welding and Joining*, 31(4):13–16, August 2013. 7
- [30] Nikola Knezović and Angela Topić. Wire and arc additive manufacturing (Waam) – a new advance in manufacturing. In Isak Karabegović, editor, *New Technologies, Development and Application*, volume 42, pages 65–71. Springer International Publishing, Cham, 2019. xi, 7, 9
- [31] R Baker. Method of making decorative articles. *United States Patent*, 1927. 8
- [32] Carpenter and Kerr. Method and apparatus for metal coating metal pipes by electric fusion. *United States Patent No.2,427,350*, 1947. 8
- [33] A Ujiie. Process and apparatus for triple-electrode MIG welding using short-circuit and spray-arc deposition. *United States patent US3746833A*, pages 2–7, 1972. 8
- [34] Brandi and Luckow. Method of making large structural one-piece parts of metal, particularly one-piece shafts. *United States Patent No.3,985,995*, 1976. 8
- [35] K Kussmaul, FW Schoch, and H Luckow. High quality large components ‘shape welded’ by a SAW process. *Weld J*, 62(9):17–24, 1983. 8
- [36] FW Schoch. *Properties of large shape-welded items, material tests carried out on a 72 t test piece made from 10MnMoNi55 all-weld metal*. PhD thesis, Materialprüfungsanstalt Universität Stuttgart, Stuttgart, 1984. 8
- [37] PM Dickens, Pridham, and RC Cobb. Rapid prototyping using 3-D welding. Austin, TX, 1992. 8
- [38] Yu Ming Zhang, Pengjiu Li, Yiwei Chen, and Alan T. Male. Automated system for welding-based rapid prototyping. *Mechatronics*, 12(1):37–53, February 2002. 8
- [39] L Li and W M Steen. A dual-frequency electromagnetic sensor for non-contact dilution evaluation in laser cladding and alloying processes. *Measurement Science and Technology*, 7(4):650–660, April 1996. xi, 8, 13, 14
- [40] M. Doubenskaia, Ph. Bertrand, and I. Smurov. Optical monitoring of Nd:YAG laser cladding. *Thin Solid Films*, 453-454:477–485, April 2004. 8, 13
- [41] J Hoffman. *Development of an observation and control system for industrial laser cladding*. PhD thesis, University of Twente, Enschede, 2009. 8, 13
- [42] Johnnieew Zhong Li, Mohd Rizal Alkahari, Nor Ana Binti Rosli, Rafidah Hasan, Mohd Nizam Sudin, Faiz Redza Ramli, Faculty of Mechanical Engineering, Universiti

- Teknikal Malaysia Melaka Hang Tuah Jaya, Durian Tunggal, Melaka 76100, Malaysia, and Center of Advanced Research on Energy, Universiti Teknikal Malaysia Melaka, Melaka, Malaysia. Review of wire arc additive manufacturing for 3d metal printing. *International Journal of Automation Technology*, 13(3):346–353, May 2019. xi, xi, 9, 10, 11, 12
- [43] Donghong Ding, Zengxi Pan, Dominic Cuiuri, Huijun Li, Nathan Larkin, and Stephen van Duin. Automatic multi-direction slicing algorithms for wire based additive manufacturing. *Robotics and Computer-Integrated Manufacturing*, 37:139–150, February 2016. 9
- [44] S. Suryakumar, K.P. Karunakaran, Alain Bernard, U. Chandrasekhar, N. Raghavender, and Deepak Sharma. Weld bead modeling and process optimization in Hybrid Layered Manufacturing. *Computer-Aided Design*, 43(4):331–344, April 2011. 9
- [45] Jun Xiong, Yanjiang Li, Rong Li, and Ziqiu Yin. Influences of process parameters on surface roughness of multi-layer single-pass thin-walled parts in GMAW-based additive manufacturing. *Journal of Materials Processing Technology*, 252:128–136, February 2018. 9
- [46] Filomeno Martina, Paul A. Colegrove, Stewart W. Williams, and Jonathan Meyer. Microstructure of interpass rolled wire + arc additive manufacturing ti-6al-4v components. *Metallurgical and Materials Transactions A*, 46(12):6103–6118, December 2015. 10
- [47] Wen Shifeng, Li Shuai, Wei Qingsong, Chunze Yan, Zhang Sheng, and Shi Yusheng. Effect of molten pool boundaries on the mechanical properties of selective laser melting parts. *Journal of Materials Processing Technology*, 214(11):2660–2667, November 2014. 10
- [48] Bi Zhang, Yongtao Li, and Qian Bai. Defect formation mechanisms in selective laser melting: a review. *Chinese Journal of Mechanical Engineering*, 30(3):515–527, May 2017. xi, 10
- [49] Shyam Barua, Todd Sparks, and Frank Liou. Development of low-cost imaging system for laser metal deposition processes. *Rapid Prototyping Journal*, 17(3):203–210, April 2011. 11
- [50] H. Meier and Ch. Haberland. Experimental studies on selective laser melting of metallic parts. *Materialwissenschaft und Werkstofftechnik*, 39(9):665–670, September 2008. 11
- [51] G. K. L. Ng, A. E. W. Jarfors, G. Bi, and H. Y. Zheng. Porosity formation and gas bubble retention in laser metal deposition. *Applied Physics A*, 97(3):641–649, November 2009. 11
- [52] Alison Wilby and DW Neale. Defects Introduced into Metals during Fabrication and Service. 2011. 12
- [53] Manuel Marya, Virendra Singh, Surendar Marya, and Jean Yves Hascoet. Microstructural development and technical challenges in laser additive manufacturing: case study with a 316l industrial part. *Metallurgical and Materials Transactions B*, 46(4):1654–1665, August 2015. 12

- [54] Thorsten Scharowsky, Vera Juechter, Robert F. Singer, and Carolin Körner. Influence of the scanning strategy on the microstructure and mechanical properties in selective electron beam melting of ti-6al-4v: influence of the scanning strategy on the microstructure .... *Advanced Engineering Materials*, 17(11):1573–1578, November 2015. 12
- [55] Ana Brandão, Romain Gerard, Johannes Gumpinger, Stefano Beretta, Advenit Makaya, Laurent Pambaguian, and Tommaso Ghidini. Challenges in additive manufacturing of space parts: powder feedstock cross-contamination and its impact on end products. *Materials*, 10(5):522, May 2017. xi, 12
- [56] NIST. Measurement Science Roadmap for Metal-Based Additive Manufacturing. 2013. 13
- [57] S. Nagarajan, P. Banerjee, W. Chen, and B.A. Chin. Control of the welding process using infrared sensors. *IEEE Transactions on Robotics and Automation*, 8(1):86–93, February 1992. 13
- [58] Harald Krauss, Thomas Zeugner, and Michael F. Zaeh. Thermographic process monitoring in powderbed based additive manufacturing. pages 177–183, Boise, Idaho, 2015. 13
- [59] S. I. Rokhlin and A. C. (Ohio State Univ Guu. A study of arc force, pool depression and weld penetration during gas tungsten arc welding. *Welding Journal (Miami); (United States)*, 72:8, August 1993. 13
- [60] Matthias Faes, Frederik Vogeler, Kurt Coppens, Hans Valkenaers, Wim Abbeloos, Toon Goedeme, and Eleonora Ferraris. Process monitoring of extrusion based 3d printing via laser scanning. 2014. 13
- [61] Armin P. Langheinrich and D. Blair Roberts. Optical emission spectroscopy. In Richard E. Wainerdi and Ernst A. Uken, editors, *Modern Methods of Geochemical Analysis*, pages 169–204. Springer US, Boston, MA, 1971. 14
- [62] George G. Gifford. Applications of optical emission spectroscopy in plasma manufacturing systems. pages 454–465, Santa Clara, CA, March 1991. 14
- [63] F Valensi, S Pellerin, A Boutaghane, K Dzierzega, S Zielinska, N Pellerin, and F Briand. Plasma diagnostics in gas metal arc welding by optical emission spectroscopy. *Journal of Physics D: Applied Physics*, 43(43):434002, November 2010. 14
- [64] Wei Ya, Ali Riza Konuk, Ronald Aarts, B. Pathiraj, and Bert Huis in ‘t Veld. Spectroscopic monitoring of metallic bonding in laser metal deposition. *Journal of Materials Processing Technology*, 220:276–284, June 2015. xiii, 14, 23, 52, 80
- [65] S.A. Linnik and A.V. Gaydaychuk. Application of optical emission spectroscopy for the determination of optimal CVD diamond growth parameters in abnormal glow discharge plasma. *Vacuum*, 103:28–32, May 2014. 14
- [66] Cerrai and Trucco. On matrix effect in laser sampled spectrochemical analysis. *Energia Nucleare 15*, pages 581–587, 1968. 15

- [67] A.R. Konuk, R.G.K.M. Aarts, A.J. Huis in't Veld, T. Sibillano, D. Rizzi, and A. Ancona. Process control of stainless steel laser welding using an optical spectroscopic sensor. *Physics Procedia*, 12:744–751, 2011. 15, 21
- [68] Lijun Song, Cunshan Wang, and Jyoti Mazumder. Identification of phase transformation using optical emission spectroscopy for direct metal deposition process. page 82390G, San Francisco, California, USA, February 2012. 15, 21, 23
- [69] B. Ribic, P. Burgardt, and T. DebRoy. Optical emission spectroscopy of metal vapor dominated laser-arc hybrid welding plasma. *Journal of Applied Physics*, 109(8):083301, April 2011. 15
- [70] Marek S. Weglowski. Investigation on the electric arc light emission in TIG welding. *International Journal of Computational Materials Science and Surface Engineering*, 1(6):734, 2007. 15
- [71] A Drieling. In Situ Defect Detection Using Three Color Spectroscopy in Laser Powder Bed Additive Manufacturing. 2018. 15
- [72] Konrad Bartkowiak. Direct laser deposition process within spectrographic analysis in situ. *Physics Procedia*, 5:623–629, 2010. 15
- [73] S. W. Williams, F. Martina, A. C. Addison, J. Ding, G. Pardal, and P. Colegrove. Wire + arc additive manufacturing. *Materials Science and Technology*, 32(7):641–647, May 2016. 17
- [74] Wei Ya and Kelvin Hamilton. On-demand spare parts for the marine industry with directed energy deposition: Propeller use case. pages 70–81, September 2017. 17
- [75] L. Ebdon and E. Hywel Evans, editors. *An introduction to analytical atomic spectrometry*. John Wiley, Chichester ; New York, 1998. 17, 20, 22
- [76] Teena Choudhary and Dr Kailash Chaudhary. A study on metal transfer mechanism in gas metal arc welding. *International Journal of Scientific Research in Science, Engineering and Technology*, 3(8):82–93, December 2017. xi, 17, 18
- [77] Desineni Subbaram Naidu, Selahattin Ozelik, and Kevin L. Moore. Gas metal arc welding: modeling. In *Modeling, Sensing and Control of Gas Metal Arc Welding*, pages 9–93. Elsevier, 2003. 18
- [78] S. Selvi, A. Vishvakshnan, and E. Rajasekar. Cold metal transfer (Cmt) technology - An overview. *Defence Technology*, 14(1):28–44, February 2018. xi, 19
- [79] G. Cristoforetti, A. De Giacomo, M. Dell’Aglio, S. Legnaioli, E. Tognoni, V. Palleschi, and N. Omenetto. Local thermodynamic equilibrium in laser-induced breakdown spectroscopy: beyond the mcwhirter criterion. *Spectrochimica Acta Part B: Atomic Spectroscopy*, 65(1):86–95, January 2010. 20
- [80] Jörg Hermann, David Grojo, Emanuel Axente, and Valentin Craciun. Local thermodynamic equilibrium in a laser-induced plasma evidenced by blackbody radiation. *Spectrochimica Acta Part B: Atomic Spectroscopy*, 144:82–86, June 2018. 20



- [81] Hans R. Griem. *Principles of plasma spectroscopy*. Cambridge University Press, 1 edition, October 1997. 20, 21
- [82] Hiroshi Akatsuka. Optical Emission Spectroscopic (Oes) analysis for diagnostics of electron density and temperature in non-equilibrium argon plasma based on collisional-radiative model. *Advances in Physics: X*, 4(1):1592707, January 2019. 21
- [83] Takashi Fujimoto and R. W. P. McWhirter. Validity criteria for local thermodynamic equilibrium in plasma spectroscopy. *Physical Review A*, 42(11):6588–6601, December 1990. 21
- [84] A. J. M. Mackus, S. B. S. Heil, E. Langereis, H. C. M. Knoop, M. C. M. van de Sanden, and W. M. M. Kessels. Optical emission spectroscopy as a tool for studying, optimizing, and monitoring plasma-assisted atomic layer deposition processes. *Journal of Vacuum Science & Technology A: Vacuum, Surfaces, and Films*, 28(1):77–87, January 2010. 22
- [85] Hans-Joachim Kunze. Quantities of spectroscopy. In *Introduction to Plasma Spectroscopy*, volume 56, pages 5–14. Springer Berlin Heidelberg, Berlin, Heidelberg, 2009. 23
- [86] A. Kramida, Yu. Ralchenko, J. Reader, and and NIST ASD Team. NIST Atomic Spectra Database (ver. 5.7.1), [Online]. Available: <https://physics.nist.gov/asd> [2017, April 9]. National Institute of Standards and Technology, Gaithersburg, MD., 2019. xi, 32, 59
- [87] H Schulze, Rod Foist, Kadek Okuda, Andre Ivanov, and Robin Turner. A small-window moving average-based fully automated baseline estimation method for raman spectra. *Applied spectroscopy*, 66:757–64, 06 2012. 32
- [88] Ronald Schafer. What is a savitzky-golay filter? [lecture notes]. *IEEE Signal Processing Magazine*, 28(4):111–117, July 2011. 33
- [89] Interaction between impurities and welding variables in determining gta weld shape depending on the trace elements in the base materials, identical changes in welding variables can have an opposite effect on weld shape. 46
- [90] T. Mukherjee and T. DebRoy. Mitigation of lack of fusion defects in powder bed fusion additive manufacturing. *Journal of Manufacturing Processes*, 36:442 – 449, 2018. 46
- [91] Alain Gleizes and Yann Cressault. Effect of metal vapours on the radiation properties of thermal plasmas. *Plasma Chemistry and Plasma Processing*, 37(3):581–600, November 2016. 52